

Table of Contents

List of Figures	3
List of Tables	5
List of Abbreviations	7
I Introduction	8
1 Background	8
2 Project Overview	8
II Methods and Results	11
3 Field Site	11
4 General Sea-Ice Observations	13
5 Sea-Ice Thickness, Snow Depth, Freeboard and Sub-Ice Platelet Layer	17
6 Electromagnetic Sea-Ice Surveys	23
6.1 Single-frequency Electromagnetic Device EM-31	23
6.2 Multi-frequency Electromagnetic Device GEM-2	29
7 Atmospheric observations	42
7.1 First Automatic Weather Station, July - August 2012	42
7.2 Second Automatic Weather Station, October 2012 - January 2013	45
7.3 Comparison of AWS and BSRN data	48
7.4 Eddy Covariance and Turbulent Momentum Flux	50
7.5 General Meteorological Observations during the SIMBIS campaign	52
8 Spectral Radiation	55
8.1 Sensor calibration	55
8.2 Data processing	57
8.3 First Radiation station 10 - 17 August 2012	57
8.4 Second Radiation station October 2012 - January 2013	60
8.5 Surface Albedo Spot Measurements	62
8.6 Surface Albedo Transects	62
8.7 Light Transmission through Sea Ice and Snow	67
9 Sea-Ice Mass-Balance Buoys	73
9.1 IMB AWI01	73
9.2 IMB AWI31	73
9.3 IMB AWI32	76
10 The Unintended Drifting Station	79
11 Snow Observations	81
11.1 General Observations	81
11.2 Snow Pits	81
11.3 Snow Transects	85
11.4 Other Snow-Depths data	85
12 Observations with Under-Ice Cameras	87

12.1	Platelet Camera	87
12.2	PASATA Videos	89
13	Oceanographic Conditions at Atka Bay	92
13.1	CTD at PALAOA Observatory	92
13.2	CTD measurements during SIMBIS campaign	93
13.3	24 h CTD profiles at ATKA21 on 03/04 January 2013	97
14	Sea-Ice Cores	100
14.1	Temperature	100
14.2	Salinity and Density	100
14.3	Chlorophyll a and Phaeophytin	102
14.4	Texture	109
15	Aerial Imagery	113
16	TerraSAR-X	115
III Reference List		117
IV Acknowledgements		119

List of Figures

Figure 1:	Map of Antarctica and AFIN stations	9
Figure 2:	Characteristics of Ekström Ice Shelf	11
Figure 3:	Aerial image of Neumayer III station near Atka Bay. Photo: Mario Hoppmann	12
Figure 4:	MODIS satellite images of Atka Bay from March 2012	13
Figure 5:	Satellite images of Atka Bay (May 2012)	14
Figure 6:	MODIS satellite images from September to November 2012	15
Figure 7:	MODIS derived surface temperature images (IST) of the Atka Bay	15
Figure 8:	Sea-ice conditions at Atka Bay in November 2012	16
Figure 9:	14 June 2012, the day of first drillings	17
Figure 10:	Measuring platelet layer thickness	19
Figure 11:	Results of AFIN drillings in 2012/13	21
Figure 12:	Photo of platelets and brown water	22
Figure 13:	Set-up of EM31 in the kayak	24
Figure 14:	Calibrations of EM31 in horizontal and vertical mode	24
Figure 15:	EM31 tracks color-coded with calculated total thickness	26
Figure 16:	Profiles of EM31 surveys	27
Figure 17:	Probability density functions of EM31 data	28
Figure 18:	Overview of GEM-2 transects in the Atka Bay	32
Figure 19:	Raw data of GEM-2 during drift test	34
Figure 20:	Drift of GEM-2 during drift test	35
Figure 21:	Noise distribution of GEM-2 during drift test	36
Figure 22:	Influence of kayak and field PCs on GEM-2 signal	37
Figure 23:	Photos of GEM-2 calibration	37
Figure 24:	GEM-2 calibration at ATKA11	38
Figure 25:	Grids and Transects	38
Figure 26:	Comparison of the two West to East transects	39
Figure 27:	Grid between ATKA07 and ATKA11	40
Figure 28:	Stationary 24 hour measurement at ATKA21 on 03 January 2013.	41
Figure 29:	Sites of autonomous measurements	42
Figure 30:	AWS on 17 August 2012	43
Figure 31:	Scheme of autonomous measurement station	44
Figure 32:	Instrument setup at ATKA03. Photo: Mario Hoppmann	45
Figure 33:	Aerial photo of instrument setup at ATKA03. Photo: AWI	46
Figure 34:	Atmospheric parameters	46
Figure 35:	Radiation	47
Figure 36:	Albedo, Heat Fluxes and Net Radiation	47
Figure 37:	Snow depth (ultrasonic)	48
Figure 38:	Comparison of AWS and BSRN atmospheric data (daily means)	48
Figure 39:	Comparison of AWS and BSRN radiation data (daily means)	49
Figure 40:	EC station set-up. Photos: Mario Hoppmann	50

Figure 41: Results of EC station	51
Figure 42: Timeseries of 2 m Air Temperature	52
Figure 43: Timeseries of 10 m Windspeed	52
Figure 44: Timeseries of Surface Pressure	53
Figure 45: Timeseries of Horizontal Visibility	53
Figure 46: Timeseries of Cloud Bottom Height	54
Figure 47: RAMSES-ACC-VIS - Hyperspectral UV-VIS Irradiance Sensor. Photo: TriOS	55
Figure 48: Photo of spectral radiometers during calibration	56
Figure 49: Deployment of first radiation station. Photos: Thomas Schmidt, Meike Kühnel	58
Figure 50: First radiation station scheme	59
Figure 51: First radiation station on 17 August 2012	59
Figure 52: Second Radiation station	60
Figure 53: Radiation station scheme	61
Figure 54: Recovery of RAMSES sensor frozen in the sea ice. Photo: Mario Hoppmann	61
Figure 55: Results of continuous irradiance measurements	63
Figure 56: Photo of albedo skidoo	64
Figure 57: GPS tracks of albedo measurements	65
Figure 58: Probability Density of Albedo during transects	66
Figure 59: Instrument setup of under-ice irradiance measurements	68
Figure 60: L-Arm measurements at ATKA11	69
Figure 61: L-Arm measurements at ATKA21	70
Figure 62: Spectral light transmittance directly below sea ice	71
Figure 63: Results of under-ice light measurements on 03 January 2013	72
Figure 64: Scheme of thermistor string AWI01 set up on 10 August 2012	74
Figure 65: Photos of sea-ice mass balance buoy AWI31 (Mario Hoppmann).	75
Figure 66: Temperature and heating data of IMB AWI31	76
Figure 67: Photos of sea-ice mass balance buoy AWI32 (Mario Hoppmann)	76
Figure 68: Temperature and heating data of IMB AWI32	78
Figure 69: Map of Atka Bay and AWI01 GPS positions around 20 August 2012	79
Figure 70: Sea-ice edge near AWS site	80
Figure 71: GPS positions of AWI31 since day of outbreak	80
Figure 72: Snow Pit. Photos: Mario Hoppmann, Stephan Paul	82
Figure 73: Snow properties in November 2012	83
Figure 74: Snow properties in January 2013	84
Figure 75: Snow Fork. Photos: Mario Hoppmann	84
Figure 76: Histograms of snow depths at different sampling sites / dates	86
Figure 77: Under-ice platelet camera. Photo: visatec	88
Figure 78: Under-ice platelet camera in the field. Photos: Mario Hoppmann	89
Figure 79: Platelet camera images. Photos: AWI	90
Figure 80: Massive platelet rise-up event	91
Figure 81: Ice Pump	92
Figure 82: The PALAOA observatory	93
Figure 83: Potential supercooling under Ekström Ice Shelf	94

Figure 84:	CTD in action. Photo: Mario Hoppmann	95
Figure 85:	CTD profiles 21 Nov - 03 Dec 2012	96
Figure 86:	CTD profiles on 13/14 December 2012	97
Figure 87:	CTD profiles on 19 December 2012	97
Figure 88:	CTD profiles 27 - 29 December 2012	98
Figure 89:	CTD profiles on 07 January 2013	98
Figure 90:	Color plots of interpolated CTD measurements at ATKA21 on 03 January 2013	99
Figure 91:	Preparation of sea-ice core for segmentation. Photo: Mario Hoppmann	101
Figure 92:	Photos of sea-ice core at ATKA11. Photos: Mario Hoppmann	101
Figure 93:	<i>WTW Cond3110</i> Conductivity-Meter. Photo: Mario Hoppmann . .	102
Figure 94:	Physical and biological properties of sea-ice cores obtained at different stations in November/December 2012	103
Figure 95:	Scheme of Chlorophyll a determination	104
Figure 96:	TD-700 Laboratory Fluorometer by Turner Designs. Photo: Mario Hoppmann	105
Figure 97:	Linear regression of TD700 fluorometer calibration factor	106
Figure 98:	Photos of Chl a sample processing. Photos: Mario Hoppmann	108
Figure 99:	Photos of thin section processing. Photos: Mario Hoppmann	110
Figure 100:	Texture of sea ice at ATKA11. Photos: Mario Hoppmann	111
Figure 101:	Texture of sea ice at ATKA24. Photos: Mario Hoppmann	112
Figure 102:	Canon 5D Mark II camera mounted on the Helicopter. Photos: Mario Hoppmann	113
Figure 103:	GPS track of aerial images on 22 December 2012	114
Figure 104:	3D mesh model of sea-ice surface	114
Figure 105:	TerraSAR-X satellite (source: EADS Astrium)	115

List of Tables

Table 1:	Calibration dates and coefficients of single exponential fit.	25
Table 2:	Overview of EM31 data in 2012.	25
Table 3:	Summary of GEM-2 data	30
Table 4:	Mean absolute offset values of GEM-2 during drift test	33
Table 5:	Influence of kayak and field computers (SoMo and Archer)	33
Table 6:	Overview of autonomous instruments deployed in 2012	43
Table 7:	RAMSES ACC VIS specifications (www.trios.de)	56
Table 8:	List of TriOS spectral radiometer used at Atka Bay	57
Table 9:	Overview of sea-ice parameters during L-Arm measurements	67
Table 10:	Thermistor numbers at interfaces between media	74
Table 11:	Bore-hole measurements at site IMB32	77
Table 12:	Technical specifications of camera system (source: visatec)	87
Table 13:	Dates and stations of recordings	88
Table 14:	CTD75M specifications	95
Table 15:	Overview of sea-ice cores processed during campaign	100
Table 16:	Calibration of TD700 fluorometer	106

Table 17: TerraSAR-X main imaging modes	116
Table 18: TerraSAR-X data availability	116

List of Abbreviations

AFIN	Antarctic Fast Ice Network
AVHRR	Advanced Very High Resolution Radiometer
AWS	Automatic Weather Station
Chl-a	Chlorophyll-a
CTD	Conductivity Temperature Depth
DFG	German Research Council
DLR	German Center for Aviation and Space Travel
EIS	Ekström Ice Shelf
EM	Electro-magnetic
GPS	Global Positioning System
HCP	Horizontal CoPlanar
IMB	Ice Mass Balance Buoy
IP	Inclination Pressure
MODIS	Moderate Resolution Imaging Spectrometer
NOAA	National Oceanic and Atmospheric Administration
PALAOA	Perennial Acoustic Observatory in the Antarctic Ocean
PASATA	Passive Acoustic Tracking of Antarctic Marine Mammals
RS	Radiation station
SAMS	Scottish Association for Marine Science
SAR	Synthetic Aperture Radar
SIMBIS	Sea-Ice Mass Balance Influenced by Ice Shelves
SP	Snow Pit
UV	Ultraviolet
VCP	Vertical CoPlanar

Introduction

1. Background

Sea ice fastened to coasts, icebergs and ice shelves is of crucial importance for climate and ecosystems. At the same time, it is not represented in climate models and many processes affecting its energy- and mass balance are currently only poorly understood. Near Antarctic ice shelves, which fringe about 44 % of the coastline, this landfast sea ice exhibits two unique characteristics that distinguish it from most other sea ice:

1. Ice platelets form and grow in supercooled water masses, which originate from cavities below the ice shelves. These crystals rise to the surface, where they accumulate beneath the solid sea-ice cover. Through freezing of interstitial water they are incorporated into the sea-ice fabric as platelet ice.
2. A thick and highly stratified snow cover accumulates on the fast ice, altering the response of the surface to remote sensing and affecting sea-ice energy- and mass balance in various ways.

2. Project Overview

In recent years, field studies of Antarctic sea ice were conducted at several locations around the coastline, but mainly in the eastern part of the continent. These studies took place on landfast sea ice in Prydz Bay, Lützow Holm Bay and McMurdo Sound (Heil et al., 1996; Kawamura et al., 1997; Trodahl et al., 2000; Tang et al., 2007; McGuinness et al., 2009; Lei et al., 2010; Leonard et al., 2011, and many more).

Following the need for a coordinated approach on the monitoring of Antarctic landfast sea ice, in particular including other regions of the continent, the Antarctic Fast Ice Network (AFIN) was initiated as a legacy project of the 2007/09 International Polar Year (Heil et al., 2011). By now a number of international partners have joined this network, of which many have already set up fast-ice measuring sites near their Antarctic bases (Figure 1 top), and further countries indicated strong interest to become involved.

To fill the knowledge gap of fast-ice properties and processes in the Weddell Sea region, Germany joined the Antarctic Fast Ice Network with monitoring activities on Atka Bay landfast sea-ice since 2010 (Figure 1 bottom).

Our monitoring activities in the framework of AFIN mainly comprise regular drillings (section 5) and EM-based sea-ice thickness transects (section 6.1) every few weeks as well as the deployment of several autonomous measuring stations (sections 7 and 8). These measurements contribute to the Antarctic Fast Ice Network (AFIN), and in this document

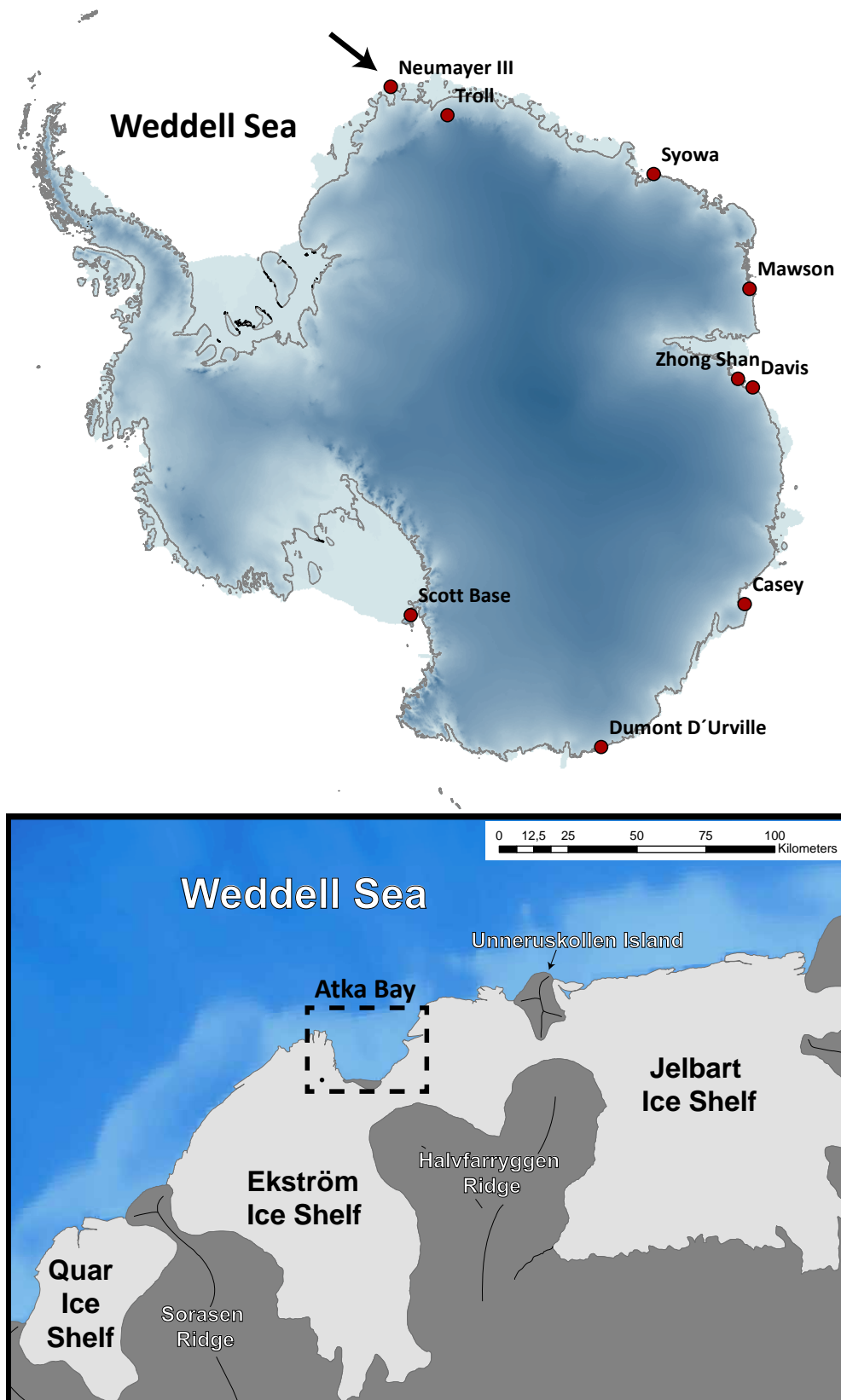


Figure 1: **Top:** Map of Antarctica and stations participating in AFIN; **Bottom:** The study area of Atka Bay is an embayment in the Ekström Ice Shelf, Eastern Weddell Sea. Coastlines: BEDMAP2 (Fretwell et al., 2012)

they are referred to as “AFIN measurements”. The data will be available to members within the AFIN network after quality control and to the wider scientific community under the Antarctic Sea Ice Processes and Climate (ASPeCt) data library.

These regular AFIN measurements were complemented in 2012/13 by a two month field campaign (19 November 2012 to 9 January 2013) of four scientists and technicians in the framework of the project “Sea-Ice Mass Balance influenced by Ice Shelves” (SIMBIS).¹

During the SIMBIS field campaign, we intensified our monitoring by using a variety of methods to investigate the physical properties of the sea ice, its snow cover and the processes affecting their mass- and energy balances at Atka Bay. We focused on the two important characteristics of Antarctic sea ice already mentioned in the introduction:

1. Kipfstuhl (1991) and Günther and Dieckmann (1999) showed in their studies during the 90s, that sea ice at Atka Bay and the associated ecosystem is heavily influenced by ice platelets, which accumulate below the solid sea-ice cover. One of the main objectives of our studies is therefore to give an estimate of the amount and extent of accumulated ice platelets at Atka Bay, and Antarctica in general.
2. The other main focus of this study is the detailed investigation of snow properties and their influence on the landfast sea ice of Atka Bay. The main factors by which a thick snow influences sea-ice mass balance directly is the formation of snow ice through surface flooding and the formation of superimposed ice through snow melting. Passive effects include the efficient insulation of the sea ice with respect to the cool atmosphere, and the reflection of a large fraction of the incoming short-wave irradiance (high albedo). Finally, we try to contribute to the question how snow alters the backscatter signal of X-band radar from satellites.

The main purpose of this report is to summarize our measurements of sea-ice and snow parameters at Atka Bay in 2012. Our activities during the two previous years are covered in Hoppmann et al. (2011) and Hoppmann et al. (2012). Following a general description of the field site, we outline our methods and present the preliminary results.

¹The SIMBIS project is funded through the German Research Council (DFG) in its priority program “Antarctic Research with comparative investigations in Arctic ice areas” (SPP1158, NI 1092/2/HE 2740/12).

II

Methods and Results

3. Field Site

The Atka Bay is a 440 square kilometer-wide indentation of the Ekström Ice Shelf (EIS, Figure 1). The EIS is a small, about 8,700 square kilometer large ice shelf and a part of the Eastern Weddell Ice Shelves (EWIS), a group of several small ice shelves in the Weddell Sea region of Antarctica. The EIS is between 140 and 250 meters thick at the edge, where it rises between 10 and 40 meters above the sea level (Figure 2). Due to a lack of data, the sub-ice shelf cavity in Figure 2d) is interpolated between the point where cavity thickness declined to 100m and the grounding line where cavity thickness is 0 m (Fretwell et al., 2012).

The German Antarctic station Neumayer III (Figure 3) is situated in the northeast of the EIS, about 8 km southwest of Atka Bay. This station serves as the logistical base for all measurements conducted in this region.

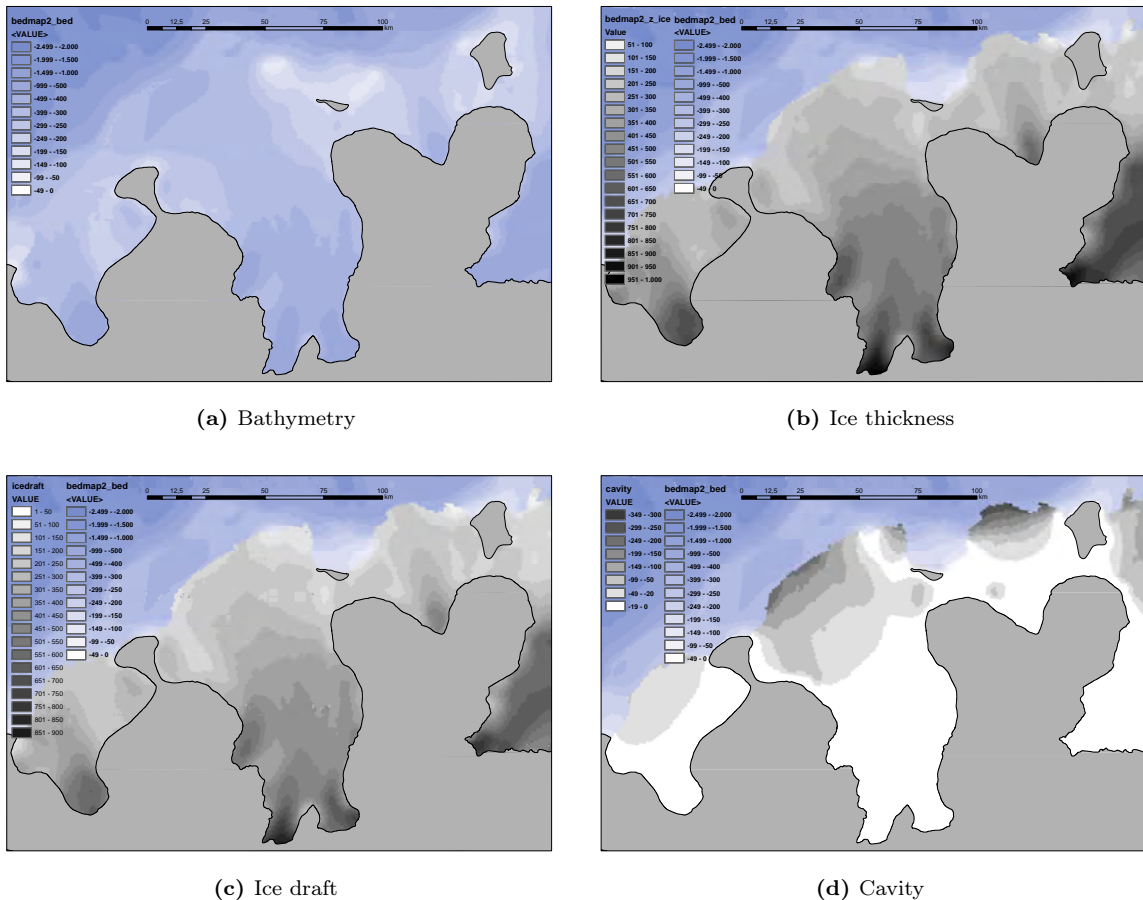


Figure 2: Characteristics of Ekström Ice Shelf, data from BEDMAP2 (Fretwell et al., 2012)

The seasonal sea-ice cover of Atka Bay usually forms between March and April, and grows to its maximum thickness in December. The extent is variable and depends on local conditions, like for example, grounded or passing icebergs and polynyas. Sea ice does not melt in situ during summer, but breaks out once it is destabilized enough by higher water and air temperatures, tidal motion and wind forcing. These factors lead to an outbreak of floes starting in the eastern part of the Bay, usually between December and January. In the southwestern part, sea ice may stay as long as early March, but in most years the Bay is completely ice free at the end of March. Our measurements during the winter season start as soon as the sea ice is accessible by a ramp, which is naturally formed by snow accumulating at the northwestern ice-shelf edge.



Figure 3: Aerial image of Neumayer III station near Atka Bay. Photo: Mario Hoppmann

Initial sea-ice formation in the Bay heavily depends on wind conditions. Sea ice predominantly grows thermodynamically in quiet conditions, but periods of strong westerly winds may push the thin ice towards the western ice shelf, leading to areas of moderately to heavily deformed sea ice in the western part.

Atka Bay is the breeding ground for a large colony of emperor penguins and smaller groups of Adélie penguins (citation). In addition, the numerous Weddell seals migrating to the Atka Bay region depend on the properties of the sea-ice cover (citation).

Finally, sea-ice conditions in this region are important factors regarding the logistical support of the German Neumayer III as well as the South African SANAE IV station by the German research vessel *Polarstern* and the South African research vessel *SA Agulhas*.

4. General Sea-Ice Observations

Sea-ice conditions in Atka Bay in 2012 were very variable, comprising a mix of second-year ice, first-year ice and new ice formed in September 2012. In addition to our field measurements, we used imagery from the Moderate-Resolution Imaging Spectroradiometer (MODIS) onboard the polar orbiting Terra and Aqua satellites (National Aeronautics and Space Administrations (NASA) to assess dates of formation and outbreaks of the fast-ice cover.

Figure 4 shows four MODIS images from March, where almost the entire Bay was ice-free. Some single floes stayed in or were drifted into Atka Bay. They refroze to the western ice-shelf edge, resulting in an area of predominantly second-year sea ice. This area is also visible in X-Band radar imagery, where a brighter color points to higher backscatter values (Figure 8).

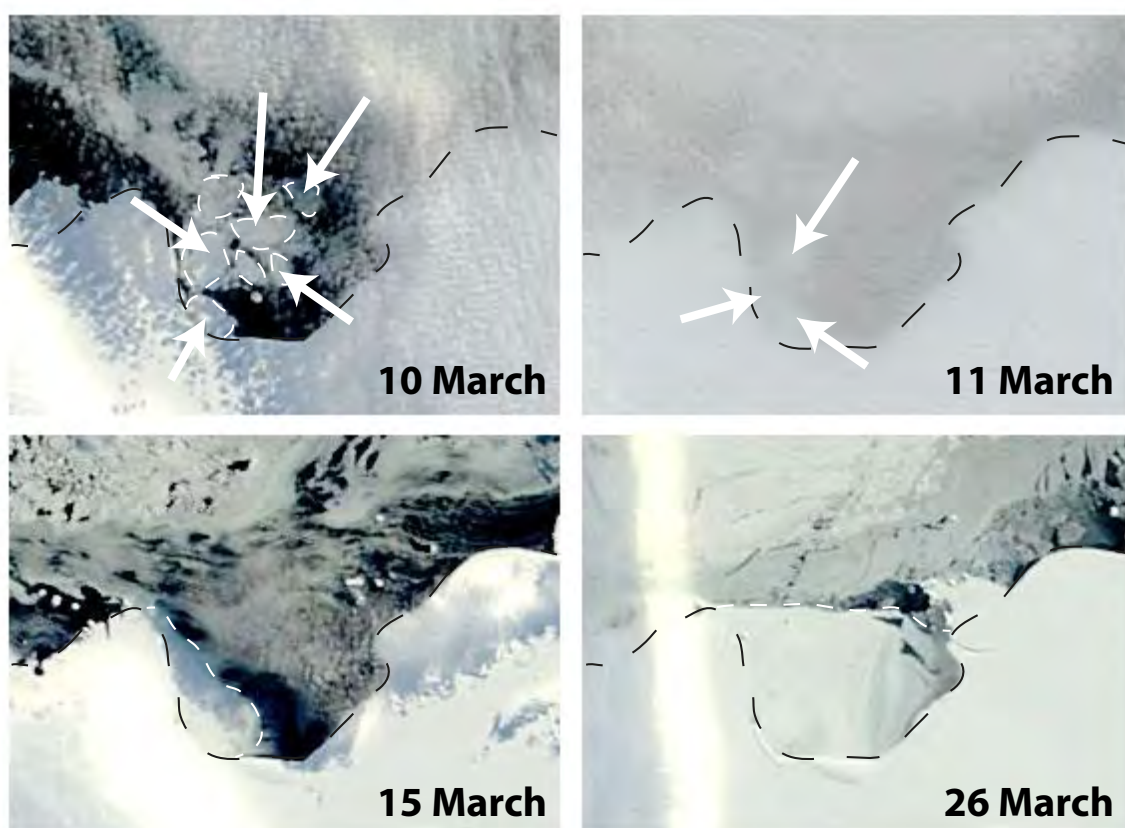


Figure 4: MODIS satellite images of Atka Bay from March 2012. The dashed black line represents the ice shelf edge. On 10 and 11 March, some smaller floes are visible through the cloud cover, which stayed in or drifted into the Bay. On 15 March, they are already refrozen to the western ice-shelf edge. On 26 March, the entire Bay was covered by sea-ice for the first time, but several storms in April caused partly break ups (not shown).

Beginning in April 2012, sea-ice conditions at Atka Bay were regularly inspected from the ice shelf edge. In addition, the usual site of the snow ramp, which connects the shelf with the sea-ice several meters below, was inspected every few weeks. At the end of April, this ramp was still not passable due to a lack of drifting snow filling up the gaps, the main gap being

around 3 height meters at that time. Visual observations confirmed a closed fast-ice sheet at the end of April, where a few weeks before open water was still present. The uneven surface over wide areas of the visible fast ice confirmed that the it mainly consisted of pressure-ridged pack-ice floes, with minimal snow cover.

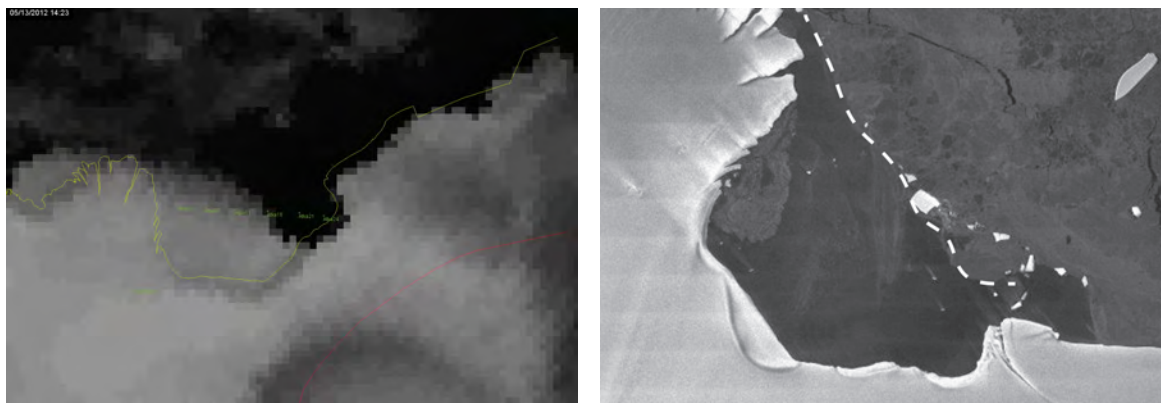


Figure 5: Satellite images of Atka Bay (May 2012). **Left:** NOAA Avhrr satellite image on 13 May 2012. **Right:** TerraSAR-X Quicklook from 31 May 2012 (©DLR). The dashed line depicts the fast ice edge.

NOAA satellite observations (Advanced Very High Resolution Radiometer, AVHRR) on 13 May 2012 revealed that the eastern part of Atka Bay was still ice-free (Figure 5a) because of several storms pushing offshore the newly formed sea ice. Sea-ice surface temperatures derived from the same instrument confirmed this observation, as temperatures were higher there. However, TerraSAR-X imagery (Figure 5b) suggests that fast-ice covered the whole Bay at 31 May 2012.

During a storm in August 2012, a breakup event occurred where about 144 km² of sea ice in the central Bay drifted away in westward direction. We can only speculate about the causes of this event: a mixture of strong winds, tidal motion and probably icebergs touching the fast-ice edge could be responsible.

New sea ice started to form in the outbreak area, but was pushed out of the Bay regularly by coastal winds. It was not until the grounding of the large iceberg B15G in late September 2012, that a stable cover of newly formed sea ice was established (Figure 6). The iceberg left its position in front of the Bay about one year later, in early August 2013, drifting in westward direction.

A general overview of sea-ice conditions at Atka Bay, as well as positions of sampling sites, sea-ice ramp and the Neumayer III base, is presented in Figure 8.

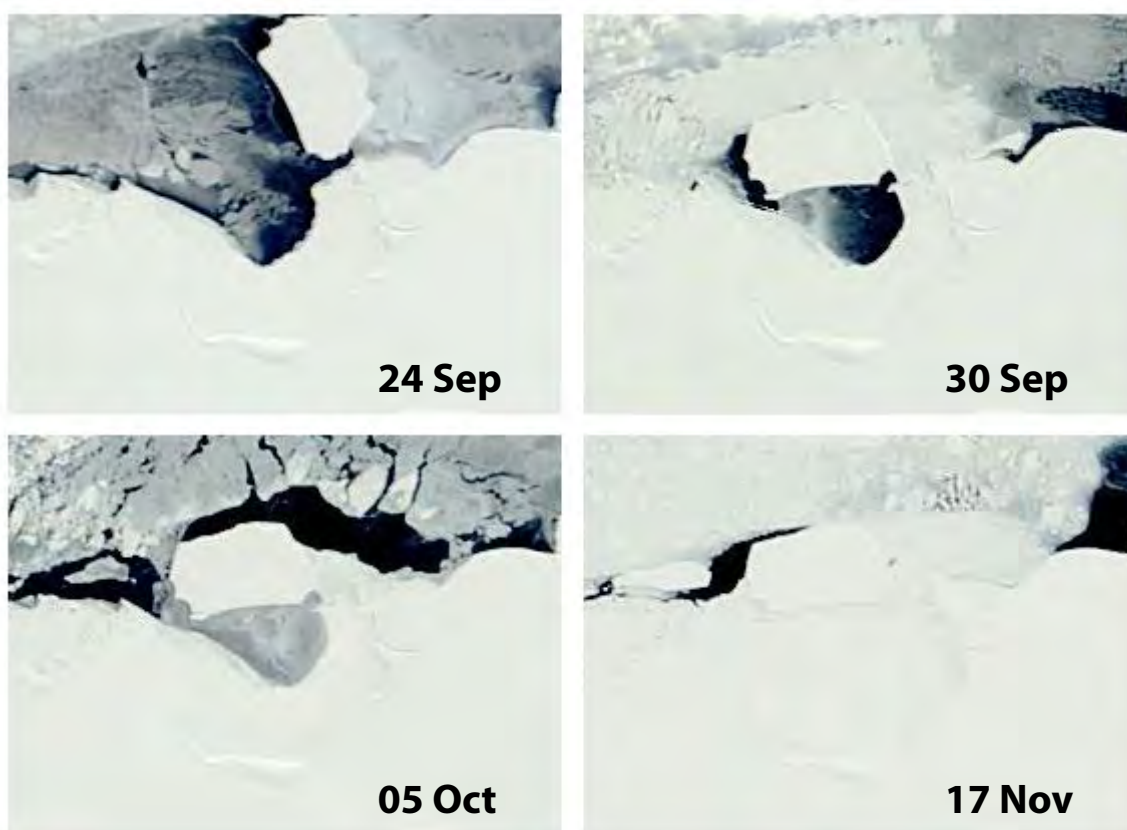


Figure 6: MODIS satellite images from September to November 2012. Iceberg B15G grounded in front of the Bay between 27 and 29 September 2012, and still has not moved at the time of writing (March 2013). At the beginning of November, the new sea ice was snow covered.

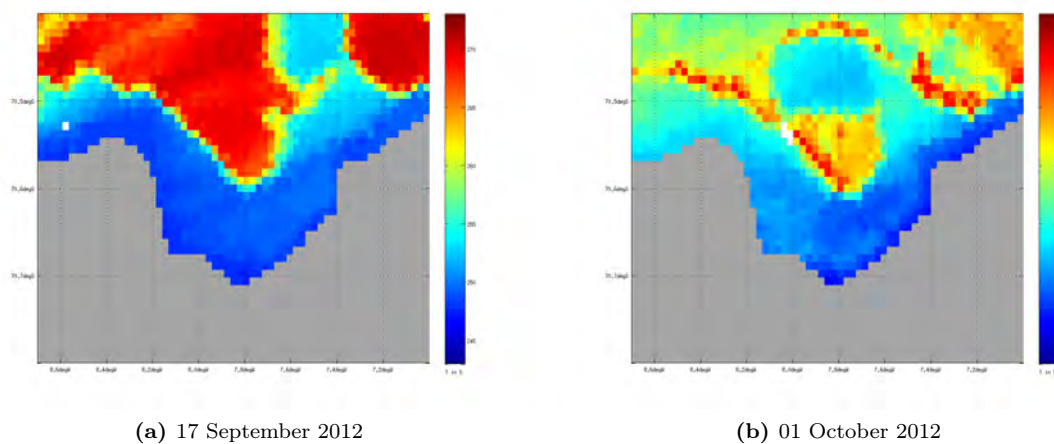


Figure 7: MODIS derived surface temperature images (IST) of the Atka Bay

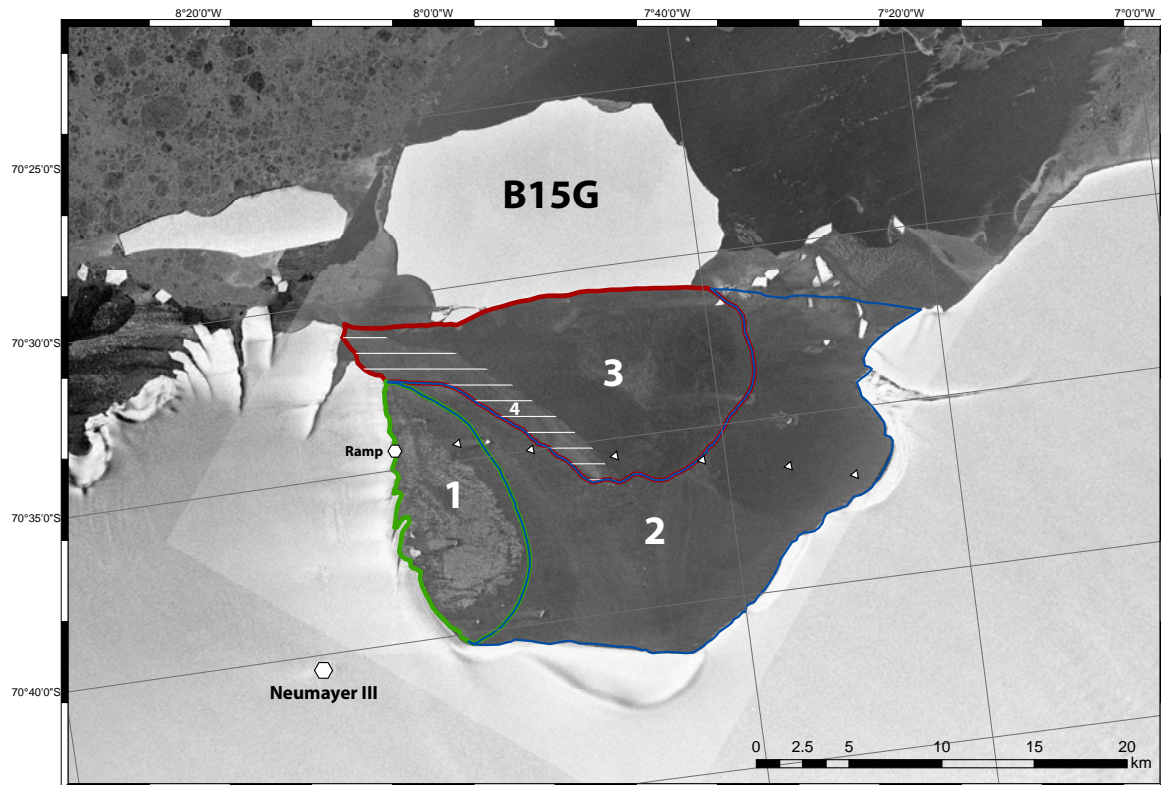


Figure 8: Sea-ice conditions at Atka Bay (TerraSAR-X, 15 and 23 November 2012); ©DLR 2012; 1 A mix of deformed second-year sea ice and sea ice grown from mid March 2012; 2 Mainly thermodynamically grown first-year sea-ice (since end of March / early April); 3 Thermodynamically grown sea ice formed in late August, after the outbreak event on 20 August; 4 Deformed sea ice also grown since late August, but pushed to the west by easterly winds. The white triangles symbolize sampling sites frequently visited during AFIN measurements and SIMBIS field campaign.

5. Sea-Ice Thickness, Snow Depth, Freeboard and Sub-Ice Platelet Layer

On **14 June 2012**, the first drill-hole measurements were performed at sampling sites ATKA03 and ATKA07, at ambient temperatures around -35°C (Figure 9). In addition, we obtained electromagnetic sea-ice thickness data with a Geonics EM31 Mark II (see section 6.1).

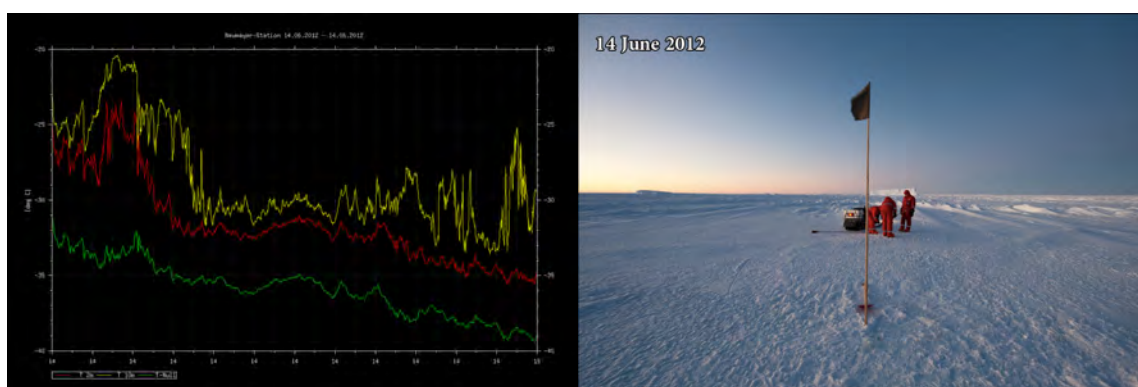


Figure 9: 14 June 2012, the day of first drillings. **Left:** Temperatures at Neumayer III. **Right:** Photo of sea ice at ATKA03 (Thomas Schmidt).

In addition to the low temperatures, a very rough sea-ice surface with minimal snow cover, extending at least 7 km into the Bay, hampered traveling across Atka Bay by snowmobile.

Sea-ice thickness in a distance of 50 m from the ramp was measured as 150 cm. The general sea-ice conditions at ATKA03 (3 km from the ice-shelf edge) were very inhomogeneous, consisting of distinct mid-size floes frozen together. A floe with a homogeneous surface was chosen for the drillings (Figure 9), which revealed a sea-ice thickness of 148 cm and a freeboard of 17 cm.

A drilling site with similar properties was chosen at ATKA07, and sea-ice thickness was determined as approximately 200 cm. During drilling, cavities were noticed inside the ice, indicating rafted floes. We were not able to drill through the entire thickness because we only had two auger flights with us, expecting thinner sea ice at this early stage. Ice platelets were not observed in any of the 6 boreholes.

On **16 June 2012**, measurements were performed at ATKA11 and ATKA16, where the sea-ice surface was generally much smoother than in the western part. But sea-ice thicknesses of this potentially thermodynamically grown sea ice ranged between 130 - 200 cm and 74 - 125 cm at ATKA11 and ATKA16, respectively, with minimal snow cover. These large thicknesses at this time of the year indicated that other mechanisms, probably mainly

dynamic growth conditions, contributed to a large extent to sea-ice growth.

Halfway between ATKA11 and ATKA16, one of our Nansen sleds took heavy damage. We made four final drillings which yielded sea-ice thicknesses between 96 and 120 cm with minimal snow cover. We returned to the station and recovered the broken sled on the next day.

On **30 June 2012**, we were able to conduct a complete survey of the sea-ice conditions on the Bay, performing five drillings at each of the six stations, recording temperatures, GPS coordinates as well as taking photos and water samples. A layer of “slush” was noticed below the fast ice, and platelets were observed in the boreholes. The sea-ice surface was distinctly more even east of ATKA11, in contrast to the frozen pack ice to the west. Between ATKA07 and ATKA11, a large area of even, homogeneous sea ice was chosen to deploy our automatic weather station, four radiometers and a thermistor chain. This location (denoted ATKA08, or AWS site) seemed to be the best compromise between representative sea-ice growth history on the one hand, and accessibility on the other. The deployment of our sensors is described in detail later in this report.

On **23 July 2012**, the regular measurements were successfully conducted along the entire profile for the second time, the only change being the relocation of the drilling site at ATKA07 to the AWS site at ATKA08.

We used a modified thickness tape (heavy metal bar with cord at one end) to better estimate the thickness of the sub-ice platelet layer (Figure 10). However, we often experienced difficulties in recovering the modified thickness tape because the metal bar got stuck in the ice/platelets interface. Therefore, we recommend to use an ordinary thickness tape to determine the sea-ice thickness.

In five holes at ATKA08, the mean sea-ice thickness was 182 cm, and the thickness of the sub-ice platelet layer was determined to range between 180 m and 238 cm, with a mean of 211 cm.

On **27 August 2012**, a large area of open water was encountered at 70°35,083'S 7°55,129'W, a few hundred meters before ATKA08. As a consequence, the sensors previously deployed at ATKA08 were lost. This event is covered in detail in section 10. Because of safety reasons further measurements were immediately canceled.

Safety considerations and bad weather made another sea-ice survey impossible until **22 September 2012**, when a complete EM transect of Atka Bay was conducted. This time, we started our drillings at ATKA24. Unfortunately, the modified platelet gauge broke after the 3rd drilling, making further platelet-layer thickness measurements impossible. The part of the sea ice that broke out in August was still ice-free over a large area, with only a small fraction of (inaccessible) thin sea ice on the western edge. For that reason, the drilling site

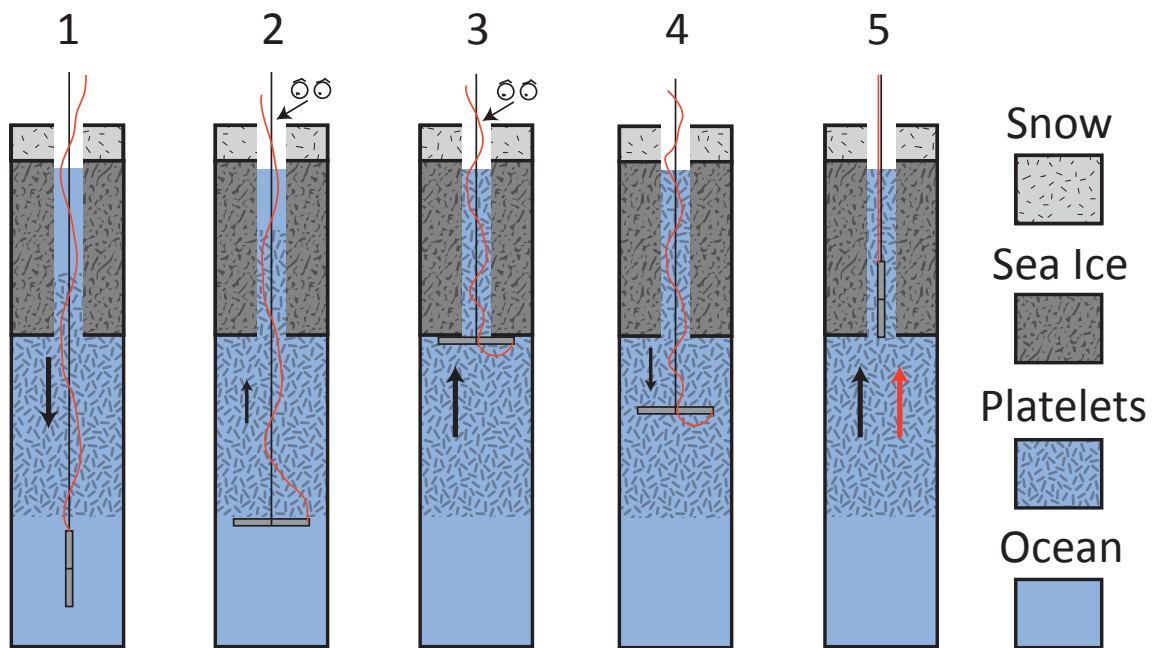


Figure 10: Measuring platelet layer thickness with a modified thickness tape. 1) A heavy metal bar penetrates the platelet layer. In situations with very dense accumulations, it takes several tries to achieve this. 2) The bar is pulled up gently to “feel” a resistance at the bottom of the sub-ice platelet layer. 3) The bar is pulled through the platelets until it reaches the sea-ice bottom. 4) The bar sinks down again. 5) The cord which is fastened at the end is pulled to recover the bar.

of ATKA11 was relocated to the southern edge of the ice-free area and denoted ATKA11b, revealing a mean sea-ice thickness of 286 cm. Because of the low temperatures, we skipped the drillings at ATKA03 and ATKA07. These were completed two days later.

On **17 November 2012**, the last sea-ice survey before the start of the SIMBIS campaign was conducted. In the meantime, the new sea ice had grown to a thickness of about 70 cm, so the original transect defined before the outbreak was resumed.

During the SIMBIS campaign, we also performed most of our activities at the predefined sampling sites. We extended our drillings and EM surveys by CTD casts, snow pits and optical measurements. A lot of unsorted thickness data were recorded at all sampling sites over the period of the campaign, most of which are not shown here. Nevertheless, systematic drillings were repeated at all stations on **13 December 2012** and **7 January 2013**.

Sea-ice conditions were still stable at the end of January. We were able to perform the last series of drillings for this season at ATKA03 and ATKA07 on **30 January 2013**.

Figure 11 provides sea-ice thickness, snow depths, freeboard as well as platelet-layer thickness as measured in 2012 and 2013 at the six ATKA stations.

It is evident from the data in Figure 11 that

- a) **sea-ice thickness** was already well over 1 m in the west at the start of the monitoring, has a maximum at ATKA07 and is most variable at ATKA07 and ATKA16;
- b) **sea-ice growth rate** strongly declines in October;
- c) **platelets** accumulate as early as July;
- d) **platelet-layer thickness** has a maximum in December, is largest in the west and lowest in the east (not counting ATKA11);
- e) **snow depth** is very inhomogeneous, with maxima at ATKA07 and ATKA16;
- f) **snow** is absent at ATKA03 and ATKA24, while at ATKA11 it is converted to snow ice in December;
- g) **freeboard** is predominantly positive;

The “sub-ice platelet layer”, which is the pronounced mushy layer below the solid sea ice, was observed at the end of June 2012 at nearly all sampling sites. Ice platelets quickly filled bore-holes, and severely hampered all under-ice irradiance and CTD measurements performed during the SIMBIS campaign. Shapes and sizes of these platelets varied greatly. Most of them got crushed during drilling of the holes. The largest specimen were bigger than 12 cm (Figure 12) top). Often it took more than 10 minutes to make single bore-holes accessible for measurements. In addition, from November on the seawater at most sites showed the distinct brown color of a diatom bloom.

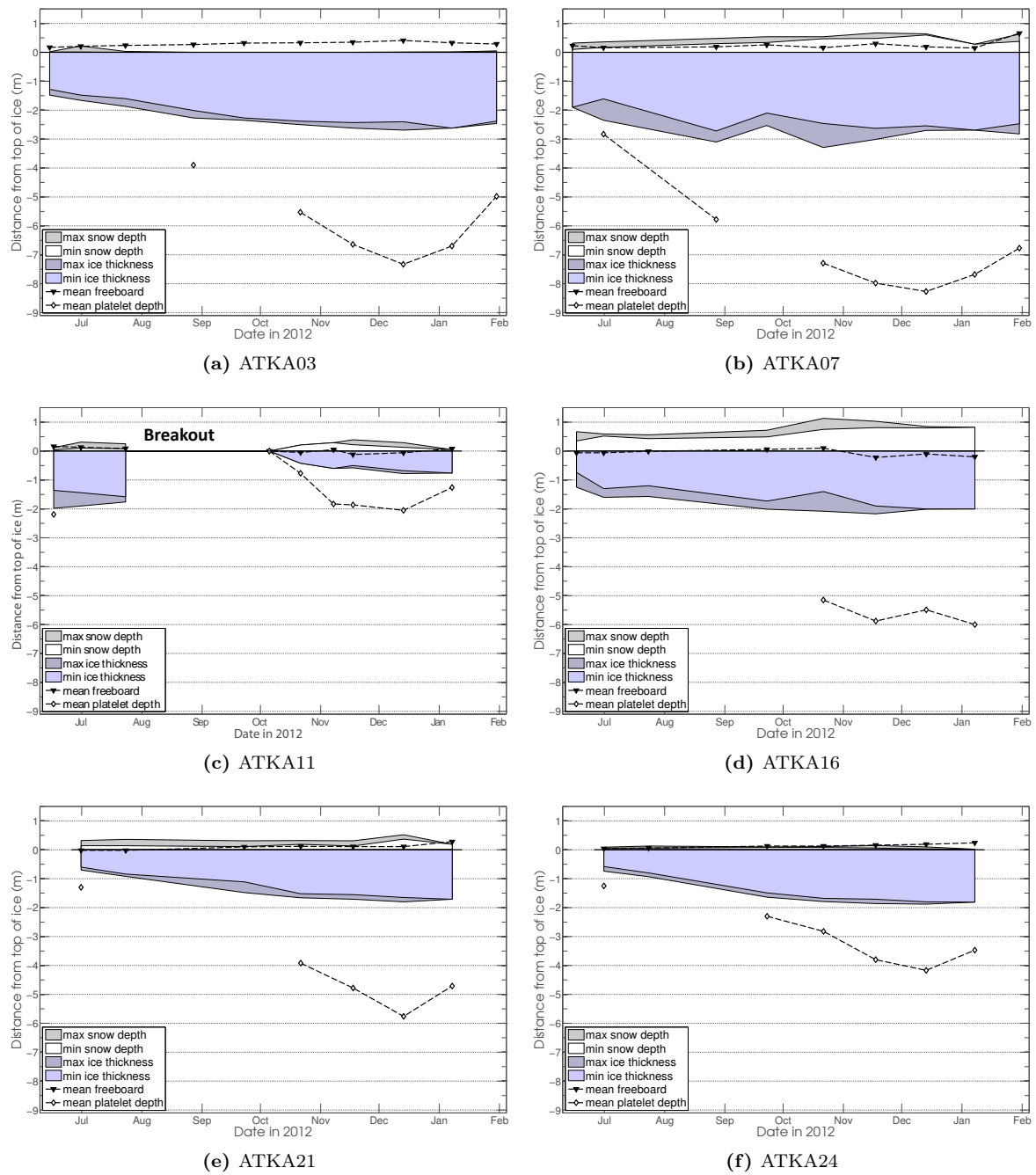


Figure 11: Results of AFIN drillings in 2012/13. Minimum and maximum values of snow depth and sea-ice thickness are given, as well as mean values of freeboard and platelet-layer thickness. Please note that data at ATKA11 are taken after the outbreak event in August, and therefore the values for sea-ice and platelet-layer thicknesses are significantly lower. Data from alternative stations to ATKA11 are not shown here because they were not visited regularly.



Figure 12: Top: Ice platelets found in coreholes. **Bottom:** During most of our drillings between November 2012 and January 2013, platelets and water of distinct brown color were observed. Photos: Mario Hoppmann

6. Electromagnetic Sea-Ice Surveys

6.1. Single-frequency Electromagnetic Device EM-31

We recorded a series of electromagnetic thickness profiles along a transect including the regularly visited study sites. This section summarizes the instrument setup, presents first results and highlights some key problems we had during operation of the device.

The instrument we used for our surveys was the newer version of the EM31 by Geonics (EM31-MK2). It was the first time we operated the device, and we had no opportunity to test it prior to the shipment to Neumayer. Some modifications were necessary for the use on the sea ice, which were prepared in April and May 2012.

The instrument was mounted in a kayak in vertical mode, with buttons on the control unit facing upwards (in contrast to horizontal mode, where buttons face sideways). A custom-made power supply (7.2Ah 12V battery with a voltage divider to +6 and -6 Volt) was mounted next to the instrument.

Two field PCs were used to record the data:

1. An Allegro field PC by Juniper Systems was connected to the EM31 via Bluetooth, and to a GPS via serial port.
2. An Archer field PC also by Juniper Systems was connected to the EM31 via serial port. A second GPS independently recorded position data.

The system was tested successfully in the freezer room at -25°C in early June 2012. On 15 June 2012, the EM31 was tested outside the station overnight, at temperatures as low as -40°C . But after 1 hour, both field PCs lost the connection to the instrument. However, a first sea-ice thickness survey was planned the following day, at temperatures between -25 and -30°C . But after startup of the EM31 at the sea-ice ramp, both field PCs were not able to communicate with the EM31 again. Back at the station, communication was possible again. We concluded that the EM31 seems not to work after a cold start at temperatures well below -25°C . In addition, the Bluetooth connection always failed at these low temperatures.

On 06 July 2012, the first electromagnetic thickness data of sea ice were obtained between the sea-ice ramp and ATKA07 (Figure 15 a). Snow depths were manually measured in parallel. Temperatures were around -22°C , and the instrument was already started in the station to prevent a malfunction due to cold start. In addition, the kayak was better insulated against the cold. But the Bluetooth connection of the Allegro field PC still failed. The EM data recorded by the Archer field PC was later merged with position data recorded by the second GPS. A Matlab routine was used to interpolate both EM- and position data to 1 s intervals, and merge them with the help of their timestamp. This procedure was applied to all datasets. Calibrations were conducted on 06.07.2012 and 07.11.2012. Total thickness was calculated from apparent conductivity by a single exponential fit to the calibration data (Figure 14 and Table 1).

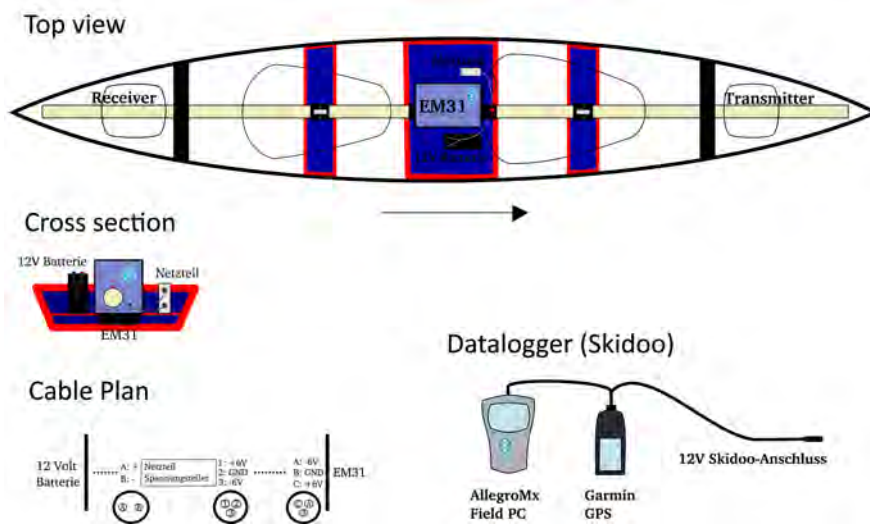
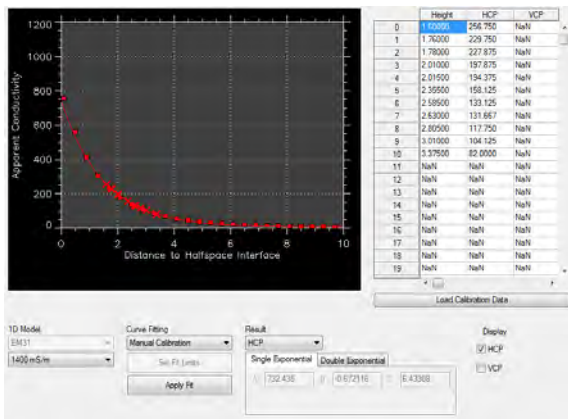
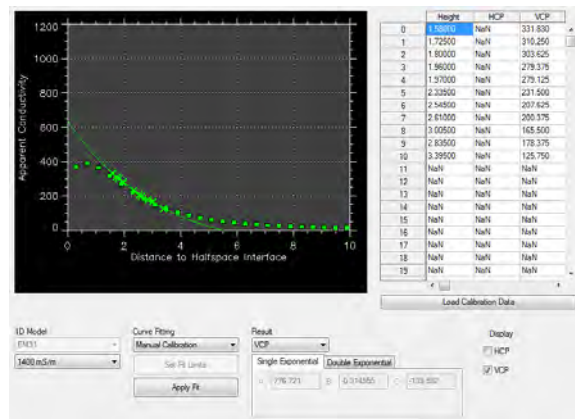


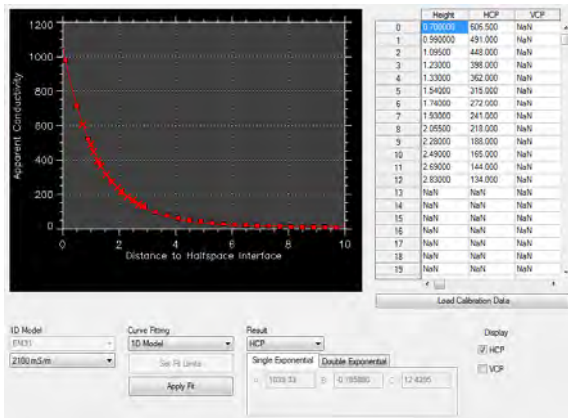
Figure 13: Set-up of EM31 in the kayak. Photo: Priska Hunkeler



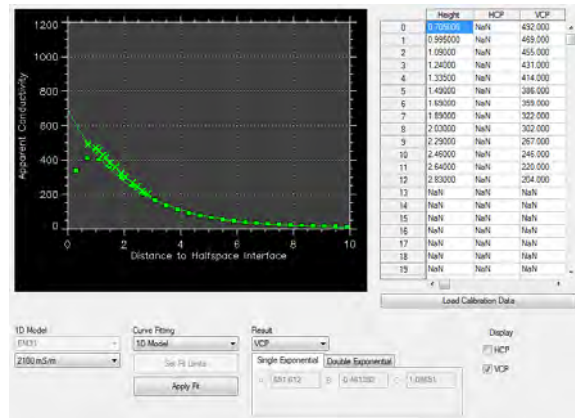
(a) 06.07.2012, HCP



(b) 06.07.2012, VCP



(c) 07.11.2012, HCP



(d) 07.11.2012, VCP

Figure 14: Calibrations of EM31 in horizontal and vertical mode

Table 1: Calibration dates and coefficients of single exponential fit.

Calibration date	Mode	A	B	C	Comment
06.07.2012	VCP	776,721	-0,314955	-13,959	manual curve
	HCP	732,435	-0,672116	6,433	manual curve
07.11.2012	VCP	691,612	-0,461392	10,865	1D model (2100 mS/cm)
	HCP	1039,330	-0,78589	12,430	1D model (2100 mS/cm)

Figure 15 and Table 2 give an overview of all EM31 transects obtained during 2012/13 with calibrations according to the second column of Table 2. One dataset (03.01.2012) is not shown as a map because the GPS track was not recorded.)

Table 2: Overview of EM31 data in 2012. VCP=Vertical CoPlanar mode, HCP=Horizontal CoPlanar mode

Date	Mode	Calibration
06.07.2012	VCP	06.07.2012
10.08.1012	VCP	06.07.2012
22.09.2012	VCP, HCP	06.07.2012
21.10.2012	VCP,HCP	06.07.2012
17.11.2012	HCP	07.11.2012
03.01.2013	HCP	07.11.2012
30.01.2013	HCP	07.11.2012

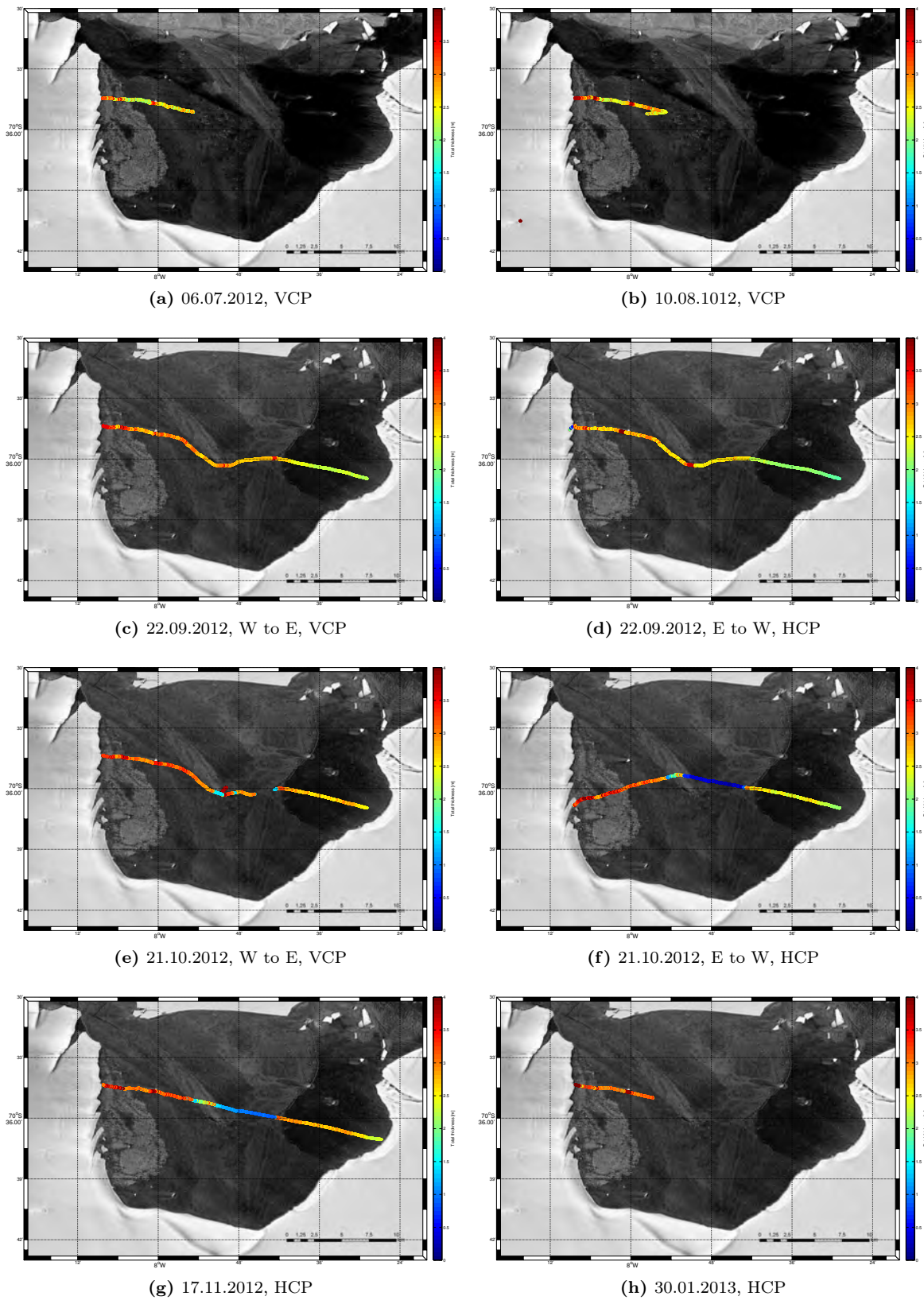


Figure 15: EM31 tracks color-coded with calculated total thickness. W=west, E=east, VM=vertical mode, HM=horizontal mode

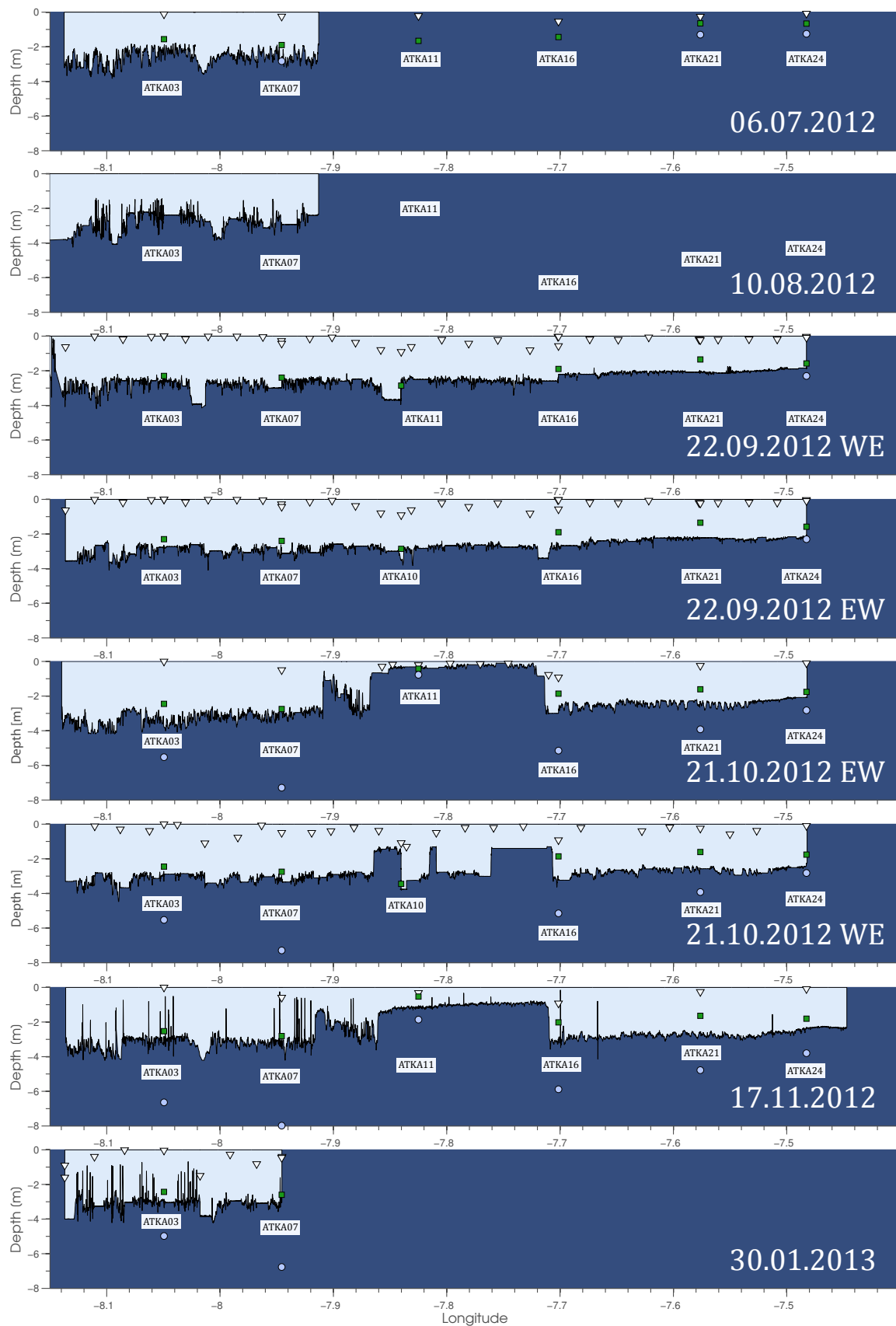


Figure 16: Profiles of EM31 surveys: the filled area (bright blue) represents EM31 total thickness; the triangles indicate simultaneously measured snow depths; the green squares are sea-ice thicknesses from regular drillings; the blue circles represent platelet layer depths.

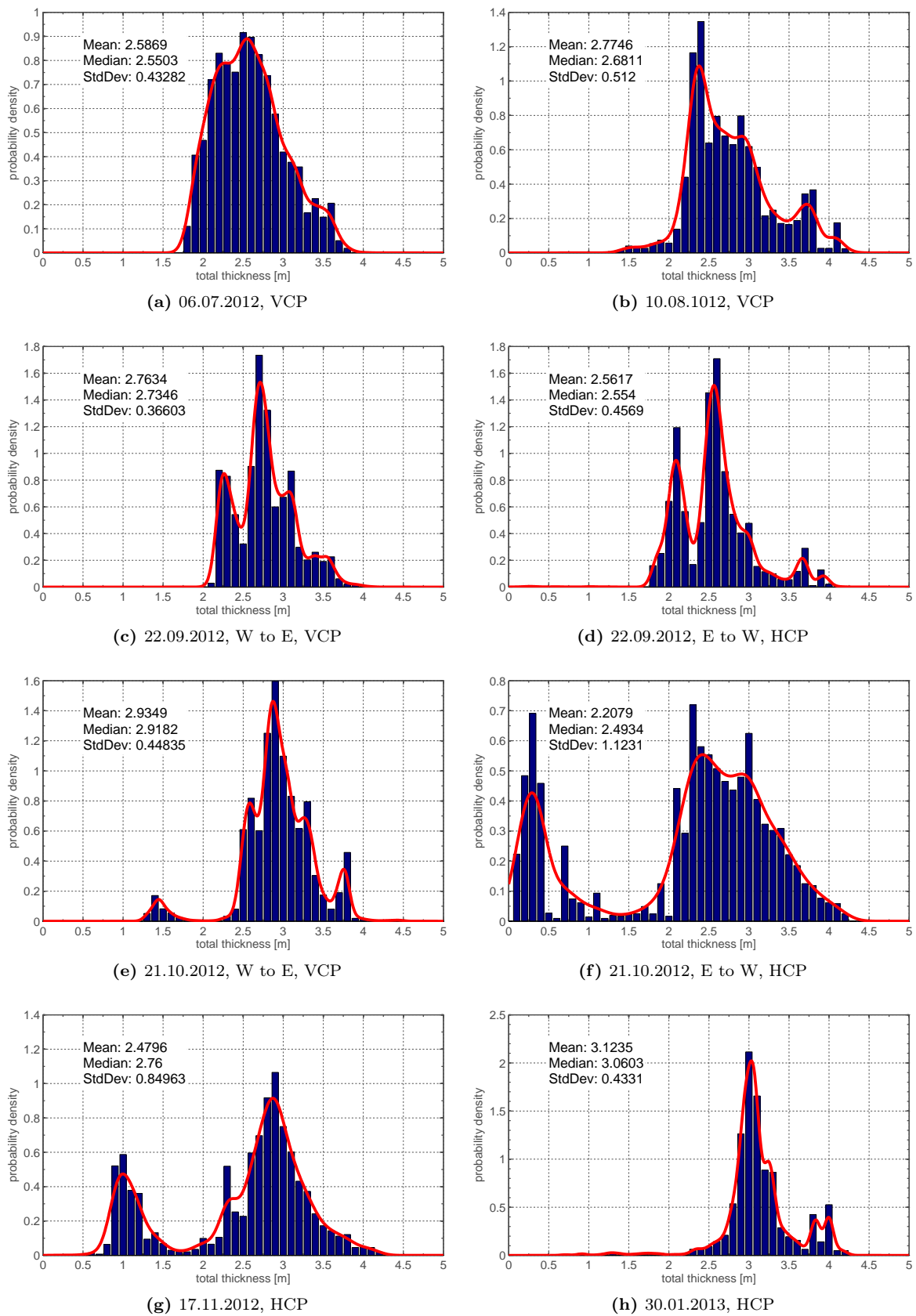


Figure 17: Probability density functions of EM31 data. W=west, E=east, VCP=Vertical CoPlanar mode, HCP=Horizontal CoPlanar mode

6.2. Multi-frequency Electromagnetic Device GEM-2

During our SIMBIS field campaign, we operated the multi-frequency GEM-2 in addition to the one-frequency EM31 described in section 6.1) for the first time on Antarctic landfast sea ice. The goal of our study was to gain information on the sub-ice platelet layer by combining data from different frequencies, ideally to be able to determine its thickness distribution. The GEM-2 coils are spaced apart 1,67 m and the sampling rate was 30 Hz. In table 3 all the different GEM-2 measurements are summarized, grouped with respect to the type of measurement. The larger scale measurements are shown as an overlay of the TerraSAR-X image of Atka Bay in Figure 18.

Table 3: Summary of data. 1) Measuring the influence of kayak and handheld computers, 2) Noisy signal due to a watch, 3) Averaging test, 4) 50 m, drift test, drilling information available, 5) 28 x 60 m, walking, drilling information available, 6) Sea Ice ramp - Atka 24, 7) Sea Ice ramp - Atka 24, 8) Atka 24 - Pingi ramp, 9) North - South, 10) ATKA03 - IMB32, 11) SNOW2 - Pingi ramp, 12) Grids with kayak

Location	Date	Mode	Frequencies [Hz]	Filename	Com.
Drift and noise					
Shelf ice	20.11.12	HCP	475, 1525, 5325, 18325, 63025	14-d-20No-508_GEM	
Shelf ice	20.11.12	HCP	475, 1525, 5325, 18325, 63025	15-d-21No-00a_GEM	
ATKA24	16.12.12	HCP	1530, 5310, 18330, 63030, 93090	81-xg-16de-09c_GEM - 82-d-16De-055_GEM	1
Calibration by lifting the instrument					
ATKA11	21.11.12	HCP, VCP	475, 1525, 5325, 18325, 63025	23-d-21No-0a8_GEM	
ATKA11	26.11.12	HCP, VCP	5310, 18330, 63030, 93090	49-d-26No-0b0_GEM - 52-d-26No-0e8_GEM	2
ATKA24	26.11.12	HCP, VCP	5310, 18330, 63030, 93090	58-d-26No-0e4_GEM - 62-d-26No-132_GEM	
ATKA11	01.12.12	HCP, VCP	450, 1530, 5310, 18330, 63030	72-d-30No-35a_GEM - 73-xg-30no-3de_GEM	
ATKA11	01.12.12	HCP, VCP	5310, 18330, 63030, 93090	74-xg-30no-48e_GEM - 75-d-30No-000_GEM	
ATKA03	27.12.12	HCP, VCP	1530, 5310, 18330, 63030, 93090	95-d-27De-23e_GEM	
ATKA11	27.12.12	HCP, VCP	1530, 5310, 18330, 63030, 93090	98-d-27De-264_GEM	
Calibration with ferrite					
ATKA11	23.11.12	HCP	450, 1530, 5310, 18330, 63030	28-d-23No-00f_GEM	
ATKA11	23.11.12	HCP	450, 1530, 5310, 18330, 63030	32-d-23No-063_GEM	
ATKA11	26.11.12	HCP	5310, 18330, 63030, 93090	48-d-26No-098_GEM	
ATKA11	26.11.12	HCP	5310, 18330, 63030, 93090	54-d-26No-00f_GEM	
ATKA24	26.11.12	HCP	5310, 18330, 63030, 93090	56-d-26No-0a2_GEM	
Grid1	30.11.12	HCP	5310, 18330, 63030, 93090	64-d-29No-4ac_GEM	
Reference data					
ATKA03	21.11.12	HCP, VCP	475, 1525, 5325, 18325, 63025	16-d-21No-050_GEM -21-d-21No-09b_GEM	3
ATKA03	23.11.12	HCP, VCP	475, 1525, 5325, 18325, 63025	26-d-22No-3de_GEM	

ATKA03	23.11.12	HCP, VCP	18330, 38310, 80010	27-d-22No-44c_GEM	
Grid 1	30.11.12	VCP	5310, 18330, 63030, 93090	65-d-29No-4c3_GEM	
Transects and grids by walking, incl. reference measurements					
ATKA11 Transect	23.11.12	HCP, VCP	450, 1530, 5310, 18330, 63030	29-d-23No-024_GEM - 34-d-23No-099_GEM	4
Grid 1	30.11.12	HCP, VCP	5310, 18330, 63030, 93090	66-d-30No-000_GEM - 69-d-30No-029_GEM	5
Grid 1	30.11.12	HCP, VCP	450, 1530, 5310, 18330, 63030	70-d-30No-01a_GEM - 71-d-30No-04a_GEM	5
Transects and grids with kayak					
Transect 1	25.11.12	HCP	5310, 18330, 63030, 93090	07-d-25No-10e_GEM_Archer	6
Transect 1	25.11.12	HCP	5310, 18330, 63030, 93090	37-d-25No-078_GEM - 46-d-25No-020_GEM	6
Transect 2	16.12.12	HCP	1530, 5310, 18330, 63030, 93090	81-d-16De-09c_GEM	7
Transect 3	16.12.12	HCP	1530, 5310, 18330, 63030, 93090	83-d-16De-0a5_GEM	8
Transect 3	20.12.12	HCP	1530, 5310, 18330, 63030, 93090	85-d-16De-0ff_GEM - 86-d-16De-020_GEM	9
Transect 4	21.12.12	HCP	1530, 5310, 18330, 63030, 93090	90-d-21De-080_GEM	10
Transect 5	21.12.12	HCP	1530, 5310, 18330, 63030, 93090	93-d-21De-428_GEM	11
ATKA03 grid	21.12.12	HCP	1530, 5310, 18330, 63030, 93090	89-d-21De-2b2_GEM	12
IMB32 grid	21.12.12	HCP	1530, 5310, 18330, 63030, 93090	91-d-21De-352_GEM	12
SNOW2 grid	21.12.12	HCP	1530, 5310, 18330, 63030, 93090	92-d-21De-299_GEM	12
24 hour measurement					
ATKA21	03.01.13	HCP	1530, 5310, 18330, 63030, 93090	99-xg-03ja-1ed_GEM - 99-xg-04ja-0ab_GEM	

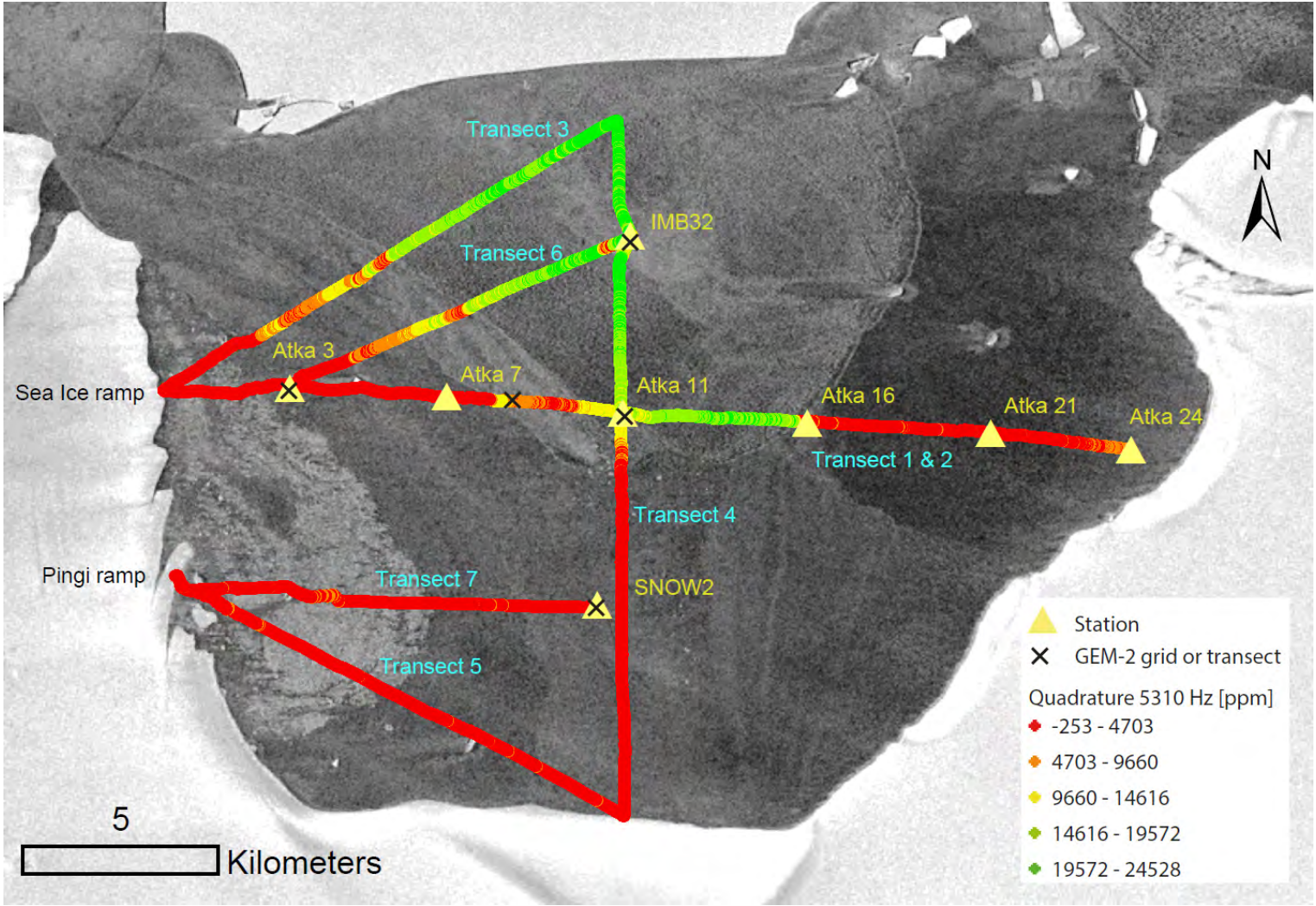


Figure 18: Overview of GEM-2 transects in the Atka Bay (Quadrature 5310 Hz) with a TerraSAR-X image from 27.11.2012 in the background

Drift and noise

For an understanding of the instruments noise and drift behavior, data were acquired on the shelf ice, where no conductive material is present. In figure 19 raw data in parts per million (ppm) of the primary field are shown. For all frequencies, the drift of inphase and quadrature do not exceed 110 ppm over a time period of 70 minutes (figure 20). In general, the quadrature is drifting less than the inphase component. The drift of both components, however, are smaller than the noise (figure 21).

Furthermore, the absolute values are shifted with respect to zero (figure 19). For the shelf-ice experiment the mean offset values for all frequencies are shown in table 4, where the highest offset is observed at 63025 Hz.

In order to understand the influence of the kayak and the small handheld computers (SoMo and Archer), data were acquired by changing these parameters (figure 22). In table 5 the influence of the kayak and both computers are summarized. The inphase is in general more sensitive to perturbations. The Archer computer, which was absent for calibration measurements, but used for kayak data acquisition, has the strongest influence on the data.

Table 4: Mean absolute offset values in ppm of individual frequencies during two 70 minutes shelf ice tests. I = Inphase, Q = Quadrature. Test 1: 35937 and Test 2 with 35286 (including peaks) data points.

Frequency [Hz]	Drift test 1		Drift test 2	
	I [ppm]	Q [ppm]	I [ppm]	Q [ppm]
475	734.2	-226.8	750.4	-233.9
1525	-240.9	-0.3	-228.8	4.6
5325	287.8	-154.6	306.7	-150.3
18325	-181.9	-607	-160.3	-603.6
63025	874.1	-2022.6	918.5	-2027.3

Table 5: Influence of kayak and field computers (SoMo and Archer)

Frequency	Influence of kayak (without SoMo)		Influence of Archer (GEM-2 in kayak)		Influence of SoMo (GEM-2 in kayak)	
	Q [ppm]	I [ppm]	Q [ppm]	I [ppm]	Q [ppm]	I [ppm]
1530	93.1	203.7	649.7	1957.5	354.8	304.1
5310	301.5	313.2	285.5	2226.1	322.7	675.9
18330	534.3	624.1	153.4	2324.9	188.0	867.9
63030	813.4	773.2	140.0	2405.7	158.6	967.1
93090	1015.6	608.5	143.7	2470.7	155.5	1027.5

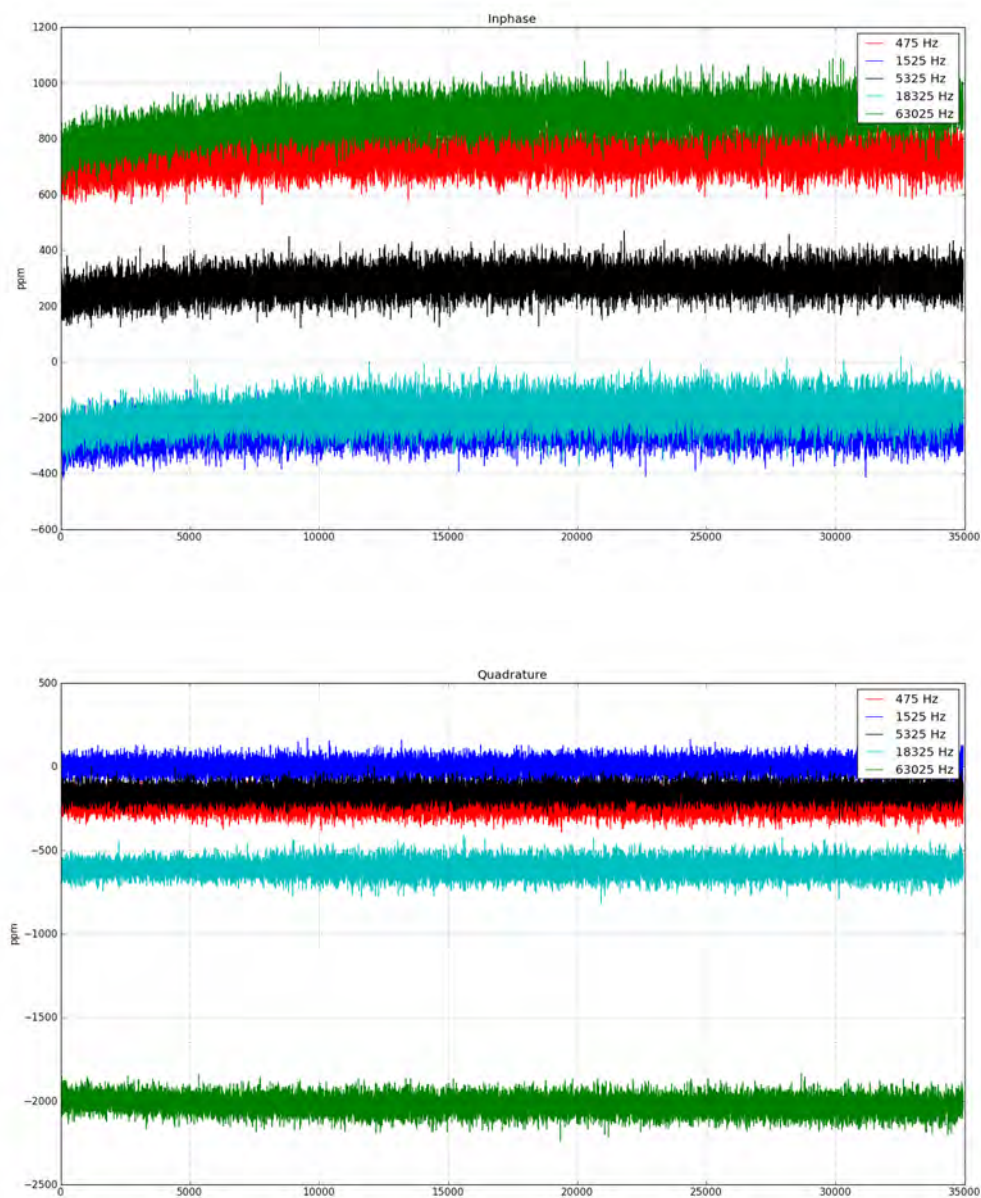


Figure 19: Inphase (top) and quadrature raw data (bottom) from a 70 minutes drift test on the shelf ice

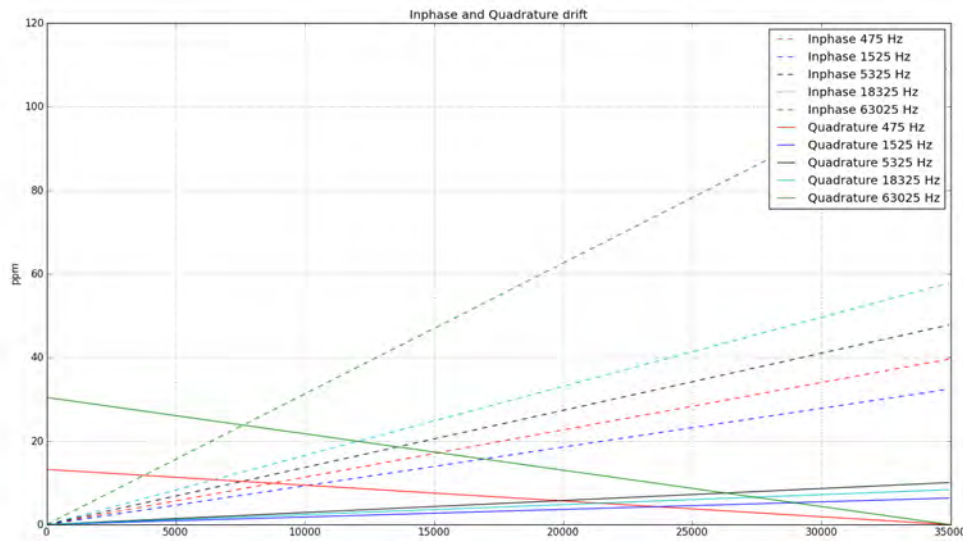


Figure 20: Drift of inphase and quadrature during a 70 minutes drift test on the shelf ice

Calibration

For calibration the device was lifted upwards in 10 cm steps in HCP (horizontal coplanar) and VCP (vertical coplanar) mode (Figure 23). The data from individual calibrations will be compared to a 1D forward model for both modes and the different frequencies. An example is shown in figure 24 for 5310 Hz in HCP mode at ATKA11. For the conductivity of water 2700 mS/m is assumed (section 13.1). Without a sub-ice platelet layer in the forward model the data points can not be explained (solid lines). Adding another layer for ice platelets results in a layer conductivity with values between 500 and 1000 mS/m.

Grids and Transects

In figure 23 some impressions of smaller and larger scale transect and grid data acquisition are shown. The data is summarized in table 3. Both West to East transects are compared in figure 26. The data from the second transect is noisier compared to the first one. This data will be compared to in-situ measurements. A grid example 28 x 60 m over three ridges is shown in figure 27. The location of the grid is shown in figure 18 between the stations ATKA07 and ATKA11. In figure 27(a) the basic features are summarized and in figure 27(b) the raw data from HCP mode, 5310 Hz are shown. The grid has to be reprocessed with respect to the grid cells as here imprecise GPS locations are plotted.

6.2.1. Stationary measurement over 24 hours

The GEM-2 was set to recording mode for 24 hours at one location (ATKA21, 03 January 2013). Only the quadrature component at very high frequencies (mainly at 93090 and 63030 Hz) showed a daily signal. In figure 28 the 24 hours data for the quadrature component at

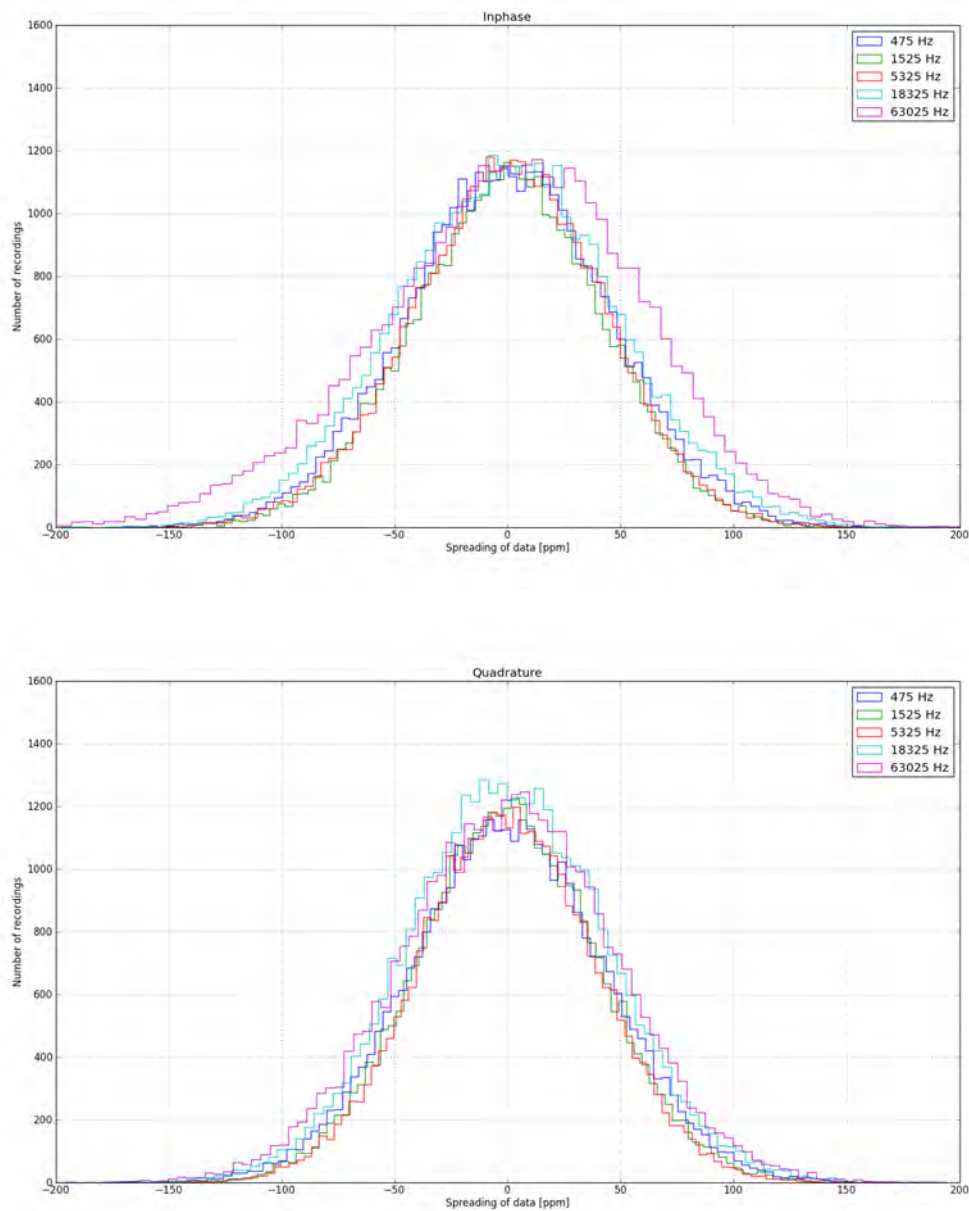


Figure 21: Noise distribution of inphase (top) and quadrature (bottom) during a 70 minutes drift test on the shelf ice

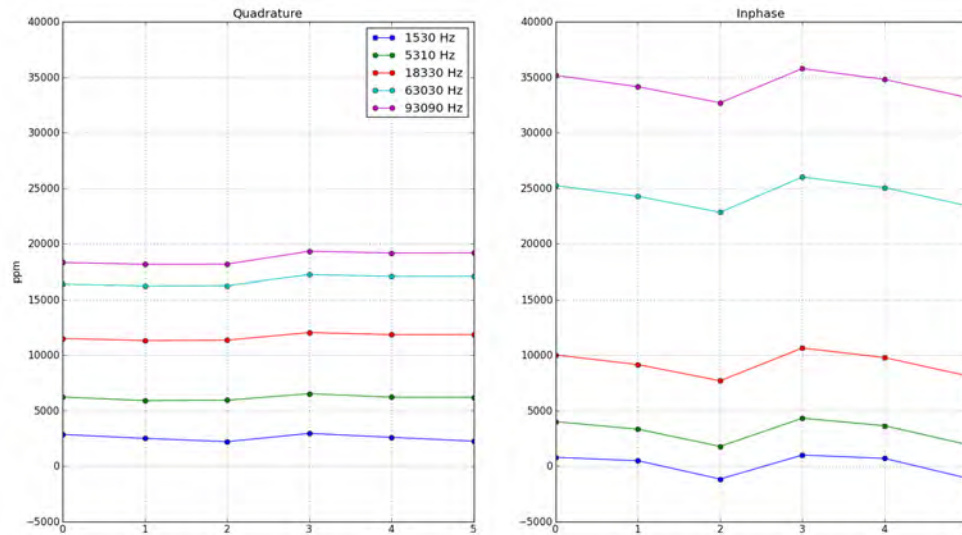


Figure 22: Influence of kayak and field PCs on GEM-2 signal at ATKA24, 16.12.2012. 1) GEM-2 on ice 2) SoMo field PC next to GEM-2 box, 3) Archer field PC next to GEM-2 box, 4) GEM-2 in kayak 5) GEM-2 in kayak, SoMo field PC next to GEM-2 box 6) GEM in kayak, Archer field PC next to GEM-2 box



(a)



(b)

Figure 23: Calibration in (a) HCP and (b) VCP mode. Photos: Uwe Baltes

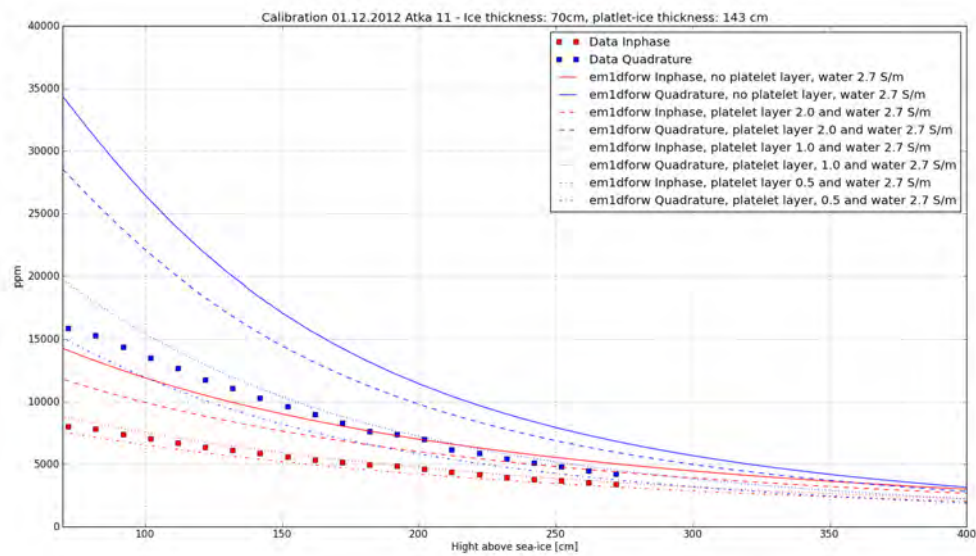


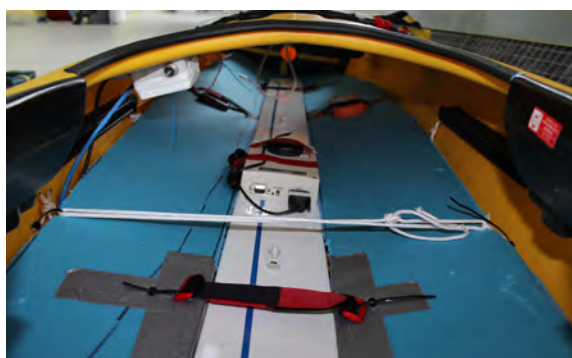
Figure 24: Calibration at ATKA11, 5310 Hz, HCP, 01 December 2012. A measurement was taken every 10 cm as lifting it up to 2 meters



(a)



(b)



(c)



(d)

Figure 25: Grids and Transects (a) GEM-2 next to a profile line, (b) GEM-2 transect over ridges, (c) GEM-2 installation in the kayak, (d) GEM-2 in the kayak during a transect. Photos: Priska Hunkeler, Mario Hoppmann

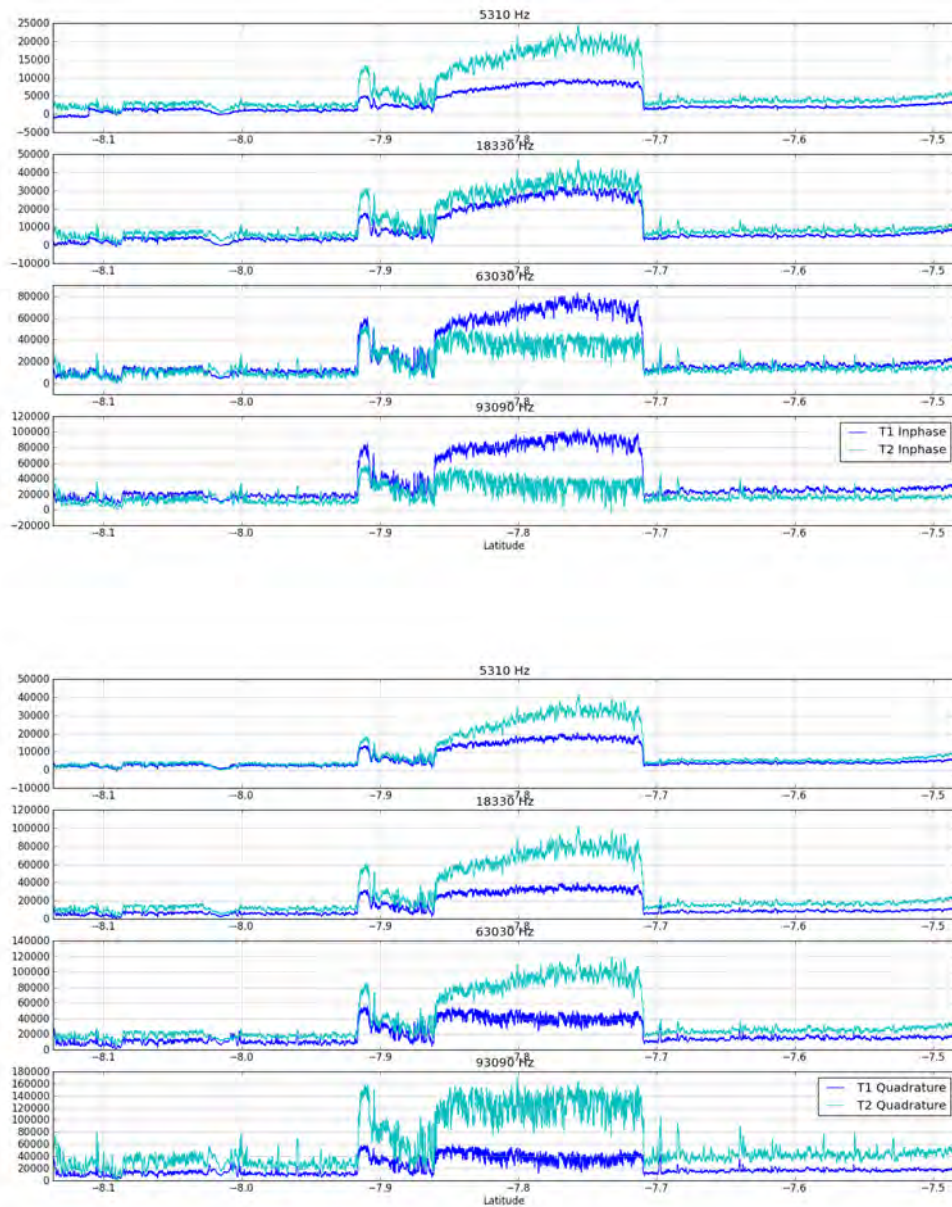
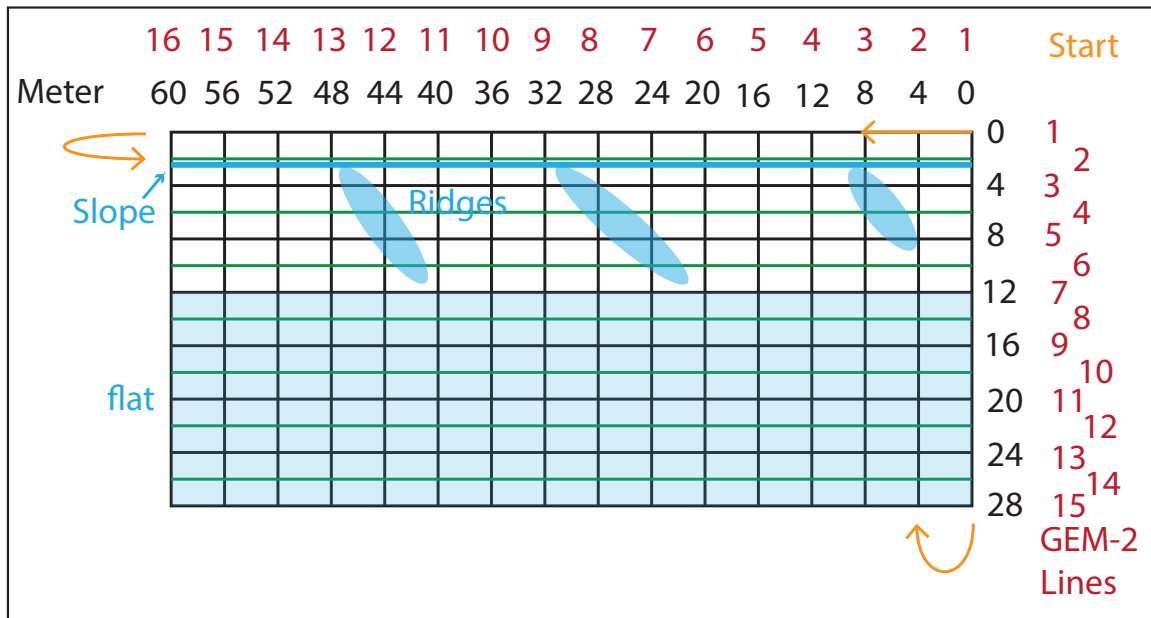
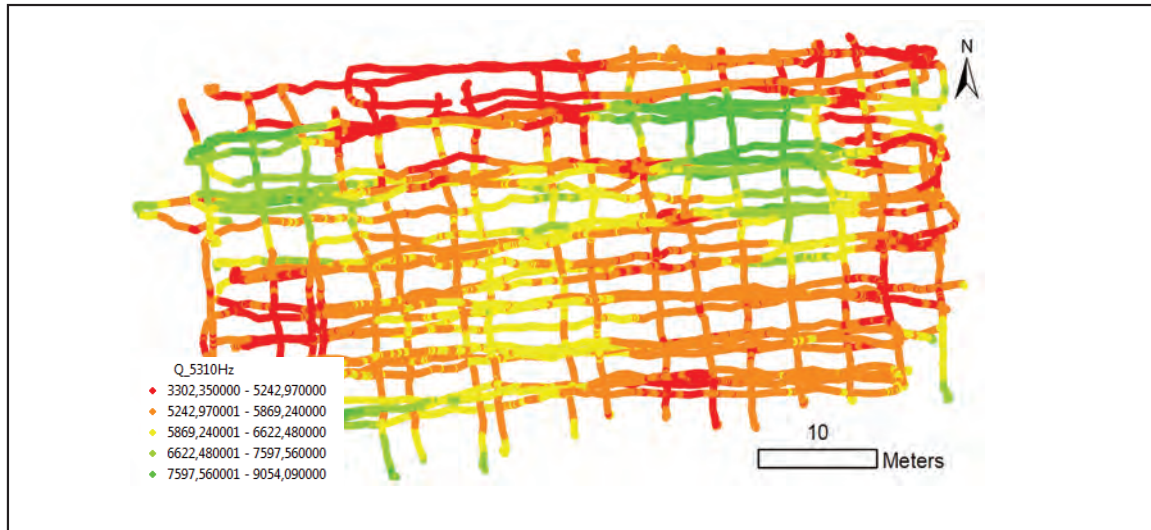


Figure 26: Comparison of the two West to East transects (top) Inphase, (bottom) Quadrature. T1 = Transect 1 (25.11.2012), T2 = Transect 2 (16.12.2012)



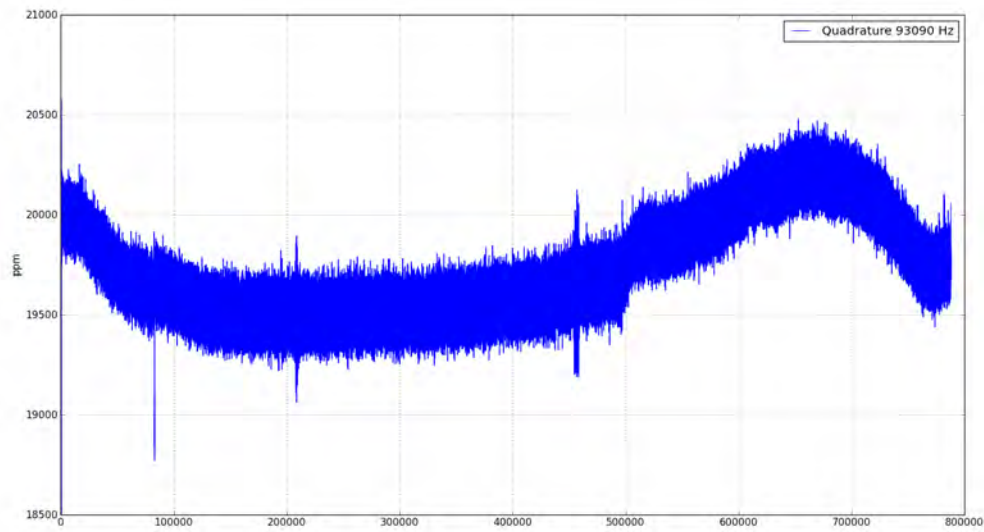
(a)



(b)

Figure 27: Grid between ATKA07 and ATKA11. (a) Basic features and GEM-2 lines, (b) Raw data, GPS locations (have to be reprocessed), 5310 Hz, HCP

93090 Hz are shown.



(a)

Figure 28: Stationary 24 hour measurement at ATKA21 on 03 January 2013.

Future work

The calibration data will be compared to different two layer cases with several conductivities for the platelet-ice layer. This will be done for every frequency, both modes and at every location. Error estimates will be calculated for all the different cases. With 1D inversion techniques the sea-ice and platelet-ice thickness as well as the typical electrical conductivity of the platelet ice layer will be simultaneously estimated. Data from simultaneous drillings, under-ice cameras and CTD profiles will be used to validate the EM data.

7. Atmospheric observations

During 2012, we deployed several autonomous instruments on two sites on the landfast sea ice, to automatically measure different parameters in high temporal resolution. Figure 29 shows their geographic location on the sea ice, while Table 6 provides an overview of these instruments.

In this section, we describe the deployment of each of these autonomous devices and present some first results.

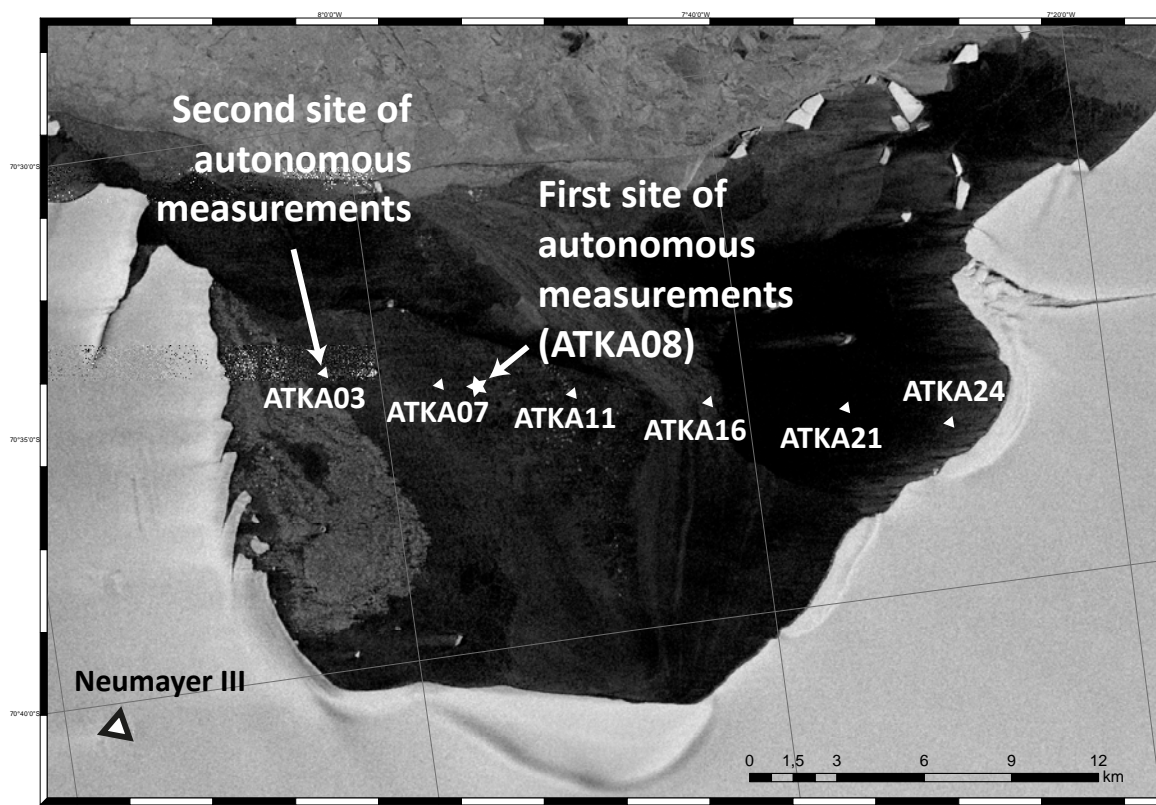


Figure 29: Sites of autonomous measurements (Background: TerraSAR-X ScanSar from 25 June 2012, ©DLR)

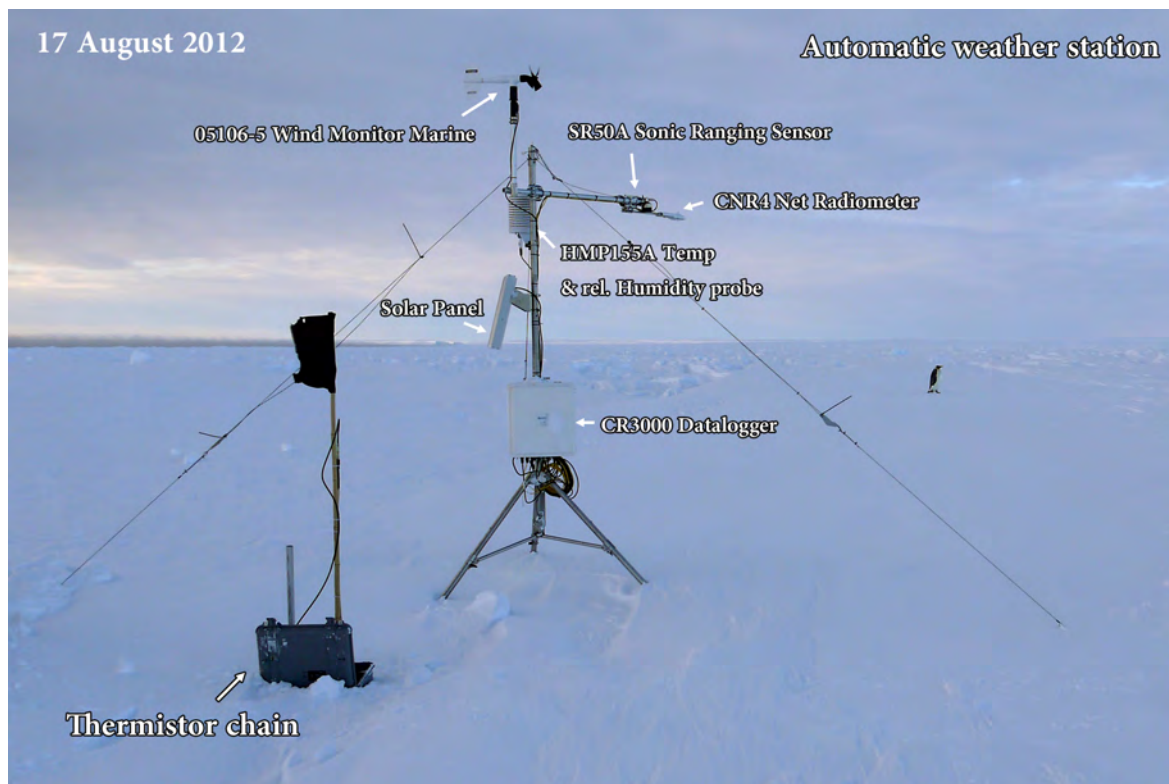
7.1. First Automatic Weather Station, July - August 2012

After our first observations of sea-ice conditions across Atka Bay during June 2012, we chose to deploy our autonomous instruments at a site of primarily thermodynamically grown ice, several kilometers away from the western ice-shelf edge.

On 06 July 2012, we deployed the first automatic weather station (AWS1) at 70.58559°S 7.91337°W , about 8 km from the western ice-shelf edge along last years transect (Figure 29). In this report, this site is referred to as ATKA08. As in 2011, the AWS was configured to measure temperature (2 m), relative humidity, barometric pressure, wind velocity, wind speed as well as downward and upward radiation and snow depth in 1-minute intervals.

Table 6: Overview of autonomous instruments deployed in 2012

Instrument	short	Deployment	Recovery
Automatic weather station	AWS1	06.07.2012	17.08.2012
Automatic weather station	AWS2	02.10.2012	27.12.2012
Radiation station (4 RAMSES ACC VIS)	RS1	10.08.2012	17.08.2012
Radiation station (3 RAMSES ACC VIS)	RS2	02.10.2012	30.12.2012
Sea-Ice Mass Balance Buoy	AWI01	10.08.2012	-
Sea-Ice Mass Balance Buoy	AWI31	21.11.2012	-
Sea-Ice Mass Balance Buoy	AWI32	13.12.2012	21.12.2012
Eddy Covariance Station	EC	21.11.2012	30.12.2012

**Figure 30:** Photo of automatic weather station, taken on 17 August 2012. Photo: Thomas Schmidt

In addition, a radiation station and a sea-ice mass balance buoy were later deployed at ATKA08. The respective instruments and their set-up are described in sections 8.3 and 9.1. A scheme of the resulting “superstation” at ATKA08 is given in Figure 31.

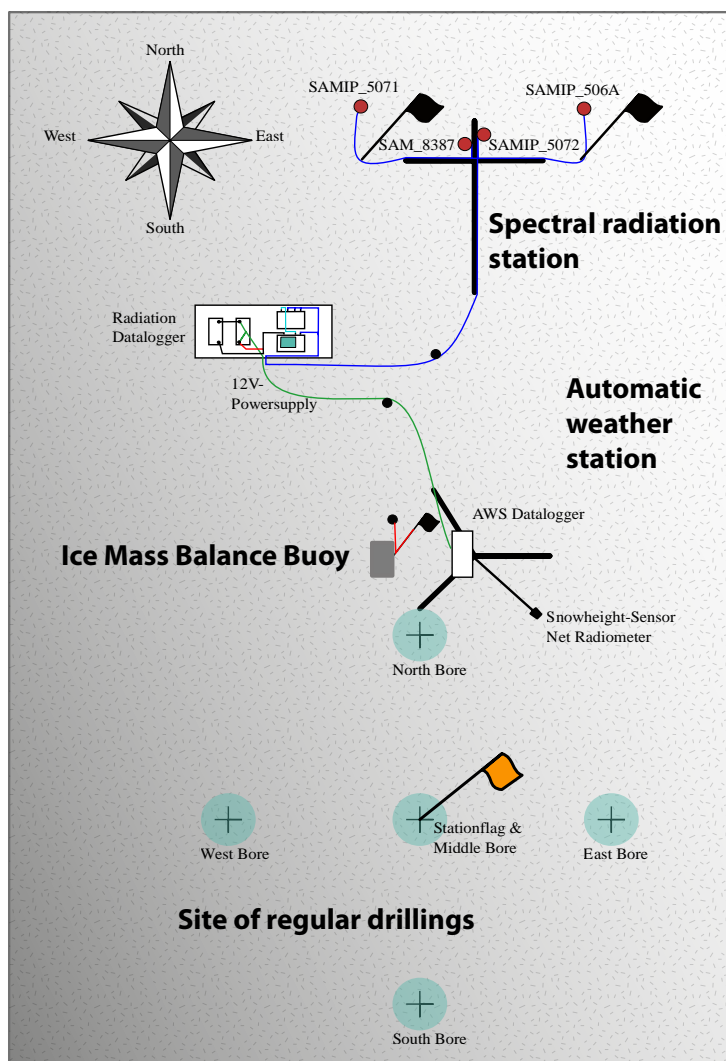


Figure 31: Scheme of autonomous measurement station

ATKA08 was visited several times in the following weeks, and AWS data was recovered from the CF-Card on 23 July, 10 August and 17 August.

AWS1, RS1 and AWI01 were lost on 20 August during a sea-ice break-up event (see section 10).

7.2. Second Automatic Weather Station, October 2012 - January 2013

Following the loss of the first “super-station”, a backup weather station (AWS2) was prepared at Neumayer III during the next weeks, and finally deployed at ATKA03 on 02 October 2012, in safe distance to the now open water at ATKA08. AWS1 was equipped with sensors identical in construction to AWS1.

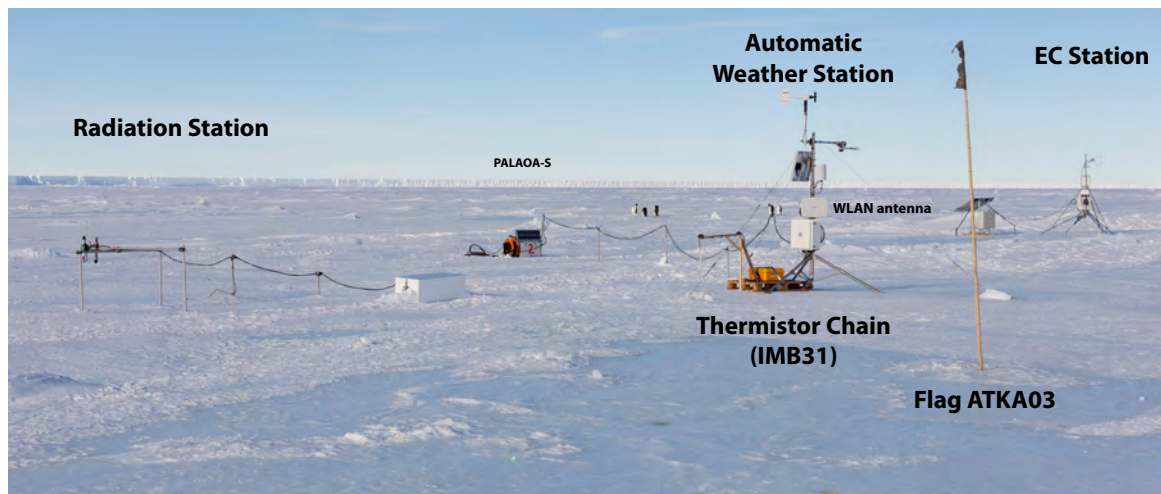


Figure 32: Instrument setup at ATKA03. Photo: Mario Hoppmann

A second radiation station was deployed at the new AWS site as well, of which a description is given in section 8.4. In addition, a second sea-ice mass balance buoy was frozen into the sea-ice at the beginning of the SIMBIS campaign at 21 November 2012. Please refer to section 9.2 for further information.

The final setup of the second “super-station” of autonomous measurements, this time at ATKA03, is shown in Figure 32 and as an aerial image in Figure 33.

At the same time, the mobile PALAOA-S box (PALAOA: “Perennial Acoustic Observatory in the Antarctic Ocean”), a hydrophone below the sea ice, was also set up at ATKA03 by the AWI Ocean Acoustics Group. This instrument was equipped with a solar-powered WLAN antenna to transfer its audio data to the Neumayer III station in real-time. We took the opportunity to test a wireless data transfer for our instruments by connecting our Campbell Scientific data logger as well as the Tribox II to this antenna. We were then able to establish a connection to our instruments in the local network (weather data: IP 192.168.31.72, radiation data IP 192.168.31.97). We made the weather data available in real time at <http://boreas.awi-neumayer.de/met/intranet/atkaaws.html>, the irradiance spectra were only available through the software TBremote admin.

Results of atmospheric measurements, irradiances and associated parameters, as well as snow depths as measured by the two AWS are presented in Figures 35, 35, 36 and 37, respectively.

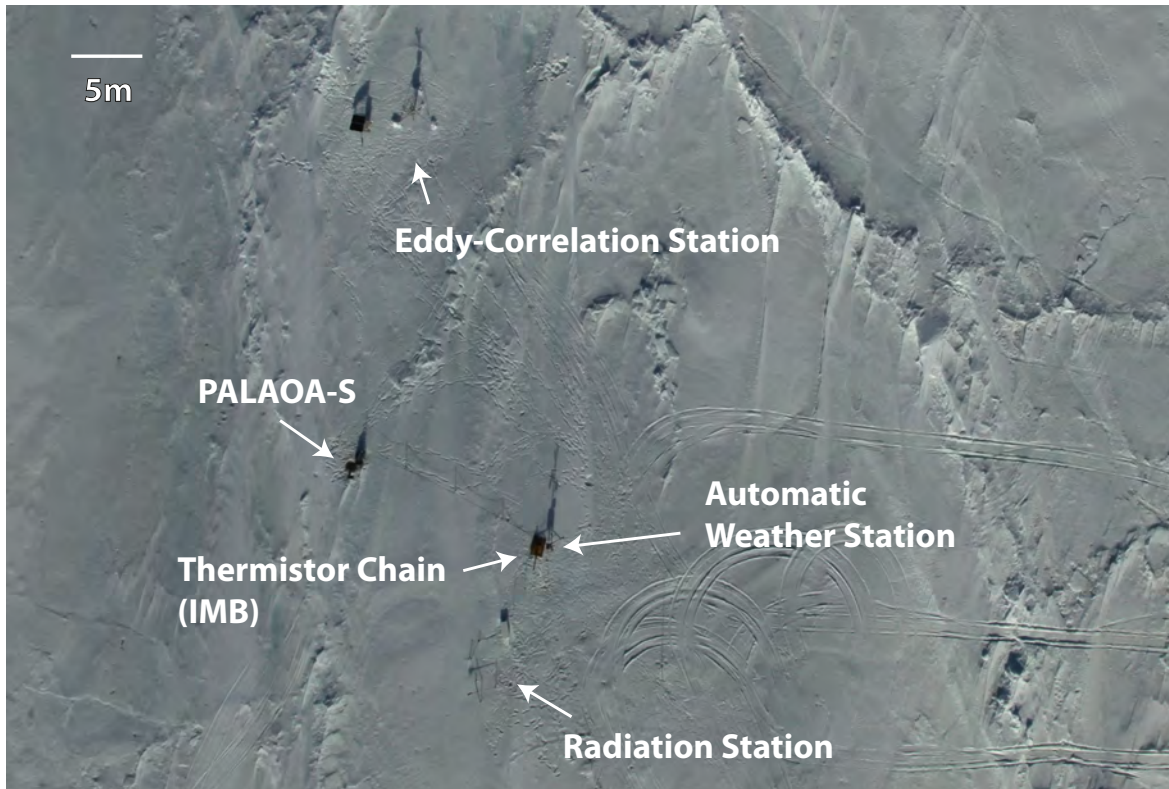


Figure 33: Aerial photo of instrument setup at ATKA03. Photo: AWI

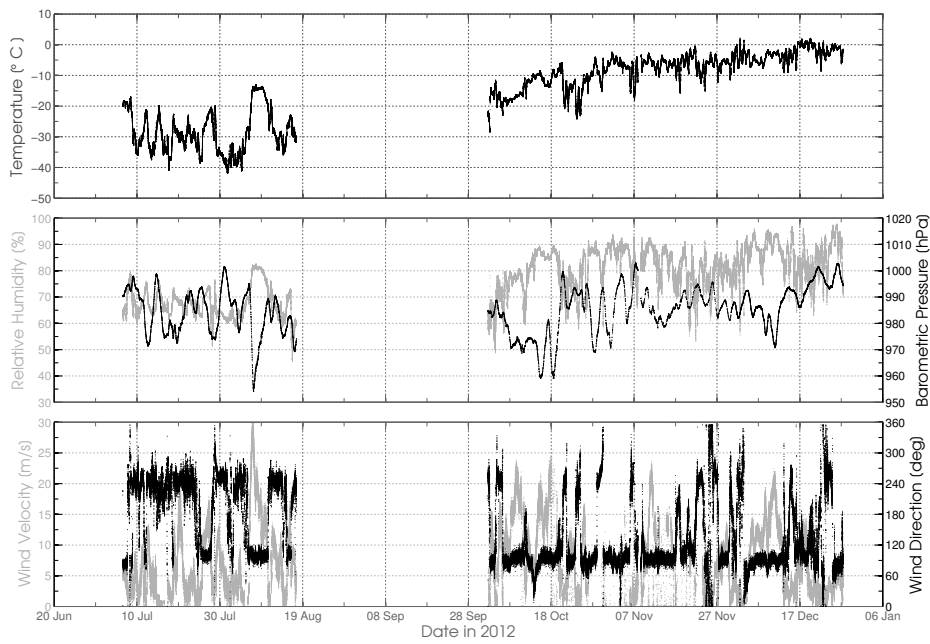


Figure 34: Atmospheric parameters

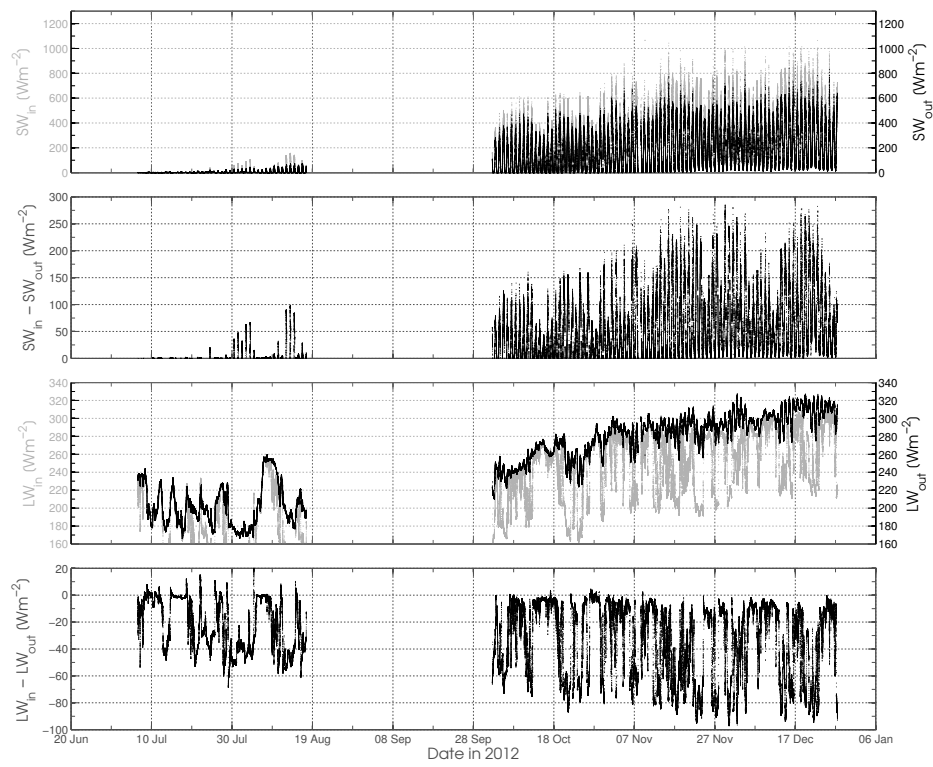


Figure 35: Radiation

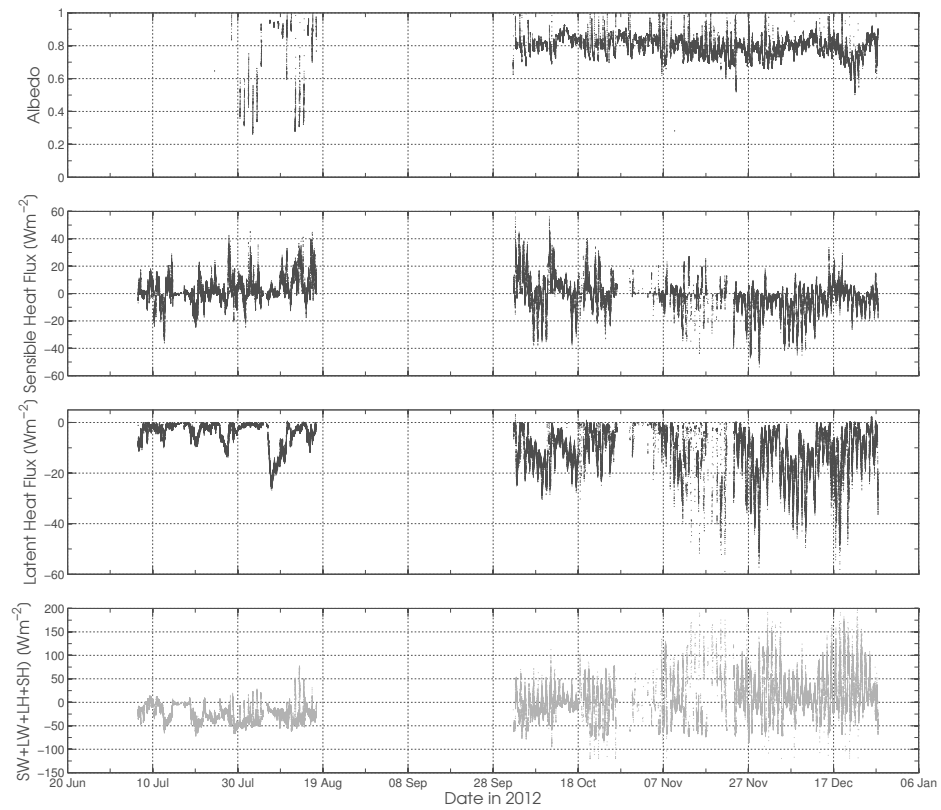


Figure 36: Albedo, Heat Fluxes and Net Radiation

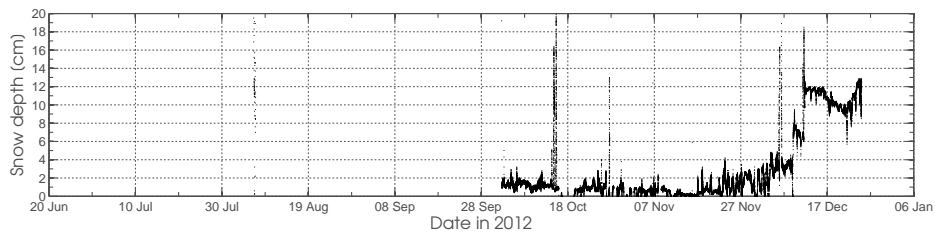


Figure 37: Snow depth (ultrasonic)

7.3. Comparison of AWS and BSRN data

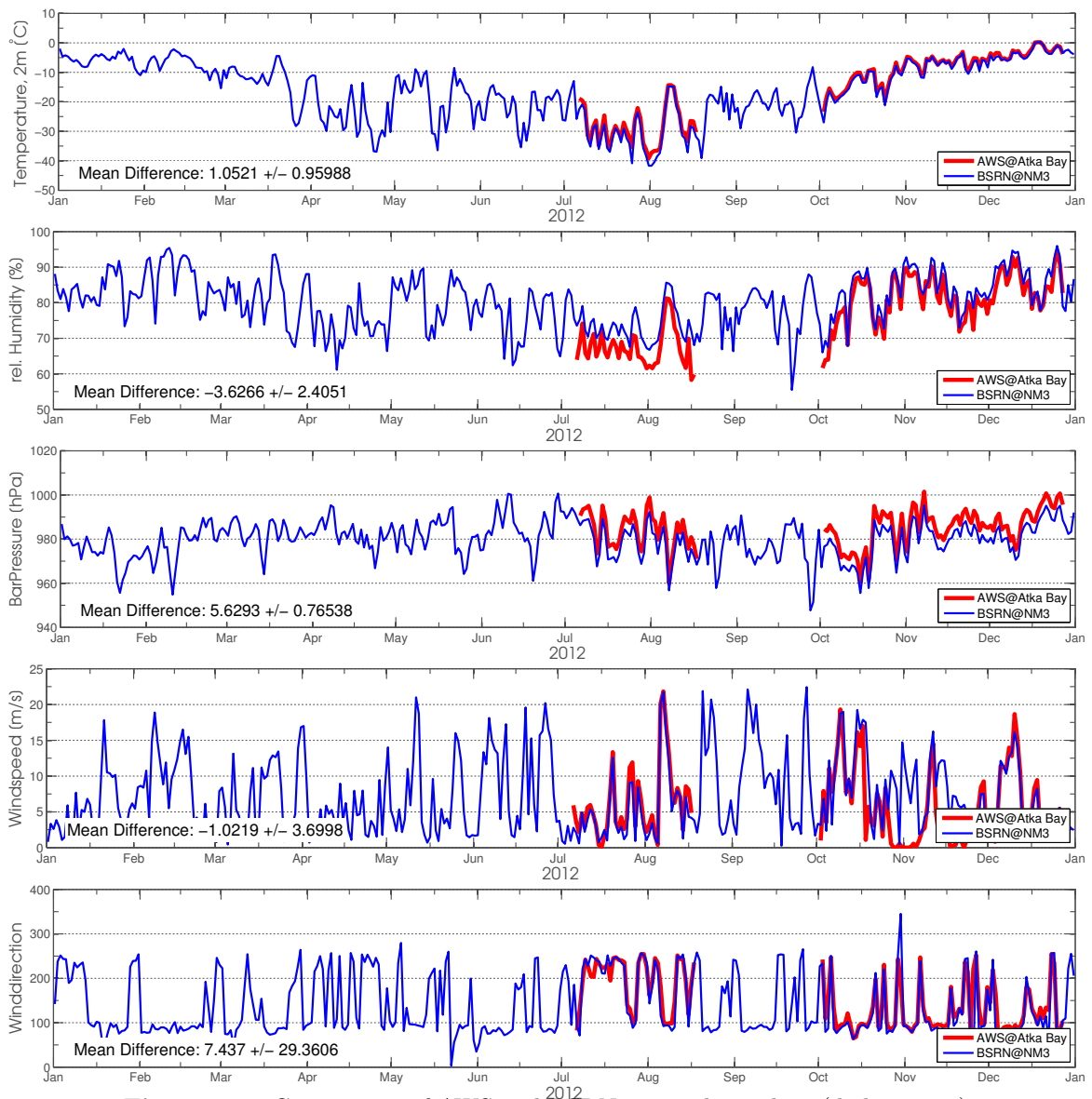


Figure 38: Comparison of AWS and BSRN atmospheric data (daily means)

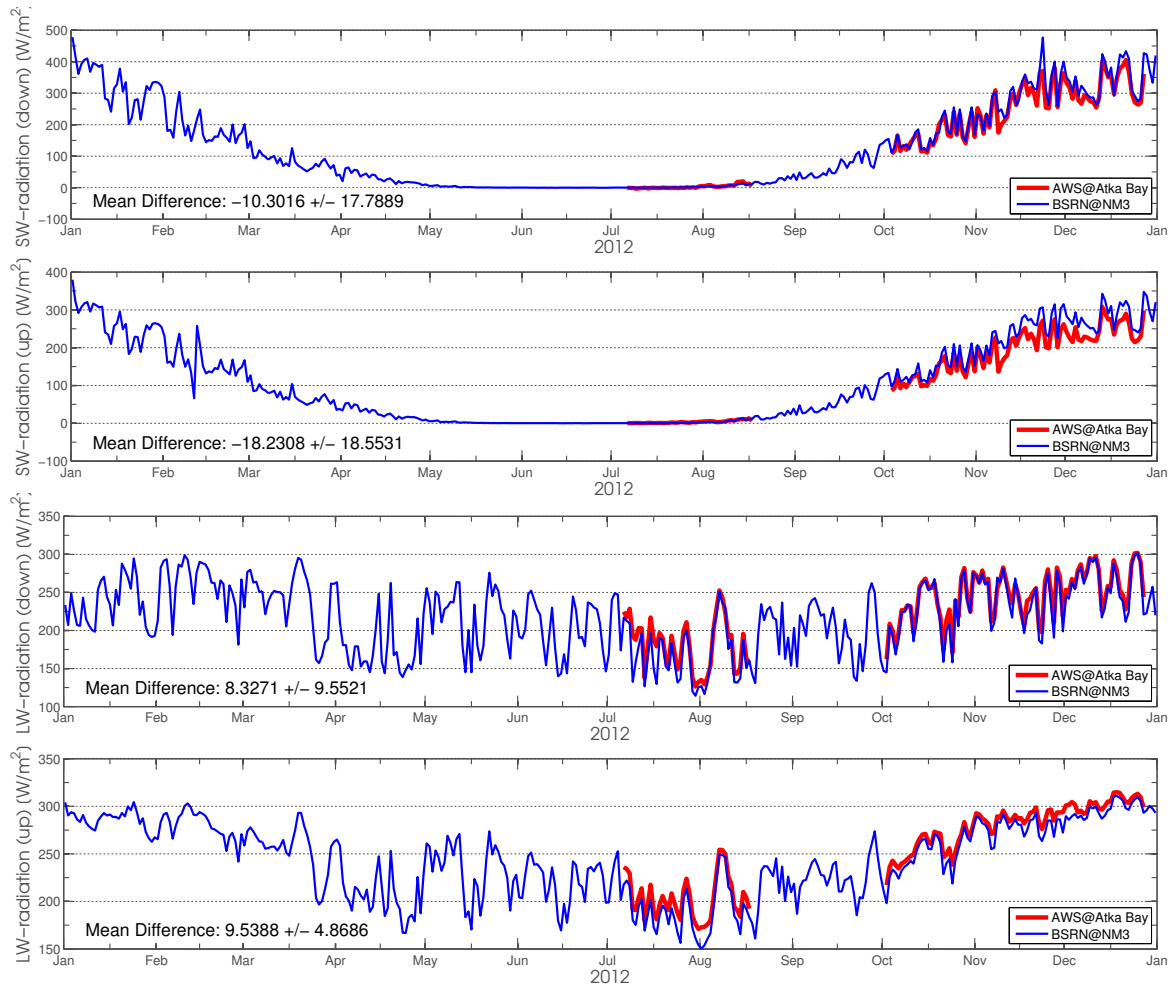


Figure 39: Comparison of AWS and BSRN radiation data (daily means)

7.4. Eddy Covariance and Turbulent Momentum Flux

On 21 November 2012, an Eddy Covariance and Turbulent Momentum Flux Station (ECS) to measure the turbulent heat fluxes of sensible and latent heat as well as the CO_2 flux was deployed at ATKA-03 (S 70°34.499', W 8°2.893'). This station was placed approx. 25 m northeast of the automatic weather station (Figure 40a). The ECS comprised of a CSAT3 sonic anemometer (see Figure 40b), an ultrasonic snow pinger (SR50A), a LiCor gas analyzer and a Campbell Scientific CR3000 data logger. The sonic anemometer was first mounted in eastward direction, 2.58 m above the ground and 0.71 m from the mast. The snow pinger was mounted on the mast at a height of 0.57 m, facing in west-southwestward direction. The power was supplied by three 100 Ah lead batteries, which were borrowed from the PALAOA project. These were constantly recharged by two solar panels at 90 Watt each, facing northwards.

On 22 and 23 November 2012, the EC-Station was completed with the LiCor gas analyzer, mounted parallel to the sonic at a height of 2.35 m above ground. Furthermore, the sonic anemometer was readjusted in south-eastward direction, 2.55 m above ground. The horizontal distance between the two sample volumes was 10 cm, the vertical distance 17 cm. Both volumes were between 66 and 67 cm from the mast. The EC-Station data in full setup are available from 23 November 2012, 11:15UTC until disassembly on 30 December 2012, 15:30 UTC.

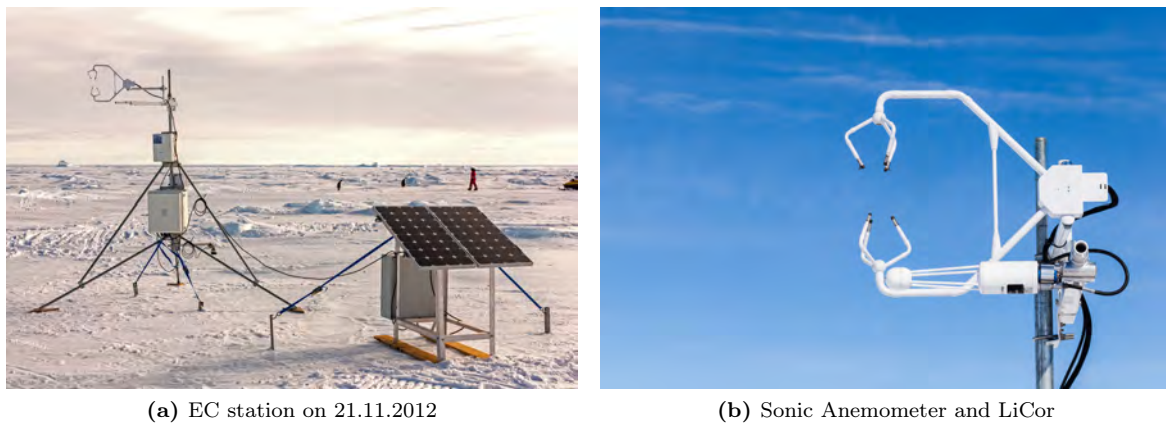


Figure 40: EC station set-up. Photos: Mario Hoppmann

A problem for the EC-Station as well as for the AWS, started with the rising temperature mid December. This resulted in additional melt around the feet of the mast and eventually a tilt of the mast. The sensors orientation had to be corrected as good as possible.

In Figure 41, the preliminary results of the processed EC data are shown. Presented are the turbulent fluxes of sensible and latent heat as well as the turbulent CO_2 flux. The processing of the data was done using the using the EC-Frame wrapper function by [Drüe \(2012\)](#) for the

ECPACK library by Dijk et al. (2004). 30 min intervals were chosen for averaging, resulting in a rejection of about 27% of the sensible heat flux data, 25% of the latent heat flux data and 31% of the CO₂ flux data due to bad test results.

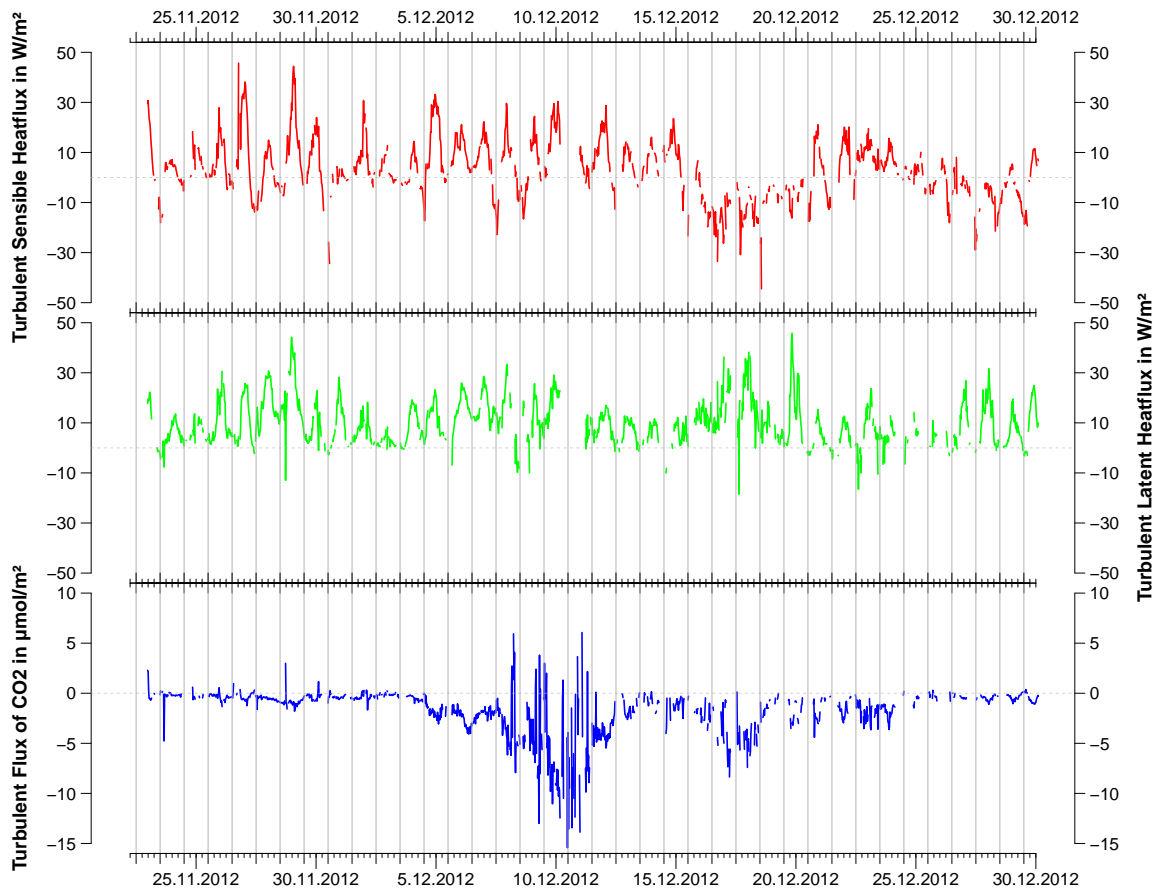


Figure 41: Post processed results showing the turbulent sensible heat flux (top), turbulent latent heat flux (mid) and the turbulent flux of CO₂ (bottom). Data gaps result either from maintenance of the station or exclusion due to a bad test flag. Fluxes are considered positive if directed towards the atmosphere.

The dominant wind direction during our campaign was ESE (100°) which made readjustment of the instrument obsolete. On average, the sensible and latent heat flux are positive during the sample period ($\sim 3 \text{ W/m}^2$ and $\sim 10 \text{ W/m}^2$ respectively) and the sea ice beneath our mast emerged as a CO₂ sink ($\sim -2 \text{ } \mu\text{mol/m}^2$). Fluctuations especially of the CO₂ flux are quite large (between $\sim -15 \text{ } \mu\text{mol/m}^2$ and $\sim +6 \text{ } \mu\text{mol/m}^2$) and correspond to storm events and/or high temperatures as presented in section 7.5. The influence of changing snow and sea ice properties during the onset of melt and rising temperatures still have to be investigated.

7.5. General Meteorological Observations during the SIMBIS campaign

The SIMBIS field campaign was carried out in the transition period from late austral winter to early austral summer, hence covering still cold non melting periods as well as melt onset and melt/freeze cycles. This section describes the general weather conditions during the field campaign from November 19th, 20012 to January 7th, 2013. All data shown here are courtesy of Gert König-Langlo. Events like new snow fall, drifting/blowing snow and hence relocation of snow masses as well as the melt/thaw onset and freeze/thaw cycles influence especially the snow pack. This again influences other surface measurements and their timing, e.g. the albedo transects were carried out in 8/8 cloud conditions.

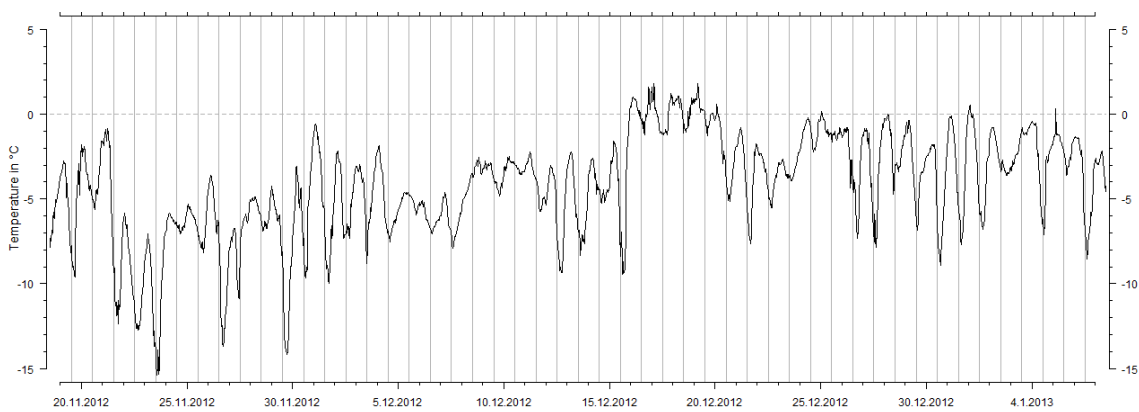


Figure 42: Timeseries of the 2 m Air temperature in $^{\circ}\text{C}$ during the field campaign measured at Neumayer III.

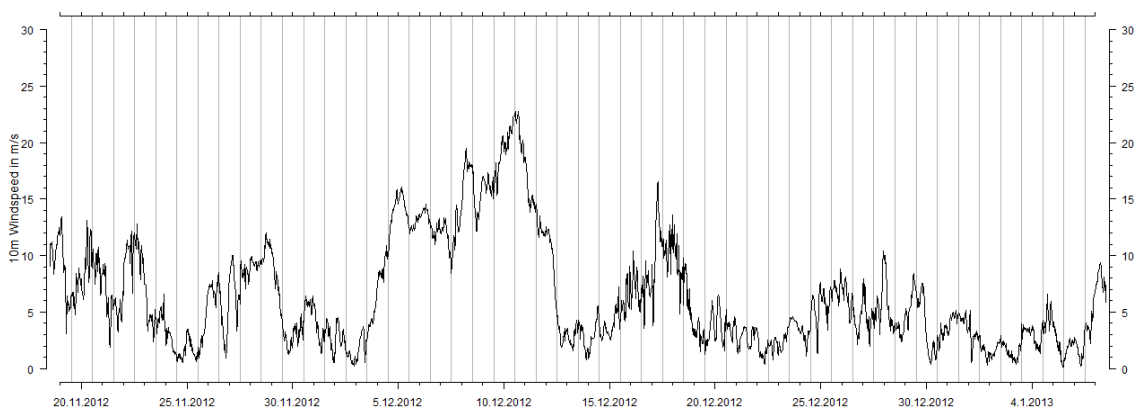


Figure 43: Timeseries of the 10 m windspeed in m/s during the field campaign measured at Neumayer III.

The here presented meteorological data were compiled from the meteorological weather station data as well as manual observations at Neumayer III. All shown data are 30 min averages.

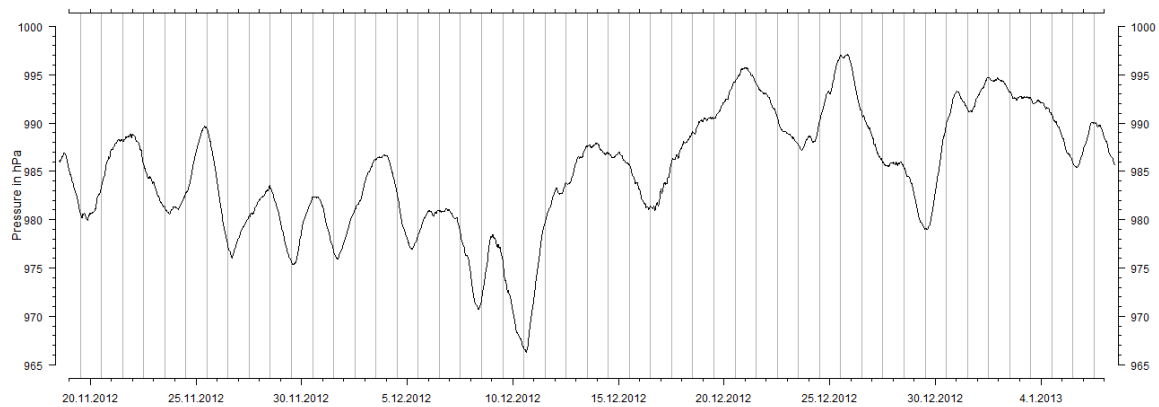


Figure 44: Timeseries of the surface pressure in hPa during the field campaign measured at Neumayer III.

From Figure 42, showing the 2 m air temperature time series during the field campaign, it is possible to derive three different states. First, from November 19th, 2012 to December 15th, 2012, the 2 m air temperature is always below zero degrees. In the second period between from December 16th, 2012 to December 20th, 2012, the 2 m air temperature reaches temperatures of up to two degrees centigrade during noon and afternoon with relatively small daily amplitude, starting off the melt period. From December 21st, 2012 onwards until the end of the field campaign, the temperature ranges from zero degrees centigrade to minus nine degrees centigrade. During this state, the zero degree mark was reached on a regular basis, but with a higher daily temperature amplitude than in the previous state. This results in freeze/thaw cycles, highly influencing and changing the snowpack.

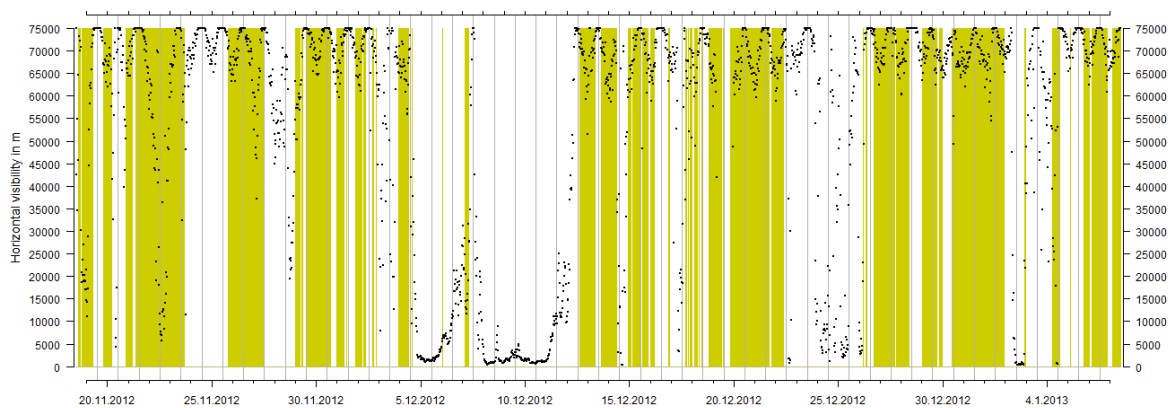


Figure 45: Timeseries of the horizontal visibility in m during the field campaign measured at Neumayer III. Yellow bars indicate whether the sensor could see the sun or not.

Figures 43 and 44 present the 10 m windspeeds in m/s as well as the surface pressure in hPa . From November 19th, 2012 to December 20th, 2012, recurring events of relatively high windspeeds exceeding $10 m/s$ and $15 m/s$ alternate with relatively low windspeeds of below

5 m/s . An eight day long storm period from December 5th to December 12th stands out from this. The highest windspeeds coincide with a low pressure system passing by (see Fig. 44). The period after the 21st of December is characterised by in general lower windspeeds, not exceeding 10 m/s .

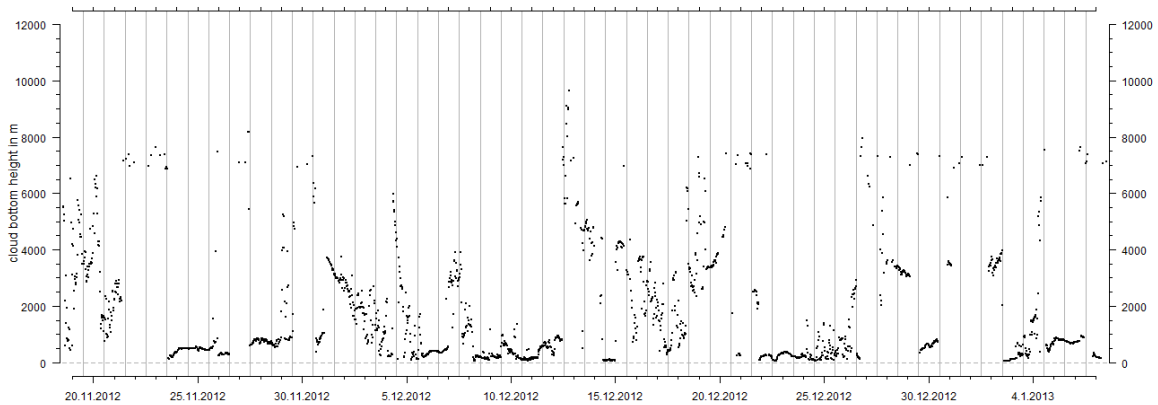


Figure 46: Timeseries of the cloud bottom height in m during the field campaign measured at Neumayer III. Gaps in the data indicate "no clouds".

Finally, Figure 45 presents the horizontal visibility as an indicator of snow drift. In addition, the yellow vertical bars indicate the presence of the sun to the sensor. Events of low visibility correspond well to the events of high windspeeds, especially during the storm event (see Fig. 43). However, two events of low visibility, one around christmas and one on January 2nd, 2013 show no conformance to the windspeed data. But these events of low visibility correspond well with the cloud bottom measurements as shown in Figure 46. Very low cloud bottom height would point towards either very low clouds or fog. Manual observations state new snow fall at November 19th/22nd/23rd/29th, 2012 as well as during the storm period.

8. Spectral Radiation

Beginning in August 2012, several TriOS hyperspectral radiometer for the UV and VIS spectral range (320 - 950nm) were used to determine irradiances above, inside and below sea ice and snow. All sensors used were of the same type (RAMSES ACC VIS by TriOS optical sensors, see Figure 47 and Table 7), the exception being the inclination/pressure modules integrated in some of them.



Figure 47: RAMSES-ACC-VIS - Hyperspectral UV-VIS Irradiance Sensor. Photo: TriOS

The general setup of these sensors included a reference sensor for incoming irradiance and one for reflected irradiance by the sea ice/snow surface. Spectra were recorded simultaneously, so that spectral albedo could be calculated by normalizing reflected by incoming irradiance. In addition, most measurements included a sensor for irradiance transmitted through sea ice and snow. The different instrument setups are described below.

8.1. Sensor calibration

Inevitable inaccuracies during the production of RAMSES radiometers cause differences in measured absolute irradiances among different sensors. To be able to compare data acquired by different sensors during a field campaign, a calibration of all instruments is required. Therefore, we operated all 7 sensors on the roof of Neumayer III, next to the balloon hall, during three calibration setups (Figure 48).

Due to limitations in instrumentation and cables, we were only able to operate three sensors at a time, but used three different combinations during each setup. We compared all measured irradiances and chose one sensor in the middle of the range as a reference. For all

Table 7: RAMSES ACC VIS specifications (www.trios.de)

wavelength range	320 - 950 nm
detector type	256 channel silicon photodiode array
spectral sampling	3,3 nm/pixel
spectral accuracy	0,3 nm
usable channels	190
typical saturation (4 ms)	10 W m ⁻² nm ⁻¹ (at 400 nm) 8 W m ⁻² nm ⁻¹ (at 500nm) 14 W m ⁻² nm ⁻¹ (at 700nm)
collector type	cosine response
accuracy	better than 6-10 % (depending on spectral range)
integration time	4 ms - 8 sec
data rate (RS232)	1,200 - 19,200 baud
power requirements	1,5 - 11 VDC 0,85 mW (data acquisition active) 100 mW (interface active) 0,5 mW (stand-by modus)
size	Ø 4,83 cm x 26 cm (without connector)
weight in air	<1,0 kg (stainless steel / POM housing)
depth range	300 m
operating temperature	-10°C to +50°C



(a) View from balloon hall



(b) Close-up of sensor setup

Figure 48: Exemplary calibration setup of three spectral radiometers on the roof of Neumayer III. This procedure was necessary to compensate sensor-specific differences in measured irradiances. Photos: Mario Hoppmann

other sensors, a broadband scaling factor was derived and implemented during the processing of all data shown in this report (Table 8)

Table 8: TriOS spectral radiometer used during field work at Atka Bay, dates of parallel measurements on the roof and resulting scaling factor.

Used at	SAMIP	SAM	scal. Fac.	Calibration on			
				07.12.2012	09.12.2012	03.01.2012	06.01.2013
RS Aug	506A	8325					
	5071	8383					
	5072	8382					
		8387					
RS Oct		8324	1.1189			x	
	506B	8343	1.0303			x	x
	5063	8328	1.0000			x	x
SIMBIS	5058	82c3	0.9842	x	x		x
	505A	82c0	0.9209	x			
		82CE	1.1251	x	x		
	5067	8330			x		

8.2. Data processing

Generally, all spectra (raw as well as calibrated data) recorded by MSDA_XE were stored in a central database. For further processing, only the raw data were exported from the database, whereas all spectra of one dataset were stored together in a single file in TriOS format (*.dat*). These separate files were then loaded into a Matlab function where sensor-specific calibration files were applied and the aforementioned scaling factors were included. In detail, the following procedure was applied to all *.dat* files:

1. Copy the scripts *dat2spec_ip.awk* and *dos2unix2spec.script* to folder with the *.dat* file.
2. Use Linux or Cygwin: Navigate to folder with *.dat* files and run *dos2unix2spec.script* to reshape the data.
3. Matlab: edit *dataload_NM* for sensor IDs and path to TriOS calibration files (*.ini*).
4. Run Matlab function *dataload_NM* for calibration and formatting of data;

The final data were saved into a Matlab variable for further processing, plotting etc. We did not apply any complex corrections due to shadowing of the sensors etc, but we tried to minimize these effects during deployment.

8.3. First Radiation station 10 - 17 August 2012

On 10 August 2012, we deployed a radiation station at the AWS site, consisting of four spectral radiometers and a styrofoam box, containing a control unit (TriBox II, Extensionbox), and two lead batteries to power the units (Figure 49). These instruments are referred to as RS1 in this report. Two of the radiometers (SAMIP5072 looking up- and SAM8387 looking

downward) were mounted on a custom-made rack, which was installed on the sea ice such that shadowing of the sensors by the frame was minimized. We took great care during deployment not to disturb the snow surface to avoid artifacts in the measurements. In order to investigate the light transmission through snow, we installed another radiometer just below the snow/sea ice interface.

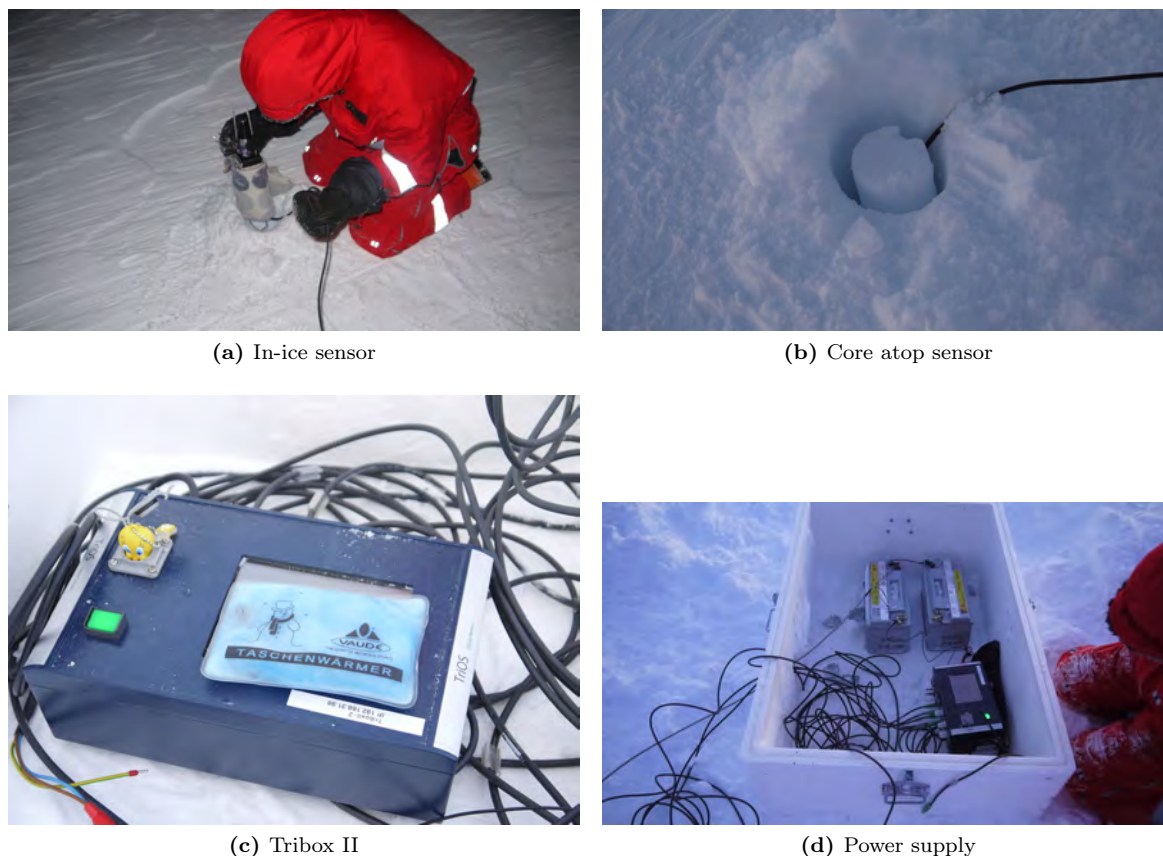


Figure 49: Deployment of first radiation station. Photos: Thomas Schmidt, Meike Kühnel

To leave the area around the sensor as undisturbed as possible, we drilled a 9 cm core hole through the snow and the top part of the sea ice. SAMIP5071 was recessed in the hole such that its top part was in one line with the snow/sea ice interface. It was carefully covered with snow after installation. Initial snow depth on top of this sensor was 90 cm.

Our fourth sensor was originally intended to be installed in the water column just below the sea ice to measure the light transmission through the entire snow- and sea-ice cover. But to avoid the freezing of ice platelets on the sensor and the risk of not being able to recover it, we decided to place the radiometer directly in the solid sea ice. We again drilled through snow and sea ice and recessed SAMIP506A in the hole. We placed a part of the sea-ice core (53 cm) back in the hole on top of the sensor, and covered the remaining hole with 94 cm of snow. A scheme of the instrument setup of RS1 is presented in Figure 50. The spectra of all four sensors were visible on the screen of the Control Unit (Tribox II) after installation. The

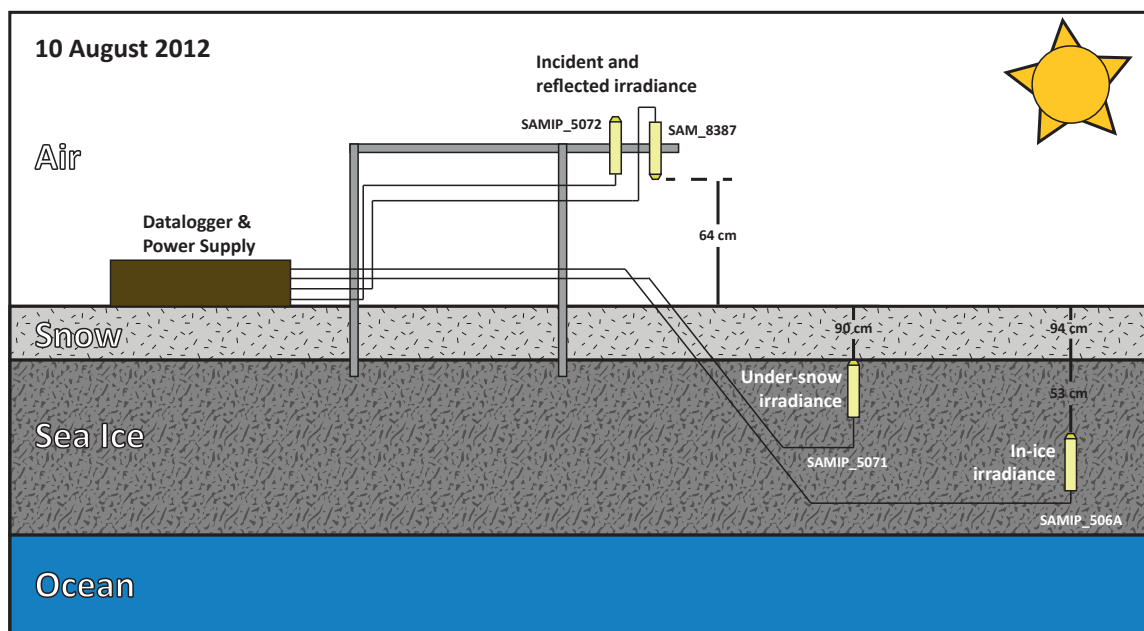


Figure 50: Scheme of radiation station as set up on 10 August 2012

measurement interval was set to 10 minutes.

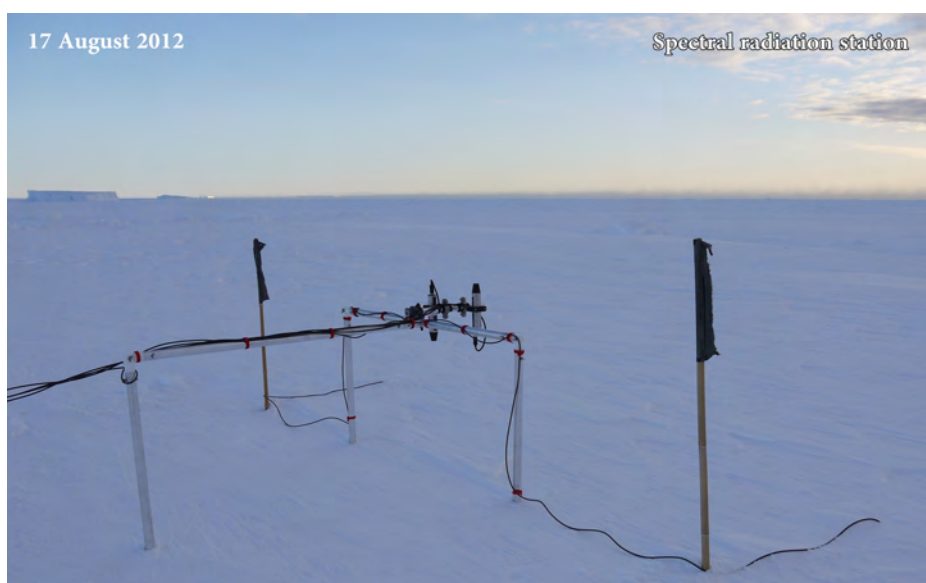


Figure 51: First radiation station on 17 August 2012. Photo: Thomas Schmidt

On 17 August 2013, after one week of operation, RS1 was visited again (Figure 51) to check the instruments and to copy the data. This was also the last time we saw RS1, because a heavy storm should break off a part of the sea ice a few days later (section 10)

8.4. Second Radiation station October 2012 - January 2013

A second radiation station was set up at ATKA03 on 2 October 2012. This time, two RAMSES ACC VIS radiometer were mounted on a rack for incoming and reflected irradiance, while a third sensor was frozen into the sea ice at a depth of 70 cm (Figure 52). Due to the lack of snow at the sampling site, our original plan of placing this third irradiance sensor directly below the snow cover could not be realized.

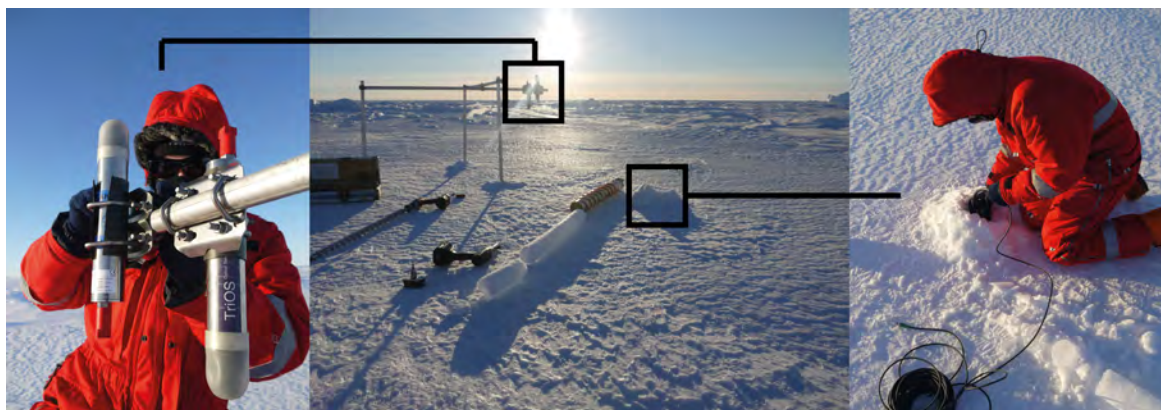


Figure 52: Left: two spectral radiometers were set up to measure incoming shortwave radiation (upward-looking sensor) and reflected shortwave radiation from the surface (downward-looking sensor) to calculate albedo of sea ice and snow. Middle: Setup of radiation station. Right: a third radiometer is lowered through a corehole (9 cm diameter) to measure light transmission through sea ice and snow. Photos: Thomas Schmidt, Meike Kühnel

A scheme of the second radiation station is shown in Figure 53.

The site was visited several times afterwards, especially during the SIMBIS field campaign we checked the station nearly every three days. From mid December on, the rack started to melt into the sea ice, which made several adjustments necessary to level the sensors correctly.

Unfortunately, the power supply of two lead batteries was not enough to ensure a continuous operation for more than a few days. There are several gaps in the data, where the batteries could not be changed for several days mostly because of long bad-weather periods. At the time of writing, a new concept for power supply is worked on, where the radiometers are controlled by a Campbell Scientific data logger. The first promising tests showed that this setup is much more energy-efficient, and will replace our current setup as soon as possible. In addition, the sensor for incoming irradiance was not very reliable, being unable to record at least 10% of its spectra.

The station was dismantled a few days before the end of the SIMBIS campaign, on 30 December 2012. We had great problems recovering the in-ice sensor, but finally, after 2,5 hours of drilling and sawing, we managed to get the radiometer out of the sea ice (Figure 54).

Figures 55 a-c show the spectra of incoming, reflected and transmitted irradiance at highest sun elevation, respectively. Figures 55 d and e show the calculated albedo and transmittance.

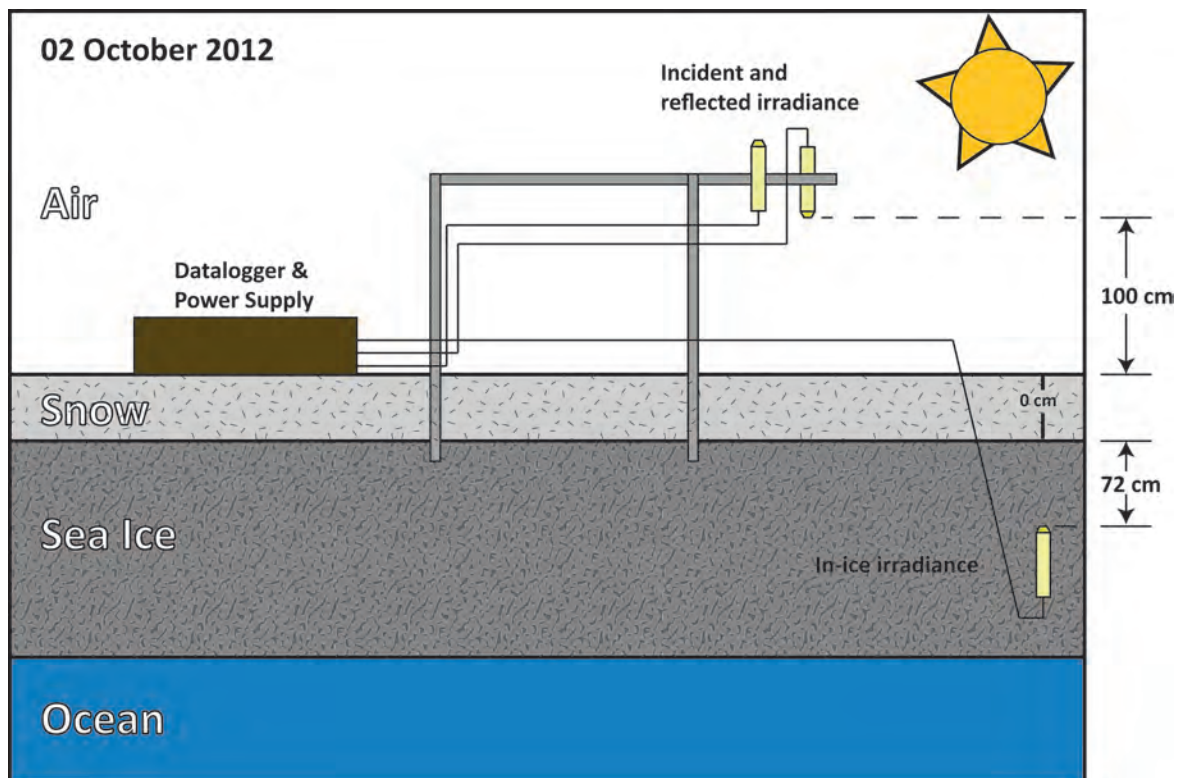


Figure 53: Scheme of radiation station sensor set-up

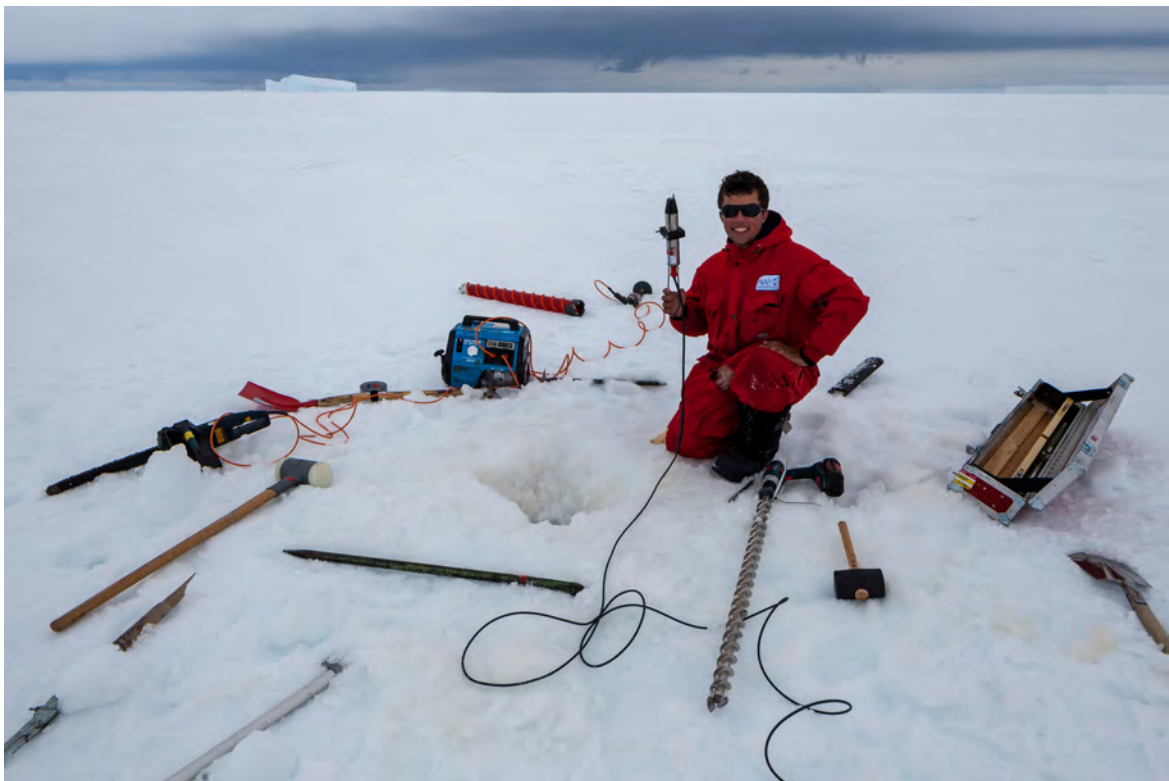


Figure 54: Recovery of RAMSES sensor frozen in the sea ice. Photo: Mario Hoppmann

The white areas are data gaps mainly caused by power failure.

8.5. Surface Albedo Spot Measurements

During the SIMBIS campaign, spot measurements of spectral albedo were carried out on several occasions, mostly in conjunction with snow pits and L-Arm measurements. The data still needs to be compiled and is not shown here.

8.6. Surface Albedo Transects

To obtain a large-scale dataset of surface albedo at Atka Bay, we mounted two RAMSES spectral radiometer on a snowmobile. We modified the metal poles and sensor holders from our two L-Arms to mount one upward-looking RAMSES on the back and one downward-looking sensor to the side of the vehicle.

The two RAMSES were operated on an IPS Box connected to a *Panasonic Toughbook*, which were transported in a small Zarges Box. Power was supplied by a small Honda generator. Simultaneous spectra of the two sensors were recorded with the software MSDAXE by *TriOS* at a measurement interval of 5 seconds (external trigger, set to timer). The raw as well as the calibrated spectra were stored in a database. The position data were recorded in parallel by a handheld GPS in 1 s intervals. Laptop and GPS times were synchronized beforehand.

In total, more than 200 km of albedo data were obtained on four days, distributed over a time period of 39 days.

The major downsides with respect to data quality of this method were twofold:

1. On uneven surfaces (snowdrifts/sastrugi/deformed ice), the sensors departed from their ideal vertical orientation.
2. The shadow cast on the surface by the snowmobile was sometimes below the downward-looking sensor.

Other problems we encountered were the following:

1. The downward-looking sensor was mounted approximately 1 m from the vehicle, and 50 cm above the ground. As a consequence, even small obstacles could potentially lead to this sensor touching the ground.
2. In the past, we experienced mixed reliability of the TriOS instruments. It was not unusual that the spectra were not recorded due to some mysterious instrument failures.

We counteracted these potential error sources by

1. choosing overcast days with diffuse light conditions.
2. driving carefully at constant speed, with a maximum of 15 km/h on flat surfaces. The vast majority of our tracks had even surface, depending on the location and the weather of the last days.

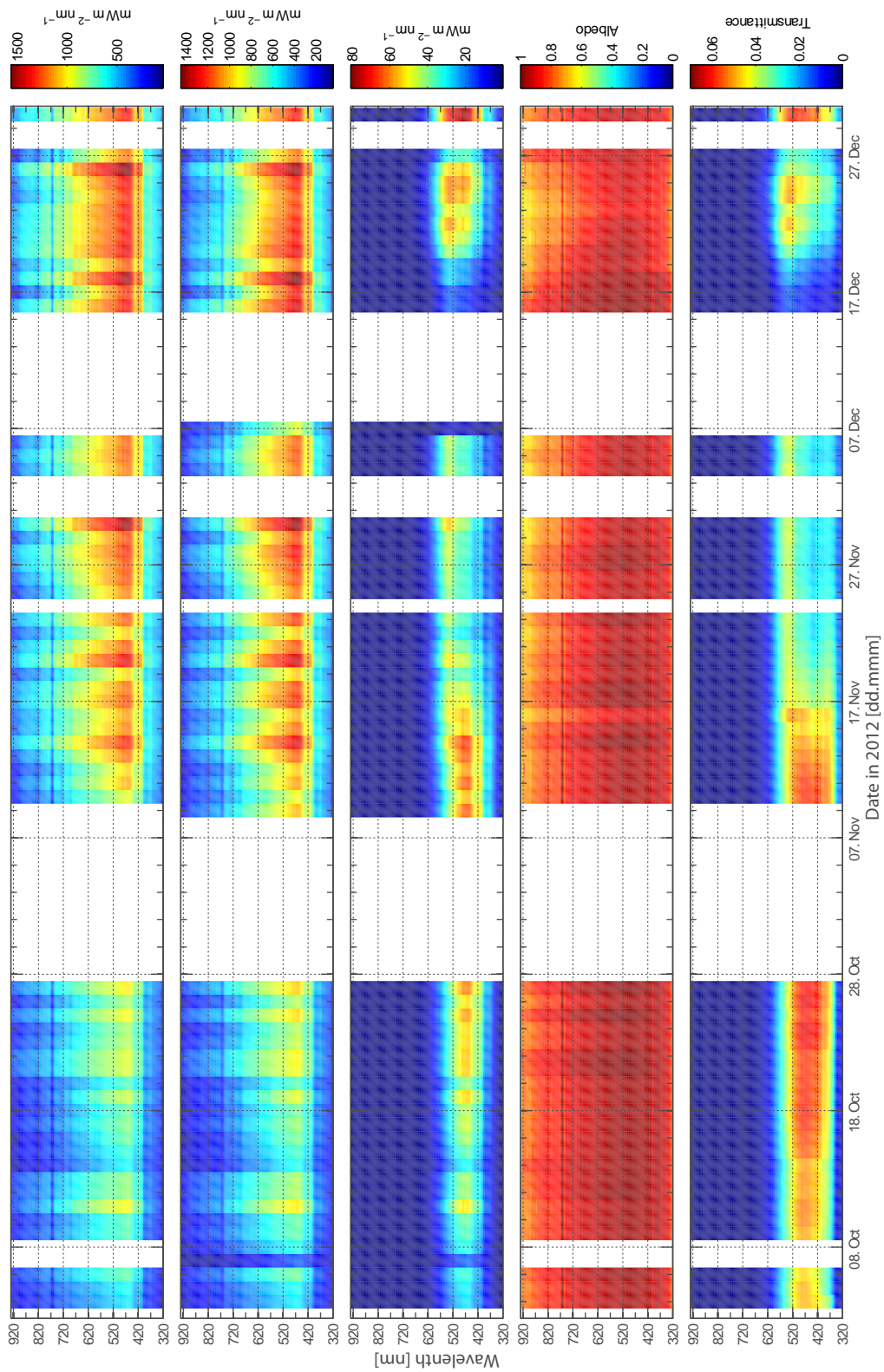


Figure 55: Results of continuous irradiance measurements at ATKA03 between October 2012 and January 2013. Incoming (a), reflected (b), transmitted irradiance (c), Albedo (d) and Transmittance (e) at highest sun elevation. The white areas are data gaps mainly caused by power failure.



Figure 56: Two RAMSES sensors mounted on “Albedo skidoo”. The Zarges Box with the laptop and the generator are located on the back of the snowmobile. Photo: Mario Hoppmann

3. mounting the downward-looking sensor to the side where no/least shadow was visible on the ground. In clear sky conditions we always had the sun directly behind us. During diffuse light conditions, which prevailed most of the time, only a very soft shadow was cast to all sides, barely visible by eye.
4. checking the data recording at regular intervals, to minimize the risk of instrument failure. It turned out that the sensors were very reliable, with only few data losses.
5. checking sensor orientation regularly. The deviation from the ideal vertical orientation was minimal in the case of the upward-looking sensor, but rather strong in the case of the downward-looking sensor due to the long side cantilever. This potential error source was at least partly compensated by the fact that the sensor head was only about 50 cm above the target surface. Further analyses are required to estimate the consequences for data quality, for example by looking at the inclination values of the sensor.

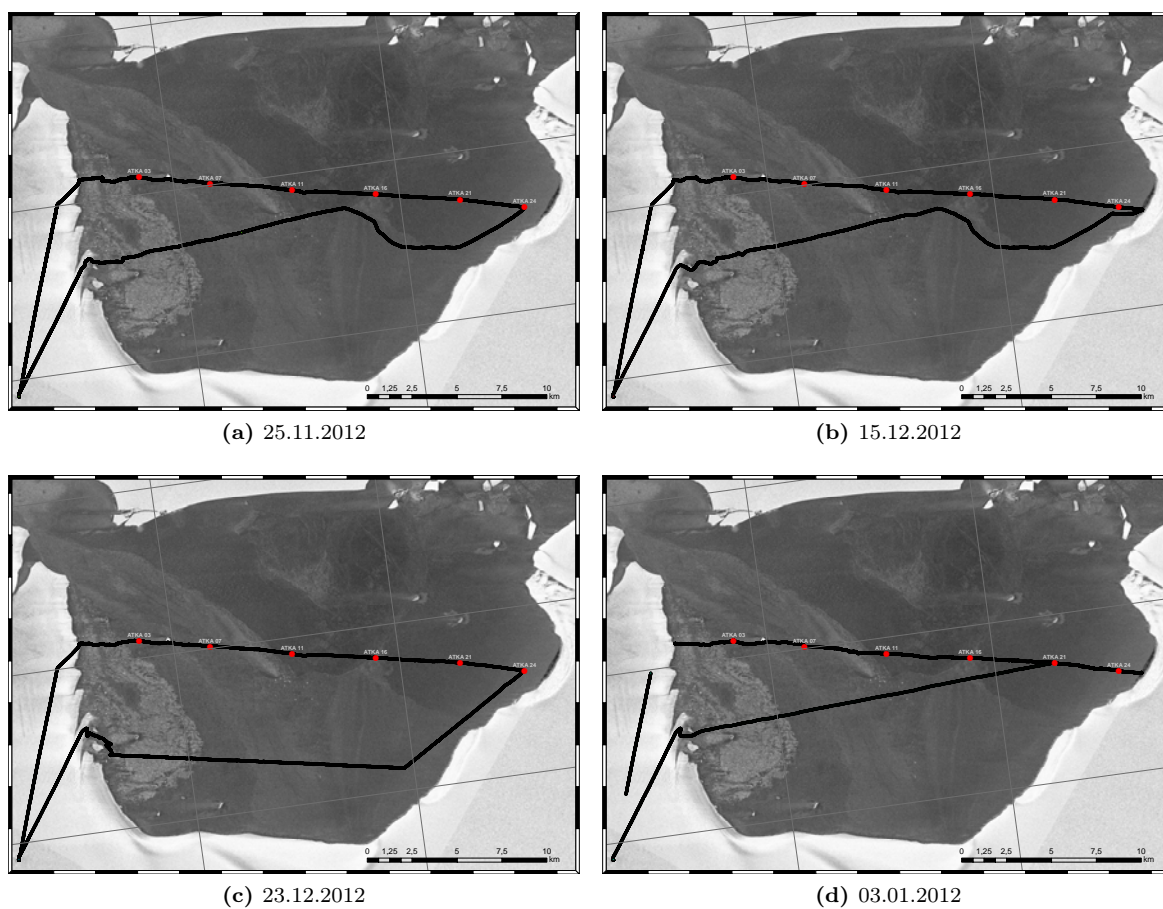


Figure 57: GPS tracks of albedo measurements

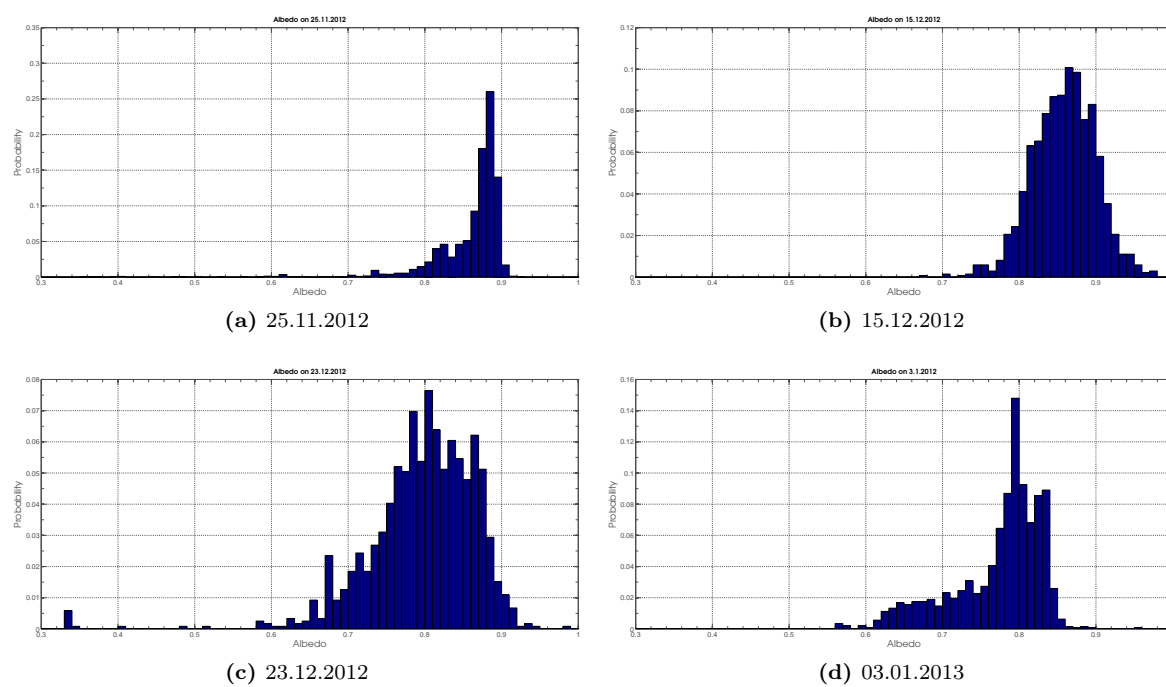


Figure 58: Probability Density of Albedo during transects

8.7. Light Transmission through Sea Ice and Snow

Another object of our campaign was the study of under-ice light regimes at Atka Bay. We intended to achieve this aim by lowering an an upward-looking spectral radiometer, mounted on a custom-made L-Arm, through a 10 cm diameter borehole. We successfully used this method several times in the Arctic, but the limiting factor at Atka Bay was, once again, the dense platelet layer below the solid sea ice. As a consequence, we had to choose sampling sites where the penetration of this layer was possible without damaging the instrument. At the same time, the sites had to be representative for Antarctic landfast sea ice in general. In the end we chose two sites with different sea-ice conditions: ATKA11 as a site with relatively new sea ice of thickness around 70 cm and a platelet-layer thickness of about 100 cm; and ATKA21 with a sea-ice thickness around 200 cm and a platelet layer of around 300 cm thickness. ATKA 11 was visited three times, while we visited ATKA21 twice (Table 9) Both sites had a variable snow cover. Measured sea-ice parameters at the sites of L-Arm measurements are given in Table 9, along with an indication if a sea-ice core for Chl-a filtration was drilled.

Table 9: Overview of sea-ice parameters during L-Arm measurements

Station	Date	z_sea ice	z_snow	FB	z_platelet	weather	Chl-a
ATKA11	23.11.2012	74	10	-5	135	...	
	30.11.2012	74	22	5	165	sunny 1/8	x
	29.12.2012	86	6	-20	100	...	x (27.12.2012)
ATKA21	01.12.2012	211	19		Stephan?	...	x
	28.12.2012	180	40	10	300	...	

The instrument setup comprised a total of three RAMSES sensors, one upward-looking reference sensor, one downward-looking albedo sensor, and the aforementioned transmittance sensor mounted on the L-Arm (Figure 59). The radiometers were operated on an IPS Box, and simultaneous spectra were manually recorded by the software MSDA_XE installed on a Panasonic Toughbook.

The 6 m long L-Arm was lowered as far as possible through the borehole, while it was not always easy to penetrate the dense platelet layer. Then we tried to lift up the bottom-most segment of the L-Arm by pulling the attached string. Most of the time several attempts were needed to succeed, because the platelets were blocking the upward movement. We took some practice to “feel” if the sensor was successfully lifted by gently pulling the string, and used the (unreliable) pressure values of the sensor to check if the sensor was oriented the right way. At ATKA11, the under-ice camera was a very good tool to observe the behavior of the L-Arm in the platelet layer. At ATKA21, the platelet-layer thickness was too large for the L-Arm to reach the underside, so the camera was of no use. In addition, we constantly checked the (rather imprecise) pressure values of the IP module of the under-ice RAMSES to ensure the

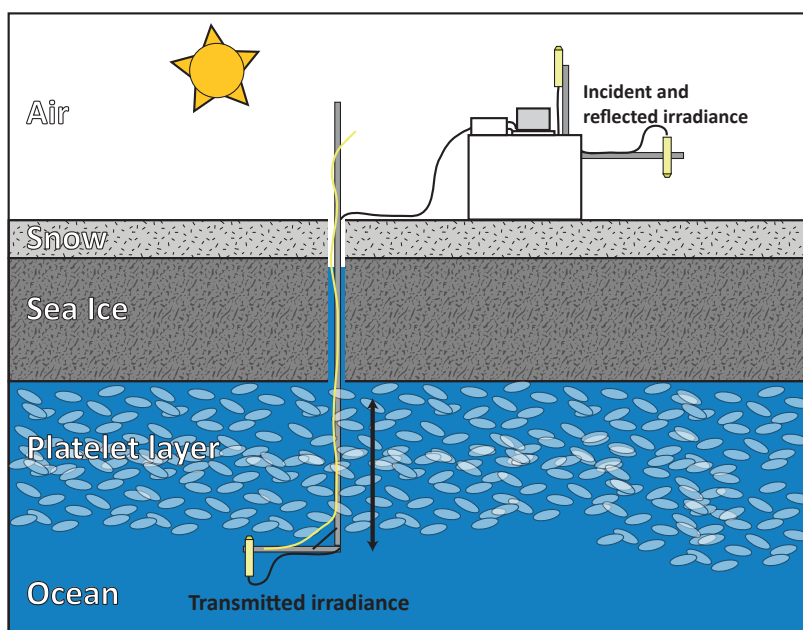


Figure 59: Instrument setup of under-ice irradiance measurements

L-Arm operated correctly.

Once the L-Arm was set up, we varied the depth of the sensor in a range limited by the sea-ice underside on the one hand and the length of the arm on the other.

By doing this, we obtained five transmittance datasets shown on the left in Figures 60 and 61. All spectra are normalized to incoming irradiance measured simultaneously by a reference sensor at the surface.

To investigate the influence of the snow cover on the under-ice light regime at our sampling sites, we removed the snow as careful as possible in a circle about 4 m in diameter directly above the sensor. The results are shown on the right in Figures 60 and 61

By normalizing the transmittance measurements with snow to the transmittance measurements without snow, we obtain the influence of the snow alone on under-ice light regimes. The results are given in Figure 62.

The simultaneous Albedo measurements still need to be processed, hence they are not shown here.

Further data analysis will for example comprise the determination of extinction coefficients and the optical properties of the platelet layer

L-Arm 24h

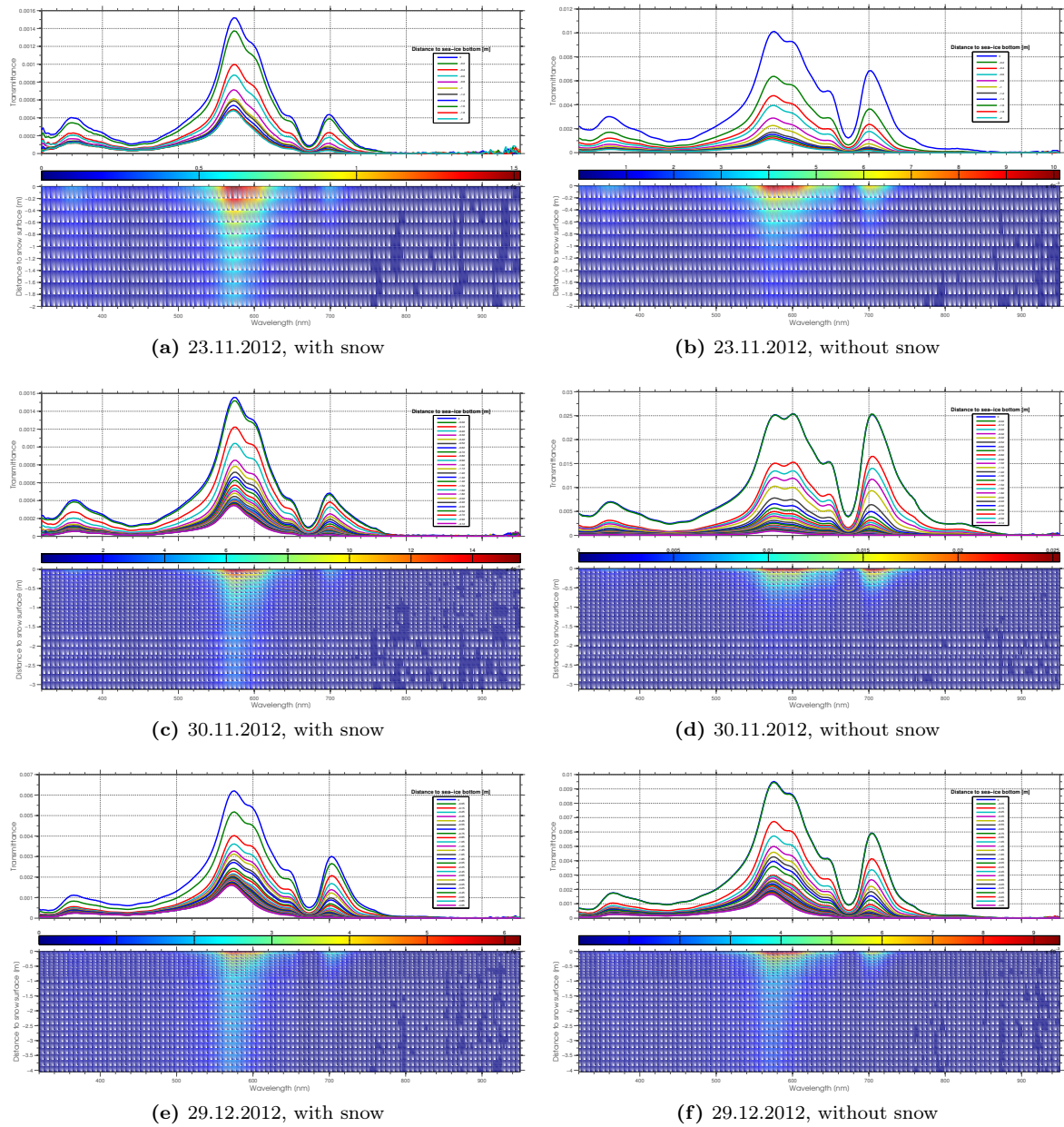


Figure 60: L-Arm measurements at ATKA11

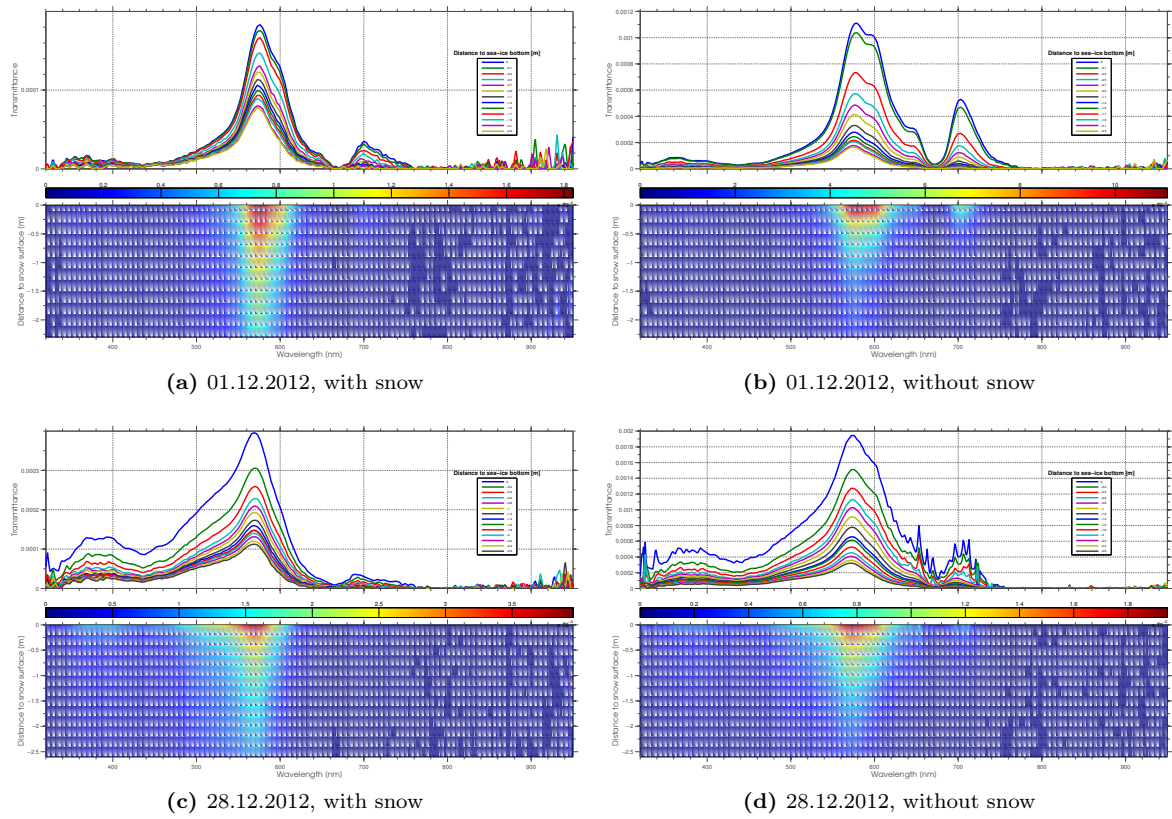


Figure 61: L-Arm measurements at ATKA21

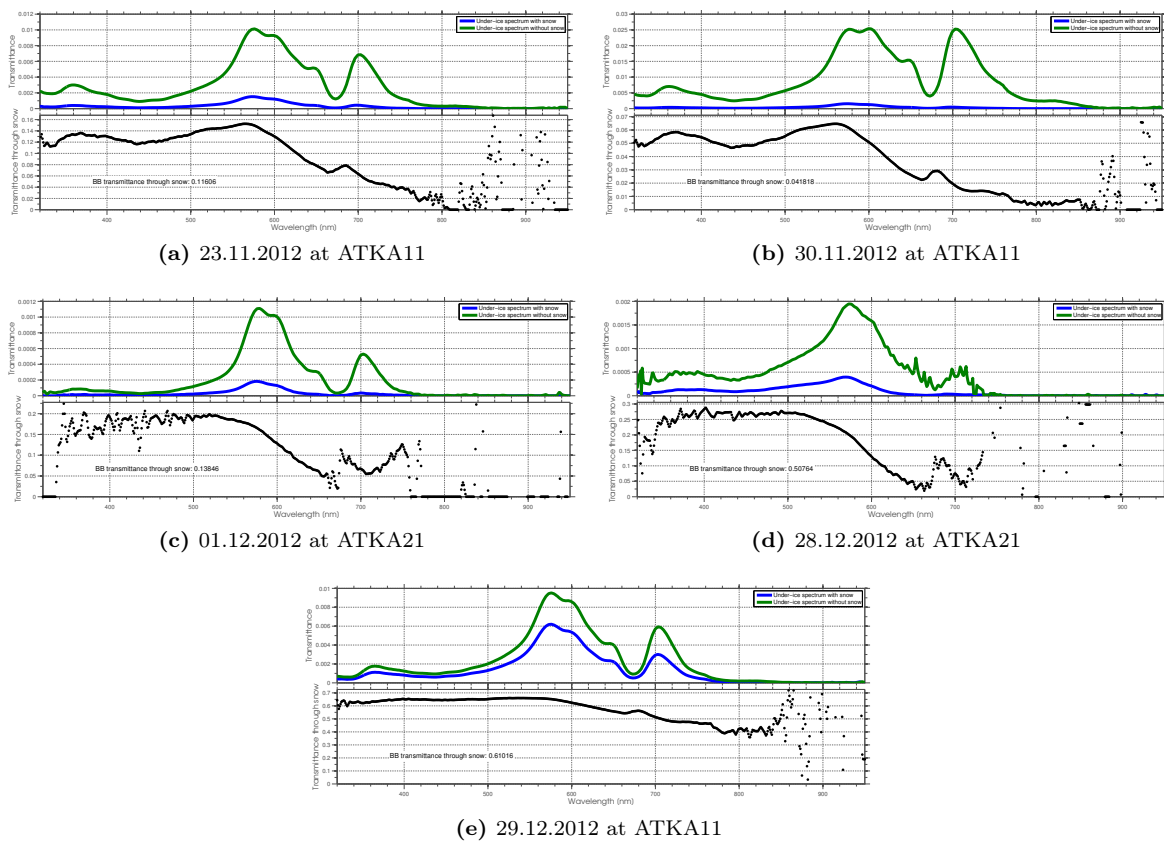


Figure 62: Spectral light transmittance measured directly at sea-ice bottom. Top: the blue line represents the spectrum measured under sea ice with undisturbed snow cover, the green line represents the spectrum measured under sea ice with the snow cover removed in a circle of $r=1.5$ m above the sensor. Bottom: Spectral light transmittance through snow (blue divided by green). The broadband light transmittance through snow is given in the text box.

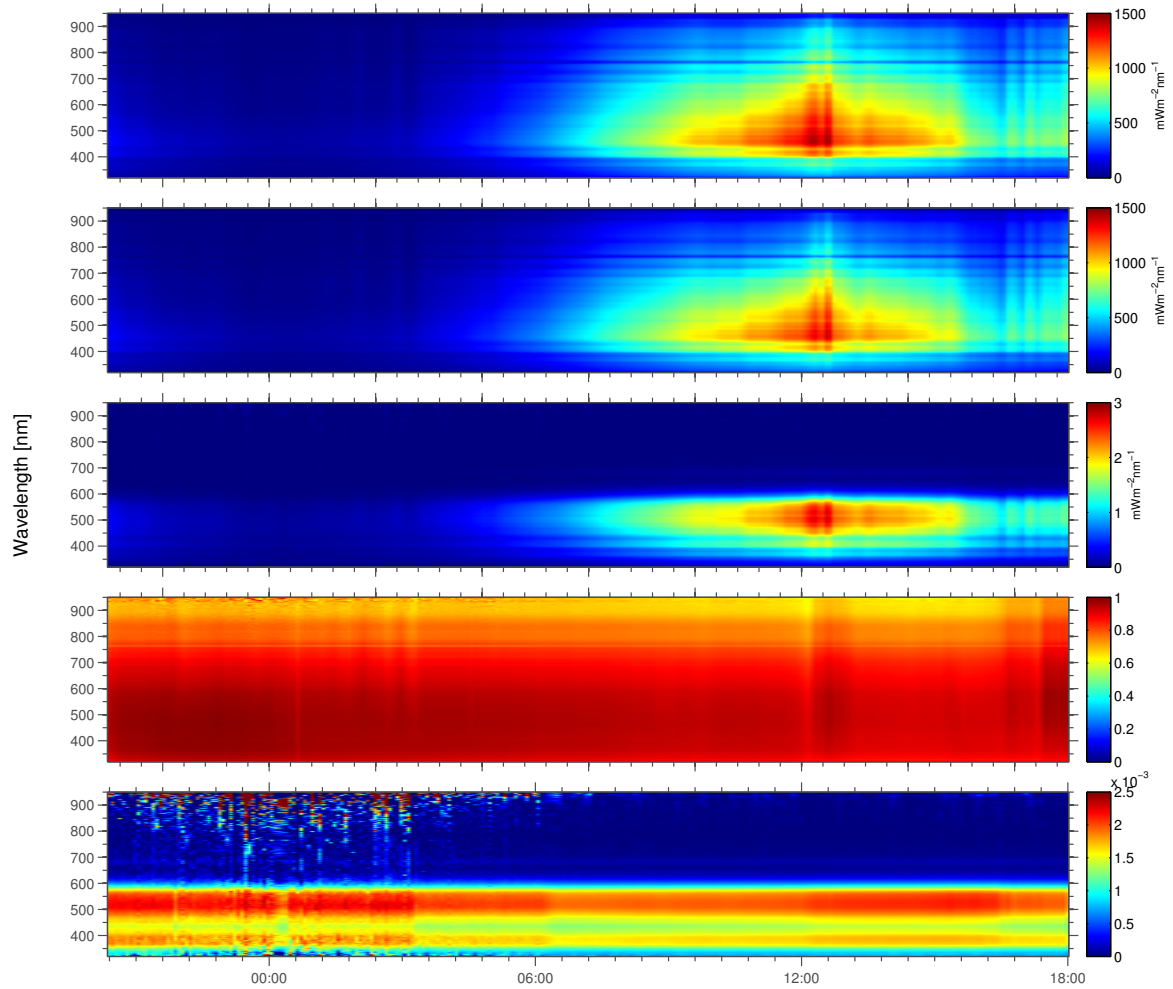


Figure 63: Results of under-ice light measurements on 03 January 2013. From top to bottom: incoming irradiance; reflected irradiance; transmitted irradiance; albedo; transmittance.

9. Sea-Ice Mass-Balance Buoys

Two SAMS sea-ice mass balance buoys, each with 240 thermistors at 2 cm spacing, were deployed during the campaign. The instruments are powered by 50 alkaline D-cells, and transmit GPS, temperature, heating and status data via a satellite link. The data are accessible at <http://martech.sams.ac.uk/awi/>.

9.1. IMB AWI01

In 2011, we reported problems with our SAMS ice mass balance buoy (referred to as IMB AWI01), leading to a data loss over a large period. We reassembled the device in 2012 with a spare mainboard and a new string of 120 thermistors at 4 cm spacing, but the problems could not be solved at first. Finally, we got it to work more or less reliable in August, but still at least one segment of the string (24 sensors) was broken. By removing the broken segment and mounting the entire string reversely, we managed to obtain a temperature profile of 96 working sensors during final testing. In contrast to last year, a regular measuring interval could be defined and the data transfer via Iridium was working.

On 10 August 2012, we froze the IMB into the sea ice at ATKA08 in a distance of 2 m from the AWS. The power supply was provided by 3 battery packs with 4 lithium D 3.7V (19200mAh) Batteries each. Please refer to 64 for all relevant sea-ice parameters during deployment. It was later recognized that data was not sent by the unit for unknown reasons. On 11 August 2012, the AWS site was visited again to check all cables and plugs of the IMB, and to reset the mainboard. Fortunately, the unit was then able to transmit its data via Iridium. But it turned out that 11 sensors at the bottom end of the string were corrupt.

9.2. IMB AWI31

Sea-ice mass balance buoy AWI31 was tested on the roof of the station for one day before it was frozen into the sea ice on 21 November 2012, next to the weather station at ATKA03. Thickness measurements in the bore-hole yielded a sea-ice thickness of 245 cm, a snow depth of 1 cm and a freeboard of about 40 cm. Determination of freeboard was difficult due to masses of ice platelets clogging the borehole. The hole was filled up with snow, but the part above the water surface did not refreeze until the end of the campaign. This has to be taken into account when interpreting the data.

Our measurements of sub-ice platelet layer thickness revealed several interfaces within the layer which varied in strength. Sub-ice platelet layer thickness was determined as 400 cm. To avoid the floating of the chain bottom in the thick platelet layer, the initial bottom weight was doubled. At first, the chain was configured to record the data every 6 hours. It was reconfigured to hourly measurements on 11 December 2012 to reveal temperature changes at a higher resolution. During February 2013 the sea ice became nearly isothermal. To save battery life, the measurement interval was set to twice a day since February.

The results of temperature and heating data of IMB AWI31 are provided in Figure 66.

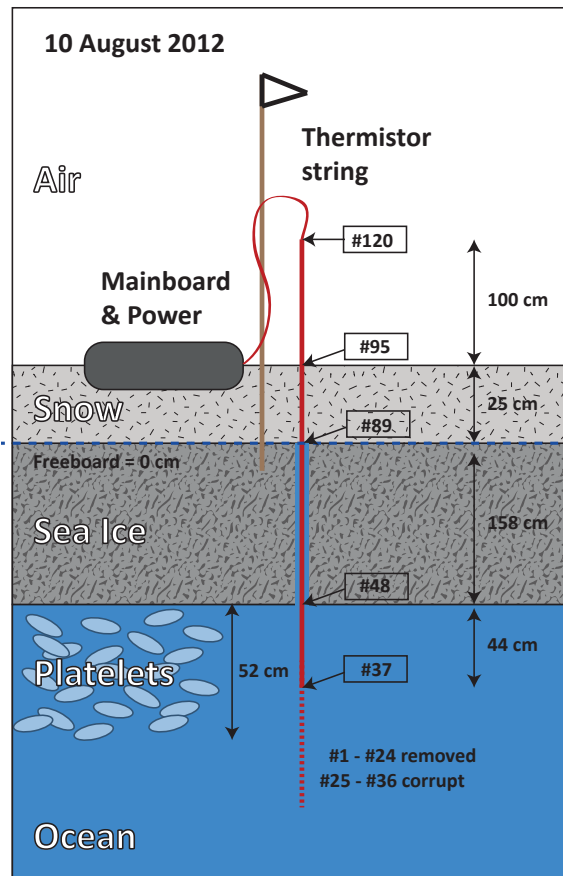
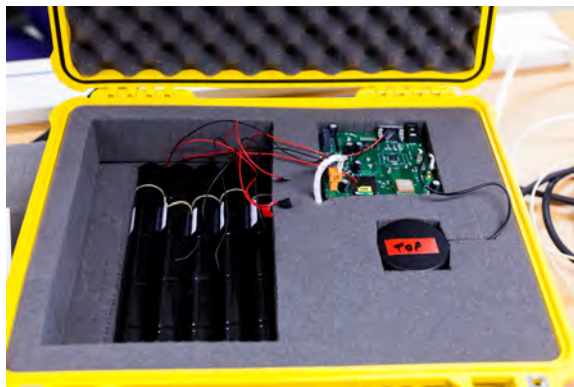


Figure 64: Scheme of thermistor string as set up on 10 August 2012 and various important parameters. The sensors at relevant interfaces are indicated by # following the sensor number. These were calculated by values of snow depth and sea-ice thickness as measured prior to deployment. The thickness of the sub-ice platelet layer was estimated by “feeling a resistance” by gently pulling a modified thickness gauge.

Table 10: Thermistor numbers at interfaces between media

Interface	air/snow	sea ice/snow	freeboard	sea-ice bot.	platelet bot.
AWI31	22	22	42	165	
AWI32	32	52	56	115	150



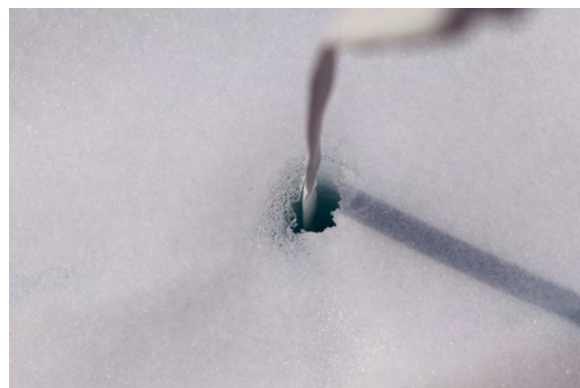
(a) IMB Case



(b) Iridium modem with IMEI



(c) Deployment, 21.12.2012



(d) Chain, 28.12.2012

Figure 65: Photos of sea-ice mass balance buoy AWI31 (Mario Hoppmann).

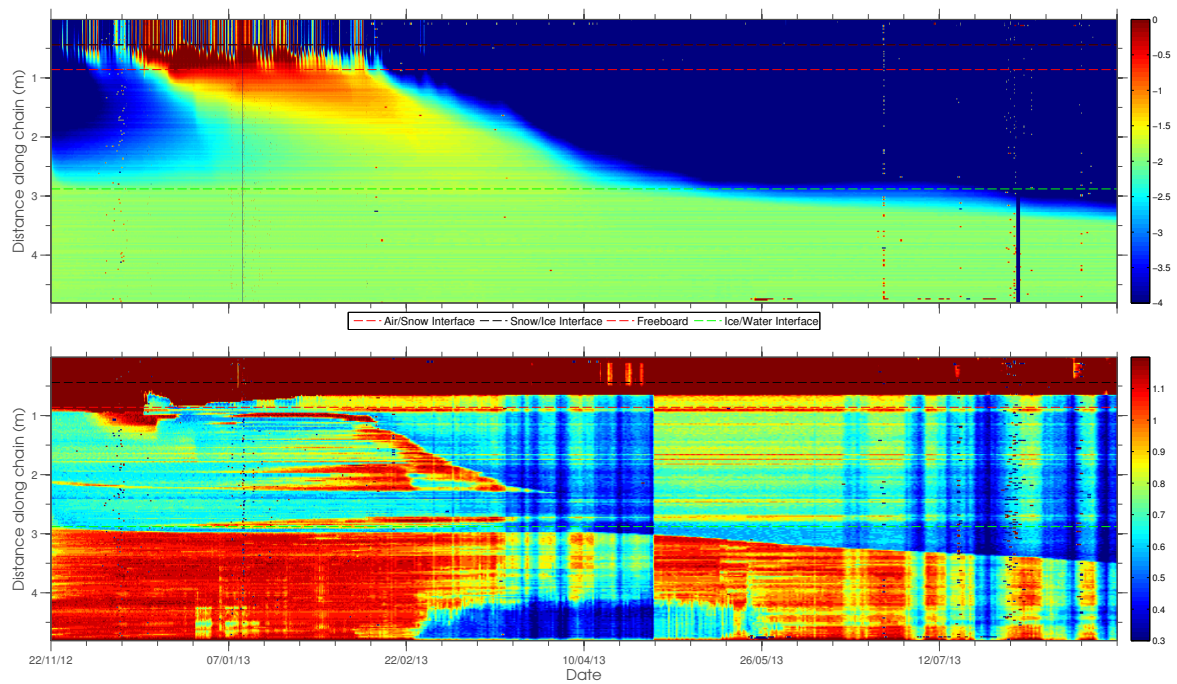


Figure 66: Temperature and heating data of IMB AWI31

9.3. IMB AWI32

The second IMB (referred to as AWI32) was also tested on the roof on 06 December 2012, but problems with the initialization of the chain arose. After unplugging and cleaning all connectors, the chain was finally recognized by the microcontroller and data was transmitted successfully. We decided to deploy the mass balance buoy on the relatively newly formed sea ice, further north in the Bay. Based on TerraSAR-X imagery we picked a suitable spot, $70^{\circ}33.146' \text{ S } 007^{\circ}48.212' \text{ W}$, and this site is referred to as IMB32 in this report. But due to bad weather conditions we were not able to deploy the unit there before 13 December 2012.



(a) Iridium modem with IMEI



(b) After deployment

Figure 67: Photos of sea-ice mass balance buoy AWI32 (Mario Hoppmann)

Thickness measurements in the borehole yielded a sea-ice thickness of 126 cm, a snow depth of 40 cm and a freeboard of about 4 cm. The platelet-layer had a low density, and thickness was determined to be around 70 cm.

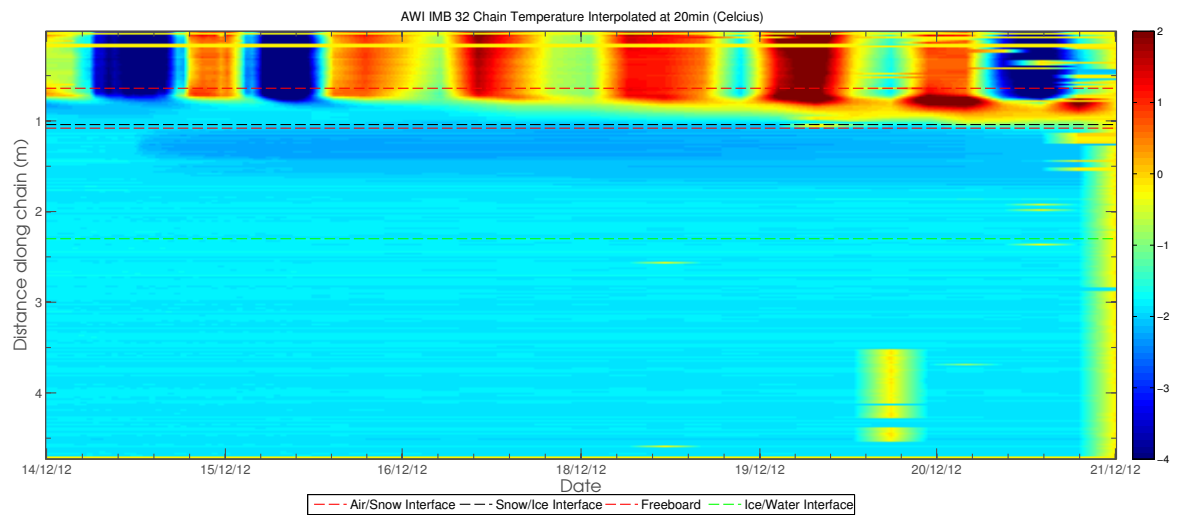
Table 11: Bore-hole measurements at site IMB32

	z_snow [cm]	z_seaice [cm]	FB [cm]	z_platelet [cm]
AWI32	40	126	4	70
5m north	34	130	-1	76
5m west	40	124	-1	80
10m west	20	125		60

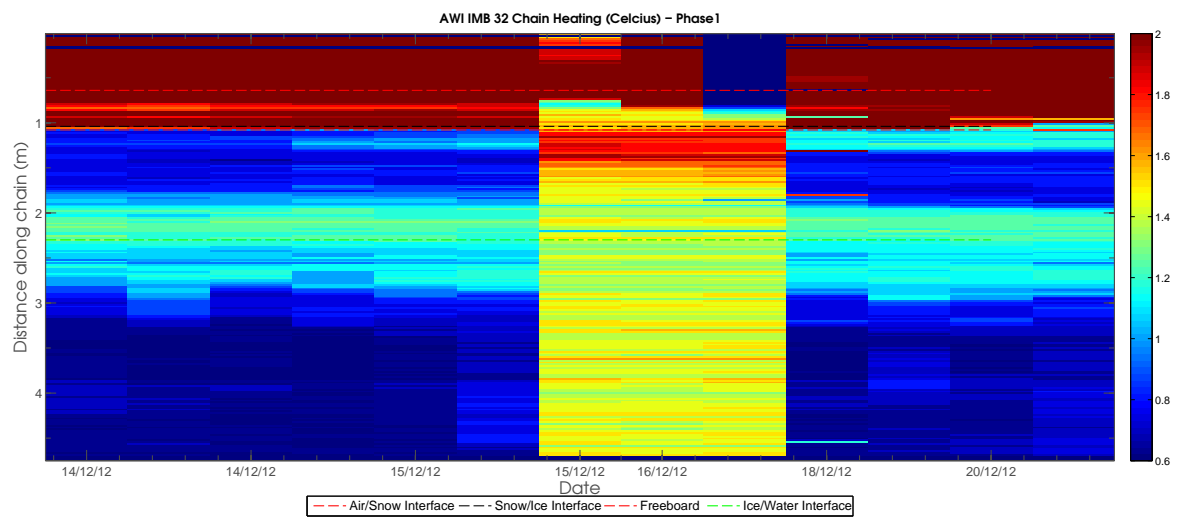
Back at the station, we checked the data via the SAMS web interface and noticed that the unit was not able to send its temperature data. The day after, the site was visited again to solve the problem. After unplugging and cleaning the connectors, we checked the status files on the SD card and made sure that the chain was recognized by the controller. The unit was then configured at a measurement interval of 6 hours, with hourly temperature profiles.

In the next days, sea-ice conditions were considerably worse, especially on the thin sea ice, so we decided to recover the instrument on 21 December 2012 to avoid the loss of the instrument. The chain was slightly damaged during recovery.

The results of temperature and heating data of AWI32 are provided in Figure 68.



(a) Temperatures



(b) Heating

Figure 68: Temperature and heating data of IMB AWI32

10. The Unintended Drifting Station

On 27 August 2012, we planned to visit sampling site ATKA08 to look after the instruments and to copy the data recorded by AWS1, RS1 and IMB AWI01. About 100 m west of ATKA08, we were standing right at the edge of a large area of open water, with no possibility to go further (Figure 70). It was obvious that a part of the land-fast sea ice had broken off and drifted out of the Bay, carrying along our instruments. After checking the position data of IMB AWI01, which were still transmitted via Iridium but haven't been checked for a longer period (the buoy was thought to be stationary), we noticed that the outbreak had already happened about 7 days earlier (21 August 2012, Figure 69), during a heavy storm.

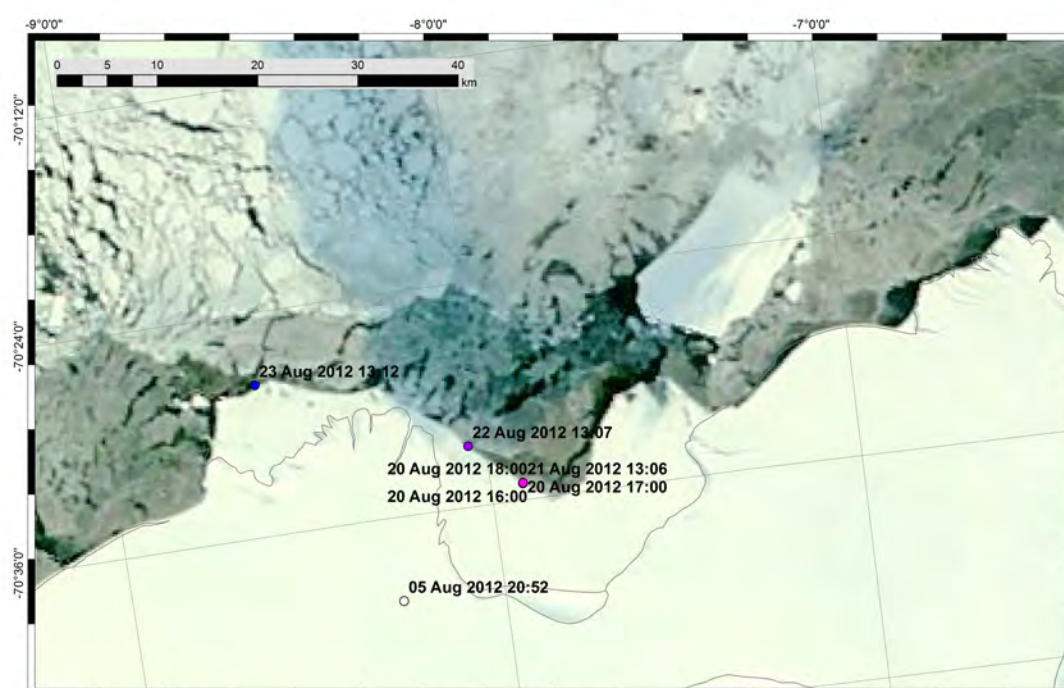


Figure 69: Map of Atka Bay and IMB AWI01 GPS positions around 20 August 2012. Apparently the outbreak happened between 21 August 13:06 and 22 August 13:07. On 23 August, the floe had already left Atka Bay in westward direction. Background: MODIS.

We can only speculate about the possible causes, but a combination of tidal motion, high wind speeds and possibly icebergs touching the fast-ice edge most likely contributed to this incident. We immediately adjusted the measurement interval and switched off the energy-consuming hot-wire anemometer mode to save battery life. Figure 71 shows a plot of the drift track. The last Iridium message was received on 26 August 2013, in the central Weddell Sea.

As a consequence, we prepared our backup instruments and deployed them at ATKA03 at the beginning of October as described in the previous chapters.

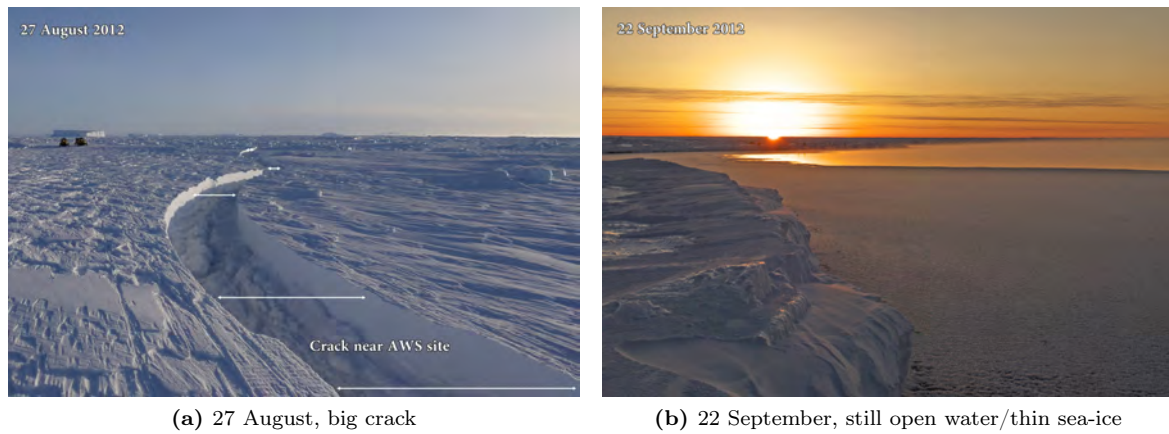


Figure 70: Sea-ice edge near ATKA08, the former site of our autonomous measurements. Photos: Thomas Schmidt

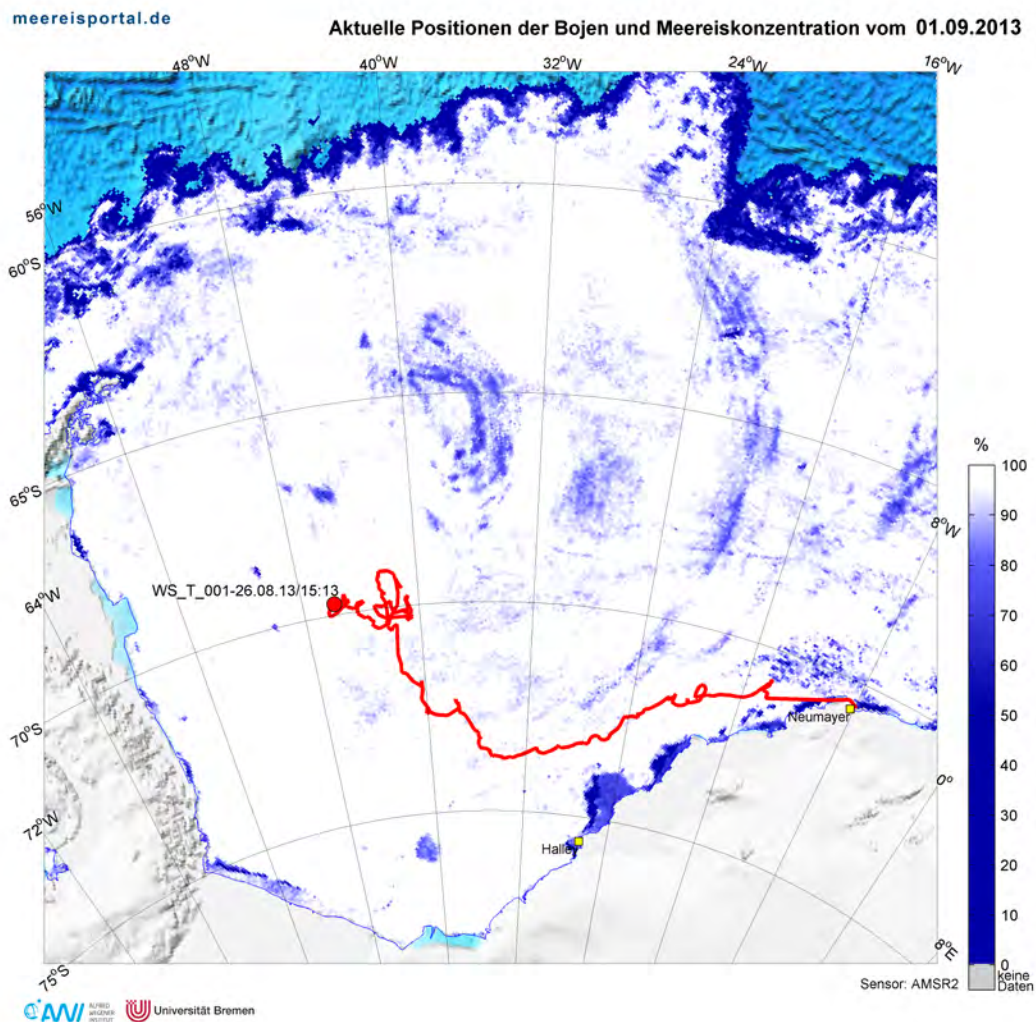


Figure 71: GPS positions of thermistor buoy between day of outbreak (20 August 2012) and 27 February 2013. Image courtesy of Jörlund Asseng.

11. Snow Observations

This section focuses on the snow observations carried out during the SIMBIS field campaign between November 2012 and January 2013. Snow-depths data recorded parallel to EM transects between July 2012 and January 2013 is shown in section 6.1.

In the following, the general procedure is described, as well as a first quick-look into the recorded data. Special emphasis lies on the measurements carried out with the Snow Fork, an instrument to measure snow liquid water content and snow density in a vertical profile. This data is of high relevance to link snow processes to remotely sensed microwave satellite data.

In addition to the punctual measurements of snow pits, snow transects were recorded at regular stations, measuring the snow thickness and surface temperature every 5 m, ranging between 50m and 100m in north, south, west and east direction.

11.1. General Observations

The general snow observations are closely linked to the general meteorological observations, e.g. due to the high impact of temperature changes on the snow pack and the ongoing metamorphism. Also redistribution of existing snow due to high wind-speeds as well as new snow fall have an impact on the snow-pack. Especially the eight day long storm period between December 5th, 2012 and 12 December 2012 as well as the onset of melt due to increasing air temperatures at 16 December 2012 changed the properties of snow pack significantly. This change is reflected in the in situ measurements as well as in the TSX data.

11.2. Snow Pits

During the field campaign, a total number of 39 snow pits were recorded. In addition, several small pits were created to describe the upper most 10 or 20 cm in temperature and density. Furthermore, snow-surface descriptions were made and photographs were taken to document changes especially in the surface roughness.

In general, snow pits reveal information about the nature of the snow pack in terms of temperature and density profiles as well as its stratigraphy describing the different layers inside the snow pack. These layers are characterized by changes in parameters like liquid water content, grain size, snow hardness or snow crystal type. These parameters have a high spatial variability and also change during the seasons due to melt/freeze cycles and snow metamorphism processes. A good understanding of these parameters is necessary to connect the found results to satellite microwave imagery.

Hence, it was tried to sample respective areas several times during the field campaign

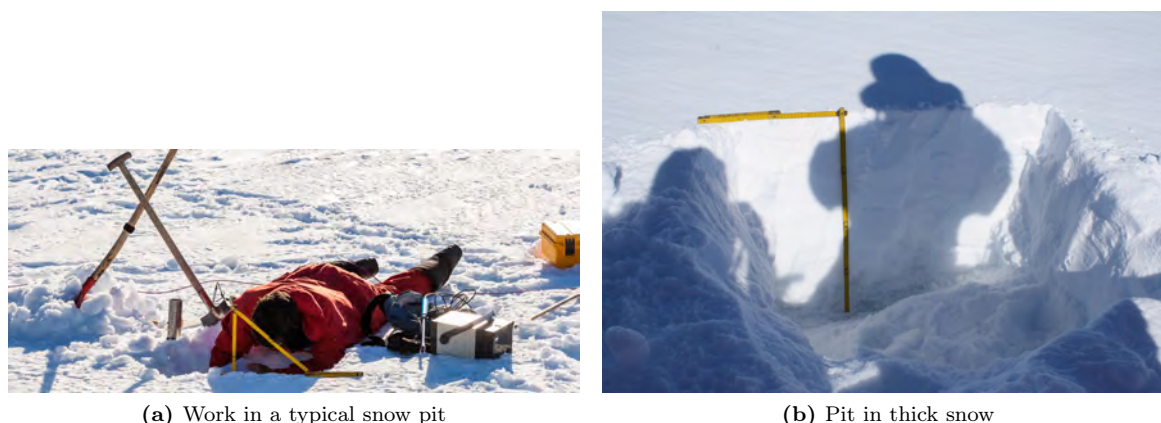


Figure 72: Snow Pit. Photos: Mario Hoppmann, Stephan Paul

to reveal seasonal changes yet get a good spatial overview of the whole Atka Bay. In addition to the six ATKA-Stations, snow pit measurements were conducted along transect measurements (Albedo, GEM-2) or in areas of interest pointed out by uncommon signals in near real time TSX satellite imagery.

To record the snow temperature profile, a simple penetration thermometer was used. In general, the temperature was measured every 5 cm. The density was measured with a metal tube of known volume and weight, that was driven into the snow pack by impact. Afterwards, its weight was measured using a spring balance. We tried to get a density measurement of at least every layer in the snow pack. However, a minimum snow depth was necessary to do so. These “bulk” density measurements will be compared to the snow fork measurements of density whenever possible.

The stratigraphic parameters were retrieved in different ways. The hardness was estimated by the degree of resistance the snow pack offers towards penetration of the observers fist, four fingers, one finger, a pen or a knife. The grain size was measured using a reference table. The crystal type was estimated using a magnifying glass and classification scheme of the crystal shape. The liquid water content was categorized into the classes “dry”, “moist”, “wet” and “slush”.

11.2.1. Preliminary Results

Some preliminary results are presented in Figures 73 and 74. Each plot for each location is separated into three subplots, showing the temperature profile (left), liquid water content and snow density (middle) as well as the hardness and grain-size (right). Note that missing data often results from a too thin snow cover, that did not permit all measurements.

In general, the temperature regime in the snow pack warms drastically from the beginning to the end of the field campaign. While it is way below freezing in November, the temperature is at freezing point almost for each measurement at the beginning of January. Only in the very thick snow-pack at ATKA-16, the temperature still reaches values of minus two degrees centigrade and below. Due to snow metamorphism, the grain size generally increased in January compared to the November measurements. However, the link between those snow-pit measurements and the TSX data has still to be evaluated.

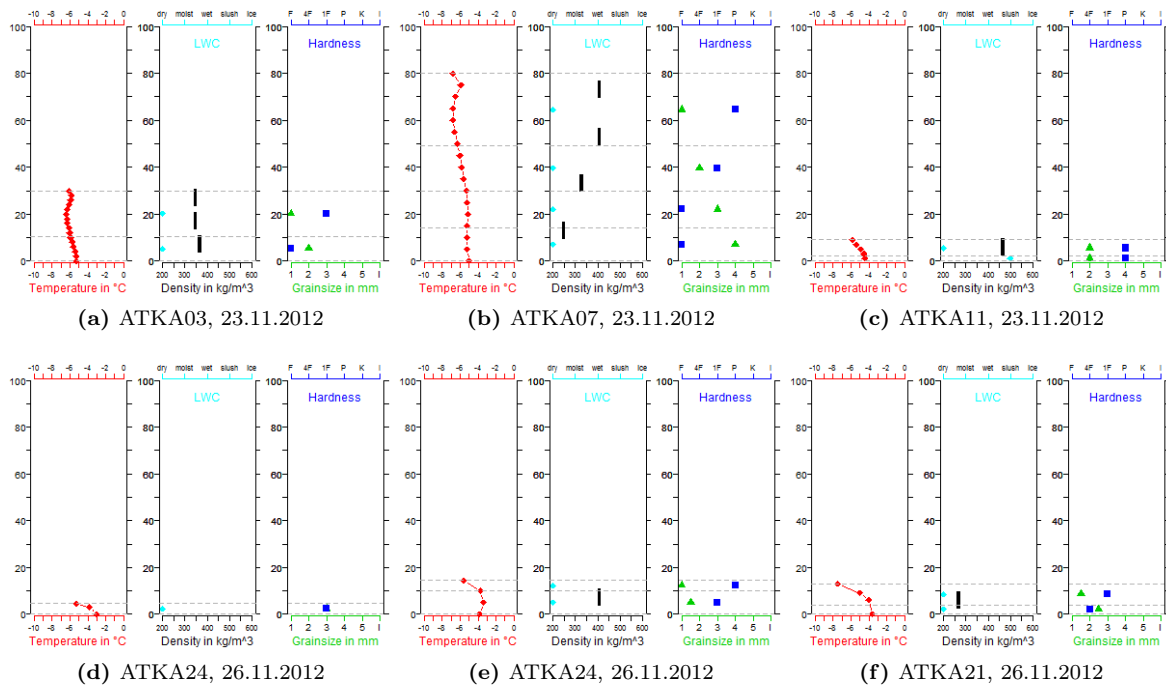


Figure 73: Exemplary figures of snow properties taken from snow-pit measurements on 23 and 26 November 2013. These show the conditions in the snowpack at the beginning of the field campaign. Note that there was now snowpit conducted at ATKA-16. Left-hand side: Temperature profile (red), Middle: Liquid water content (lightblue) and snow density (black), Right-hand side: Hardness (darkblue) and grainsize (green).

11.2.2. Snow Fork Measurements

During the active field campaign, an additional instrument became available: The snow fork. It utilizes the dielectric properties of snow to estimate liquid water content and the snow density. However, the uncertainty rises in very inhomogeneous and wet snow. Due to the late arrival of the instrument, only 9 snow pit measurements could be supplemented by snow fork measurements between 27 December 2012 and 07 January 2013. However, this was probably there more interesting period during the campaign in the matter of rising liquid water content and melt/freeze changes as well as metamorphism in the snow pack.

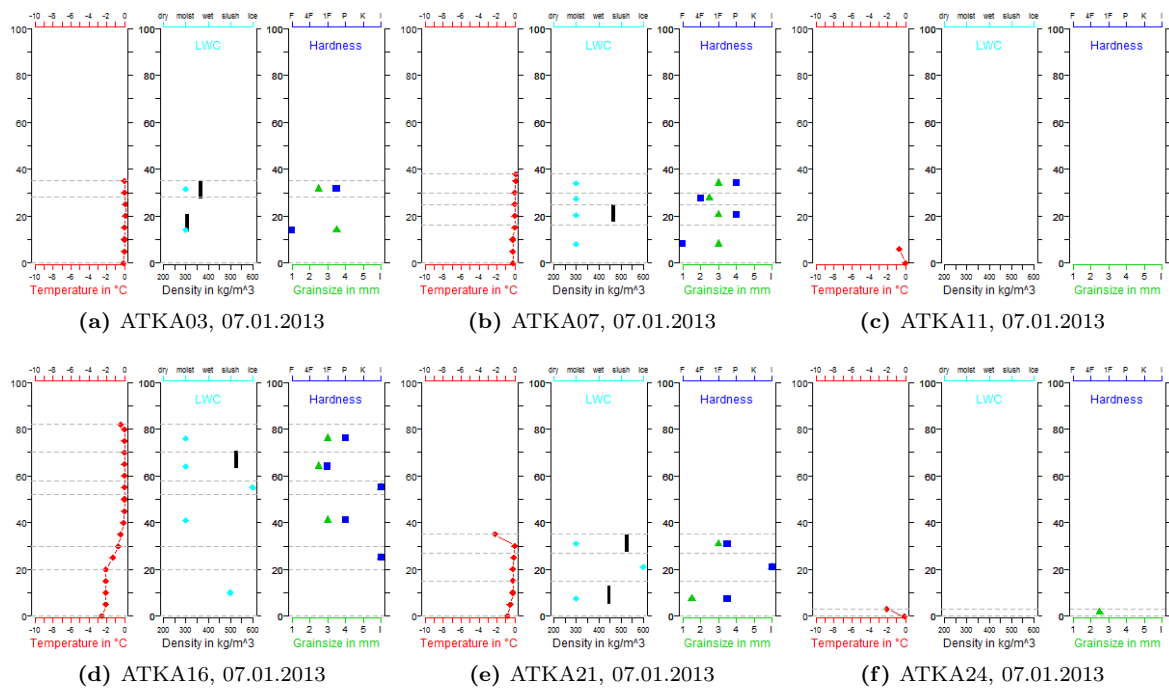


Figure 74: Exemplary figures of snow properties taken from snow-pit measurements on 07 January 2013. These represent the conditions in the snow pack at the end of the field campaign. The setup complies with that of Figure 73.



Figure 75: Snow Fork. Photos: Mario Hoppmann

11.3. Snow Transects

Even though snow pits are tried to be located in a representative area for the surroundings, they are still only very local measurements. In order to get further information of the surroundings, snow thickness transects as well as surface temperature transects were the second important part of the overall snow observations. These transects were done by measuring snow thickness and surface temperature every 5 m for 50/100m northwards as well as south-, west- and eastwards. Figure 76 shows exemplary distributions of snow depths at four different sampling sites.

11.4. Other Snow-Depths data

In addition to the transects in the vicinity of the the snow pit measurements, snow thickness transects were also carried out along side the albedo and EM sea-ice thickness measurement transects done in the Atka Bay. Here, approximately every 500 m three to five measurements were done to have a measure of representativeness and to reveal small scale changes in snow depth.

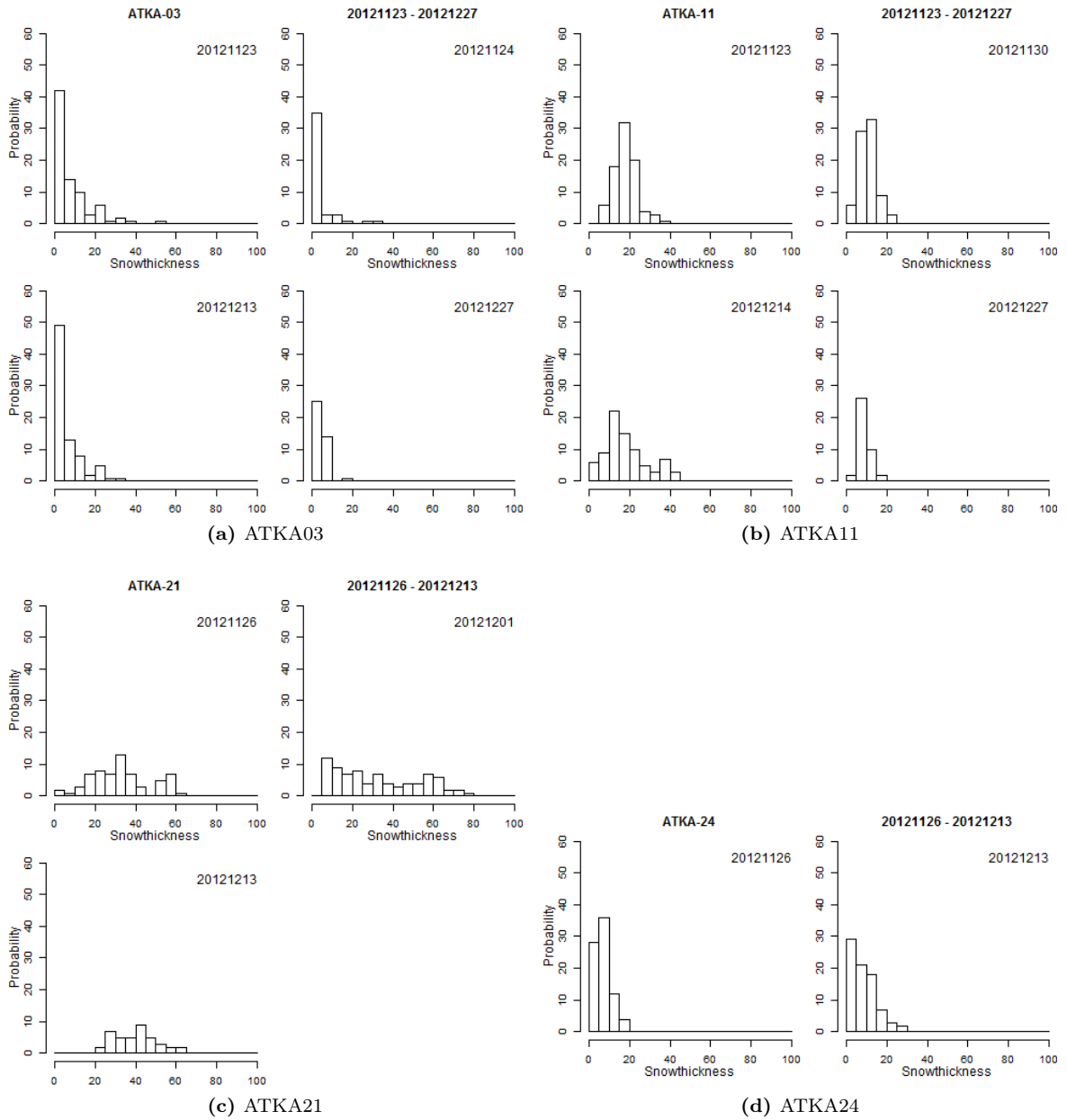


Figure 76: Histograms of snow depths at different sampling sites / dates

12. Observations with Under-Ice Cameras

12.1. Platelet Camera

During the SIMBIS campaign, we used an under-ice camera system to visually inspect the platelet layer, and recorded about 20 hours of sub-ice video footage. The system consisted of a power and control unit (PCU), a 50 m cable and a highly specialized camera head (Figure 77). Power was supplied by a Honda generator. A regular USB video grabber (TerraTec Grabster AV 450 MX) was used to transfer the camera image to a Panasonic Toughbook in real time, where it was recorded by the video editing software “MAGIX Video easy”. The control unit enabled us to manually adjust pivot and rotation angles, focus distance, as well as illumination in real time.

The most important parameters of the camera head are summarized in Table 12.

Table 12: Technical specifications of camera system (source: visatec)

Image sensor	1/3" IL CCD
Video out	FBAS
Resolution/Lines	400 lines
Video resolution	720 x 576 pixel
Sensitivity	0,3 Lux
Optics	f=3.6 mm
Focus	5 mm - infinite
Pivot angle	+/- 110o
Rotation	infinite
Illumination	LED high intensity
Glass cover	acrylic glass
Housing	stainless steel
Dimensions	34 mm x 90 mm (d x l)
Weight	150 g
Temperature range	-150 bis +500
Pressure	5 bar (opt. 50 bar at d=36mm)

The camera system enabled us to accurately determine the platelet-layer thickness. With its diameter of only 3,4 cm, it was possible to lower the head through a regular 5 cm diameter borehole, without the need of drilling a bigger hole. We experienced that our thickness gauge technique regularly underestimated platelet-layer thickness by as much as 60 cm. The reason lies in the fact that the metal rod of the thickness gauge needs a certain threshold of platelet density to bear enough resistance for the user at the surface to feel. This brings up the need for a definition of “platelet-layer thickness”. We most often used the thickness gauge technique, so for our purposes we defined the thickness as the difference between the first noticeable resistance and the sea-ice underside. But as the camera showed us, there often was a layer of very loose platelets below that “first noticeable resistance”, which varied in thickness. In the end, depending on how “platelet-layer thickness” is defined, the one or the



Figure 77: Under-ice platelet camera. Photo: visatec

other method is more accurate.

The camera system was used parallel to under-ice radiation measurements, during which the position of the under-ice radiometer was monitored.

At some stations we filmed Amphipods grazing in the platelet layer, who were drawn to the camera lights.

Table 13: Dates and stations of recordings

Station	Date	Comment
ATKA03	21.11.2012	
ATKA11	21.11.2012	
ATKA03	23.11.2012	
ATKA11	23.11.2012	L-Arm, Thickness gauge
ATKA11	30.11.2012	L-Arm
ATKA21	01.12.2012	Amphipods
SNOW01	03.12.2012	
SNOW02	03.12.2012	Amphipods
ATKA21	28.12.2012	
ATKA11	29.12.2012	L-Arm, CTD, Thickness gauge

Some of the problems we faced in the field are the following:

- Like every other instrument we wanted to operate under the sub-ice platelets, we also had problems pushing the camera head through this layer. We needed to put the cable through metal poles, which we used to push the camera head through (Figure 78). By doing this, the handling unfortunately became more difficult, as we needed several segments of these heavy, 2,5 m long metal poles. One of the biggest problems that arose was, once we needed two or more of these segments, their connecting element made a larger (core)hole necessary. This lead to the fact that the setup time increased from



Figure 78: Under-ice platelet camera in the field. Photos: Mario Hoppmann

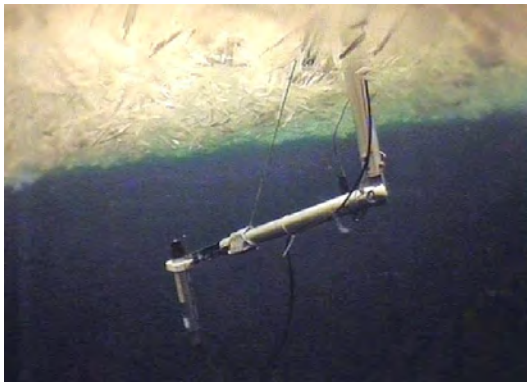
two minutes to around half an hour. A better solution to this problem is needed in the future.

- Light conditions under thick sea ice and snow often made it impossible to obtain high-quality recordings. The best quality was achieved at ATKA11 in late December, when most of the snow was transformed to snow ice by surface flooding.
- Although the camera is principally easy to use, it still takes some time to get used to the controls, especially adjusting the focus right was a major challenge during low-light conditions and takes a bit of practice.

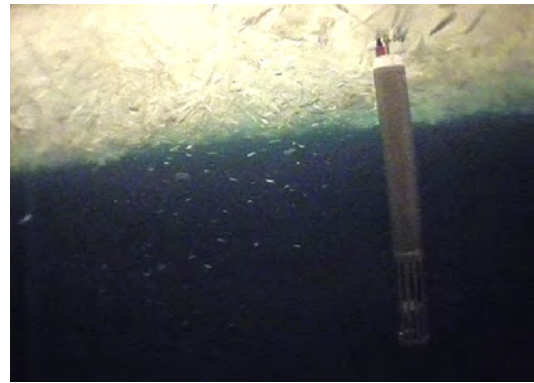
To summarize our experiences with the “platelet camera”, it is in principle well suitable for the determination of platelet-layer thickness, and to get a visual impression of the spectacular world below the solid sea ice. Once we have a solution to the “pole problem” the handling in the field will be very good. Some highlights of our videos are provided as screen shots in Figure 79.

12.2. PASATA Videos

Between 21 and 30 November 2012, the PASATA project (Ilse van Opzeeland and Karoline Thomisch) recorded continuous under-ice videos at xxx to monitor the under-water behavior of seals. These videos unintentionally contributed to the SIMBIS campaign by filming a nearly continuous uprise of buoyant ice platelets, which had its maximum at 25 November, and ceased nearly completely at 30 November. Figure 80 shows four screen shots of a video recorded on 25 November 2012, where the highest amount of rising ice platelets was observed.



(a) L-Arm



(b) CTD



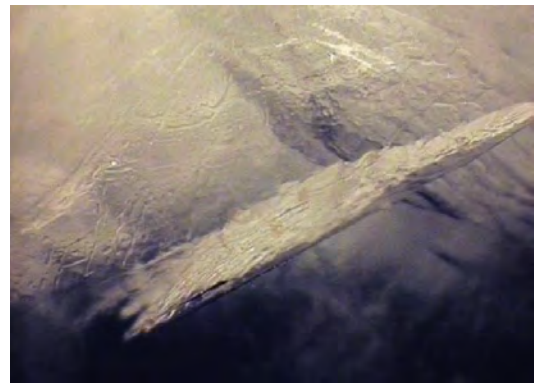
(c) Thickness Gauge



(d) Amphipods



(e) Good light conditions



(f) Platelet



(g) Low light



(h) LED illumination

Figure 79: Platelet camera images. Photos: AWI

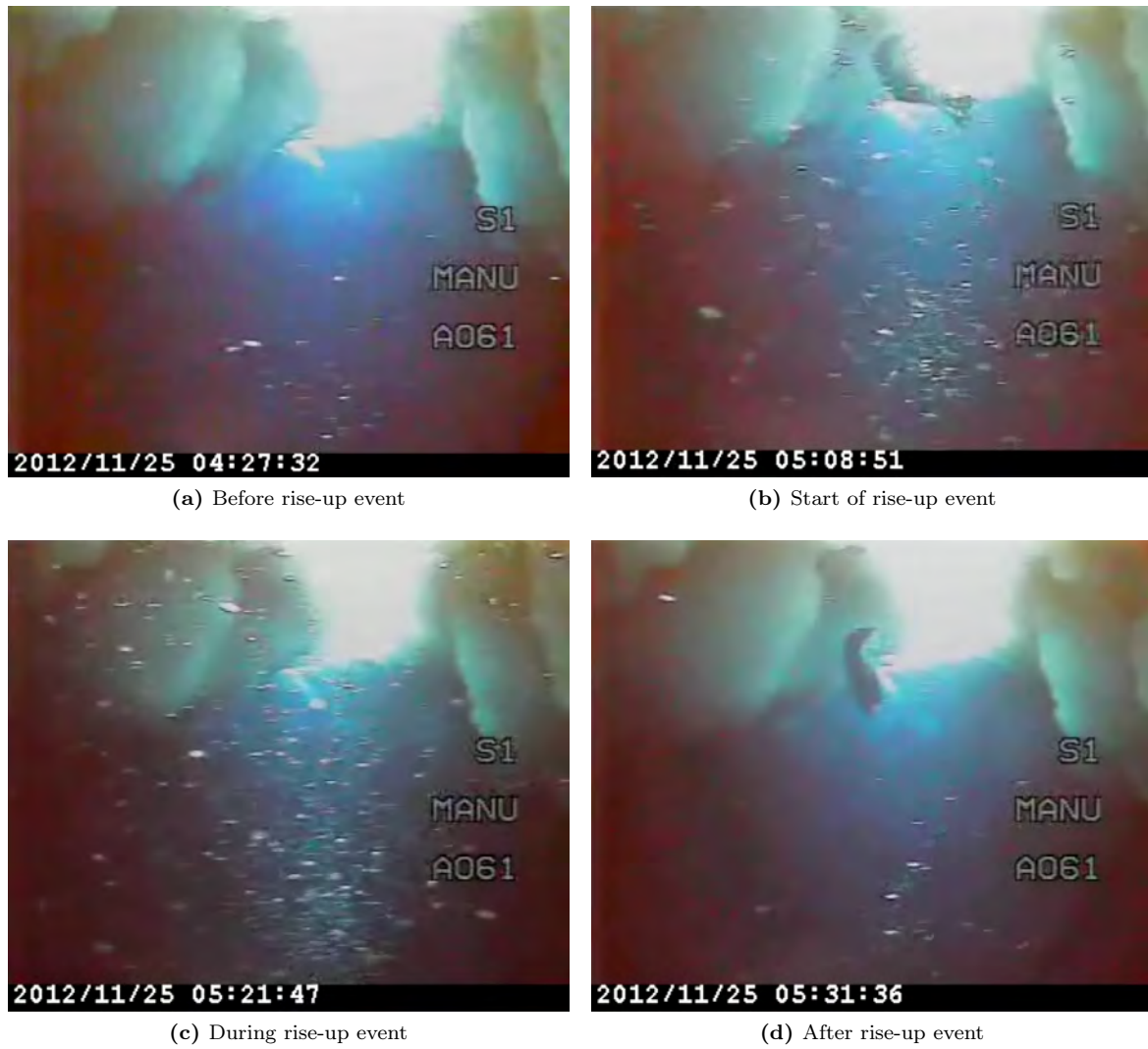


Figure 80: Screen shots from an underwater camera before, during and after massive platelet rise-up event (©PASATA project).

13. Oceanographic Conditions at Atka Bay

Ice platelets generally form deeper in the water column in supercooled water masses, where they may grow or float upwards to the sea surface. These conditions only occur in the presence of a heat sink at depth, like ice shelves, because it is not generally possible to cool the water column below the surface freezing point by the removal of heat to the atmosphere. The formation of ice platelets in the cavity between the floating ice sheet and the bedrock beneath is part of a process termed “Ice Pump”, which was described by Lewis and Perkin (1986), and is summarized in Figure 81.

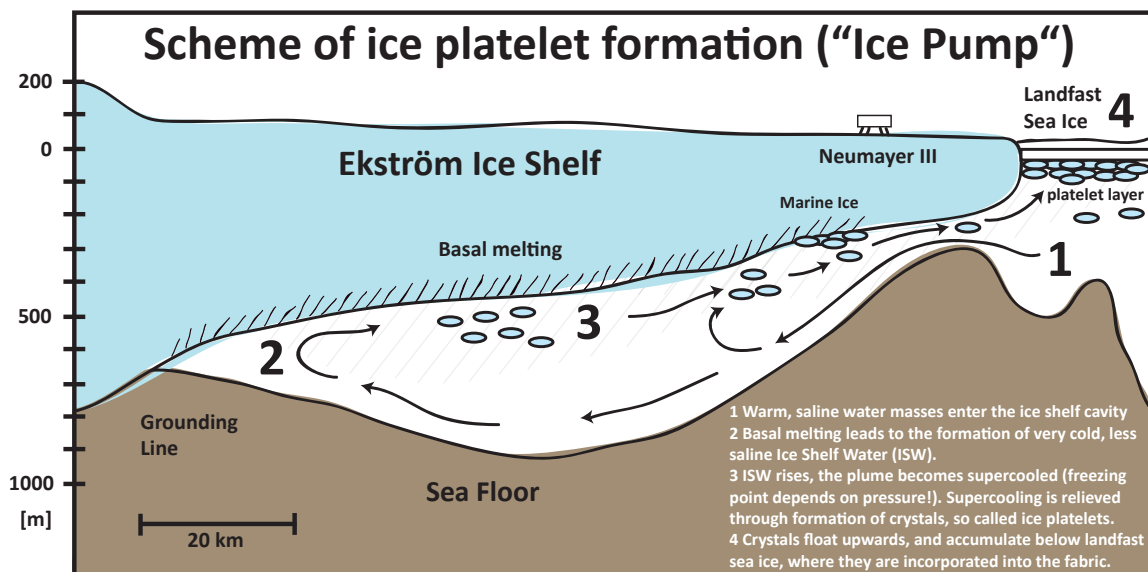


Figure 81: Ice Pump, after Günther and Dieckmann (1999)

In this field report, two different sets of CTD data from 2012 are shown to investigate the formation of ice platelets at depths. The first dataset is provided by a permanently installed CTD under the Ekström Ice Shelf, which records oceanographic parameters every 30 minutes. The second dataset was recorded in November and December 2012 under the landfast sea ice of Atka Bay in the framework of the SIMBIS campaign.

13.1. CTD at PALAOA Observatory

PALAOA (Perennial Acoustic Observatory in the Antarctic Ocean) is a small, unmanned and autonomous research station north of Neumayer III. It is one of the permanent observatories at Neumayer and is operated by the Ocean Acoustics Group at AWI. Several hydrophones are installed under the Ekström Ice Shelf to record acoustic signals from the marine realm. In addition, a CTD was lowered through the massive ice shelf, primarily to determine the speed of sound necessary to correct the acoustic data.

CTD data from PALAOA is not explicitly part of our sea-ice program, but it is a valuable source of information about the formation processes of ice platelets. The CTD was deployed



Figure 82: The PALAOA observatory. Photo: Lars Kindermann

in 2006, and records oceanic parameters every 30 minutes. In this field report, the data between 2008 and 2013 are shown (Figure 83).

13.2. CTD measurements during SIMBIS campaign

During the SIMBIS campaign, we conducted more than 50 vertical, high-resolution CTD casts below the landfast sea ice of Atka Bay to investigate the prevailing oceanographic conditions during the transition to summer.

Vertical temperature and conductivity profiles were obtained using a *Sea&Sun CTD75M* Conductivity-Temperature-Depth probe (Figure 84). The probe was switched on with a magnetic rod and lowered through regular 10 cm coreholes drilled by a *Kovacs Mark II Coring system* using a 250 m long cable. The cable was connected to the serial port of a *Panasonic Toughbook*, where the data were recorded in continuous mode (all datasets are stored with the maximum possible data rate) using the software *SDA* supplied by *Sea&Sun*. A separate file was saved for up- and downward casts respectively, and the raw data were later exported with the help of the integrated conversion tool.

Several problems arose when attempting to lower the probe through the corehole. Nearly all holes quickly filled with ice platelets floating upwards immediately after taking out the last core segment. By lifting the probe upwards and letting it fall through the hole it was sometimes possible to get the instrument through. But often it was necessary to “fish” a large amount of ice platelets out of the hole to get the instrument through. But even if the hole was free, the underlying high-density platelet layers made it difficult to further lower the

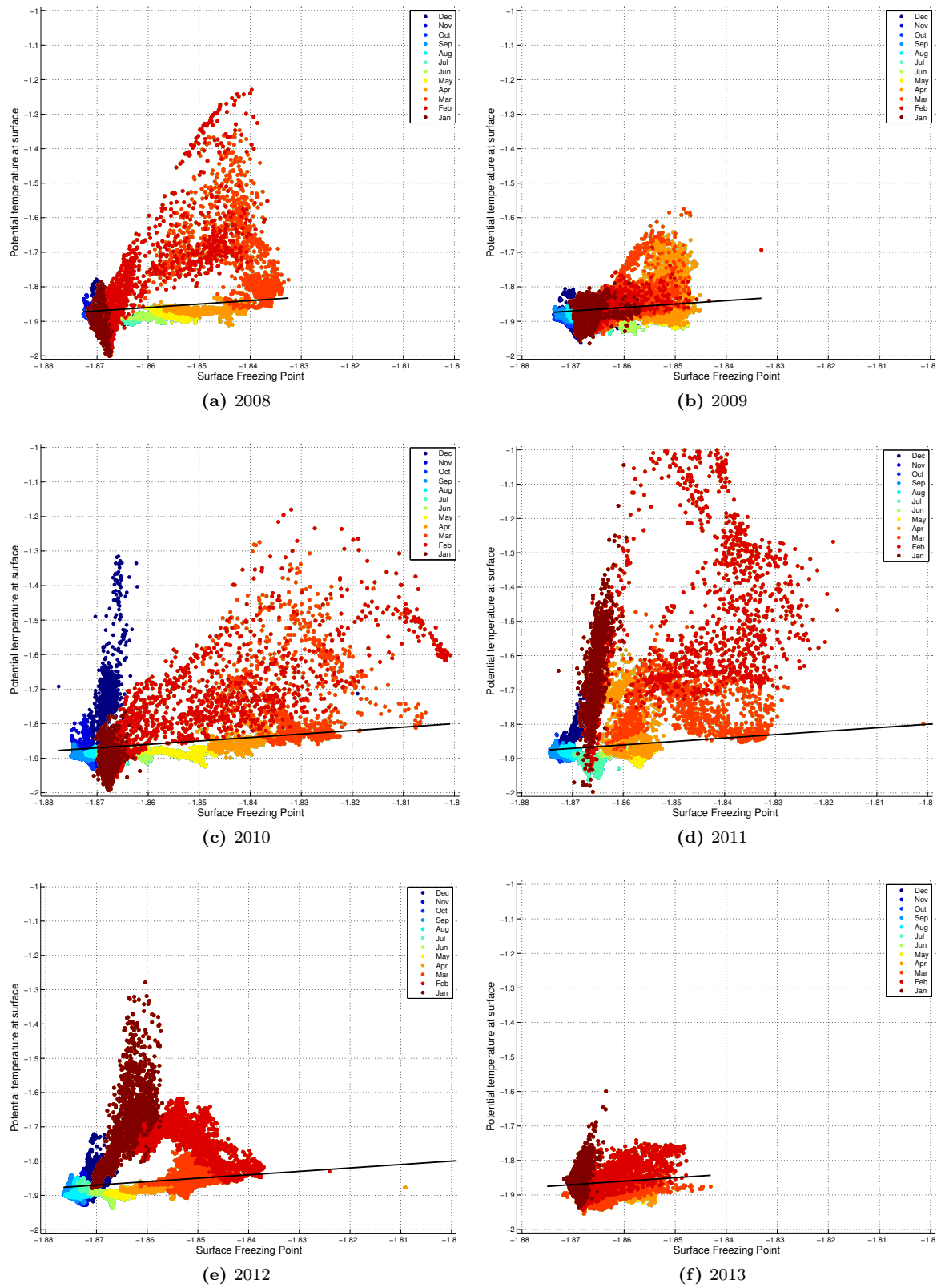


Figure 83: Potential supercooling under Ekström Ice Shelf



Figure 84: CTD in action. Photo: Mario Hoppmann

Table 14: CTD75M specifications (from datasheet). For further specifications, refer to (cite manual here)

Sensors	Principle	Range	Accuracy	Resolution
Conductivity	7-pole-cell	0...70 mS/cm	+/- 0.010 mS/cm	0.001 mS/cm
Temperature	Pt 100 4 pole	-2...+36 °C	+/- 0.005 °C	0.005 °C
Pressure (depth)	piezo-resistive	various ranges	+/- 0.1 % fs	0.002 % fs

probe. A side effect of this problem was the accumulation of small platelets in the cage of the instrument which protected the sensors. This was often visible in a lower salinity value in the real-time data on the screen. The probe was then moved up and down again to get rid of these frazil crystals. Once the salinity returned to plausible values again, the cast was started and the data were recorded. However, it is still possible that the conductivity/salinity values show a large error in the first 10 m.

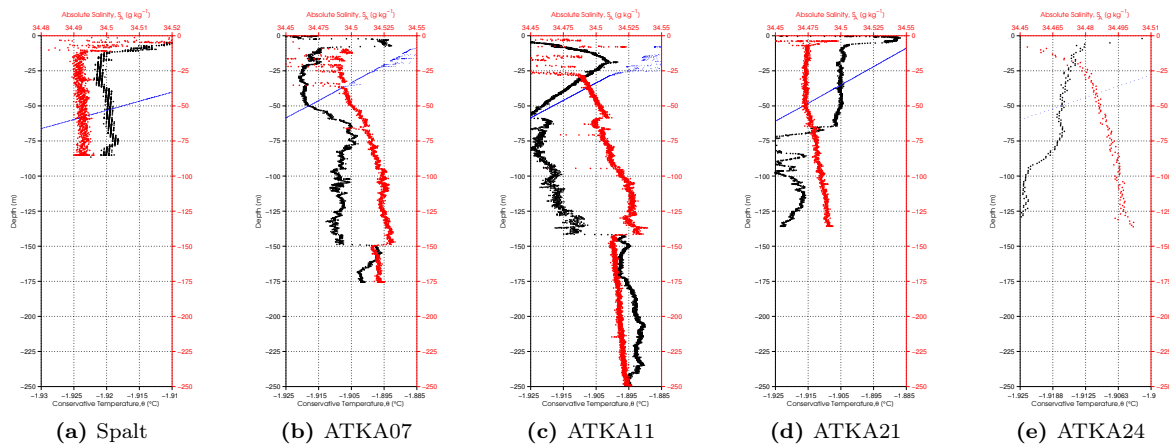


Figure 85: CTD profiles 21 Nov - 03 Dec 2012

Figures 85, 86, 87, 88 and 89 show first results of CTD data obtained between November 2012 and January 2013 at different stations at Atka Bay. Measured temperatures and conductivities have been converted to the absolute salinities and conservative temperature shown here with the help of the gsw oceanographic toolbox for Matlab (citation). The blue curve indicates the in situ freezing point of the water mass in dependence on the absolute salinity and the measured pressure at that point. Conservative temperatures cooler than the in situ freezing point (above the blue dots) are most probably supercooled in situ, which means that these water masses act as a potential source for ice platelets. It is evident from Figures 85 and 86 that in situ supercooling was still present at the beginning of the campaign in the uppermost 50 m of the water column, and ceased between 03 and 13 December 2012. A signature of supercooling is still partly present in the platelet layer a few meters below the sea ice until January 2013, but we are still not sure to which extent the CTD measurements can be trusted when operated directly in the platelet layer.

Generally, the entire water column was very cold (< -1.64 °C) until the beginning of December. After the bad-weather period lasting from 03 to 13 December, a layer of warmer water penetrated Atka Bay from the East. At the end of December, temperatures in the upper 20 m of the water column reached a maximum of -1.64 °C at ATKA11, and rose to -1 °C at ATKA16 at the beginning of January 2013. This led to a strong melting of the sea ice mainly from the inside, which was also reflected in the increased porosity of sea-ice cores taken after 13 December 2012. What is also evident from Figure 86 is that a different water

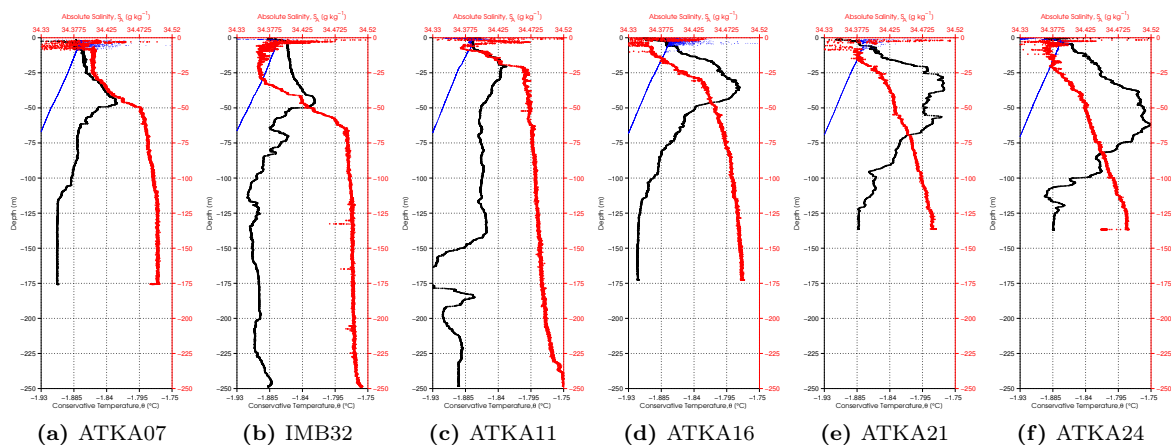


Figure 86: CTD profiles on 13/14 December 2022. Absolute salinity is shown in red, conservative temperature in black. The in-situ freezing point is shown in blue (see text). Different depths result either from running out of cable (250 m, ATKA11) or from reaching the seafloor (other stations). ATKA24 has a lower depth resolution, because the measurement interval was set incorrectly.

mass with lower salinity and higher temperature is sitting at the very bottom of the central Bay (<136 m) in November.

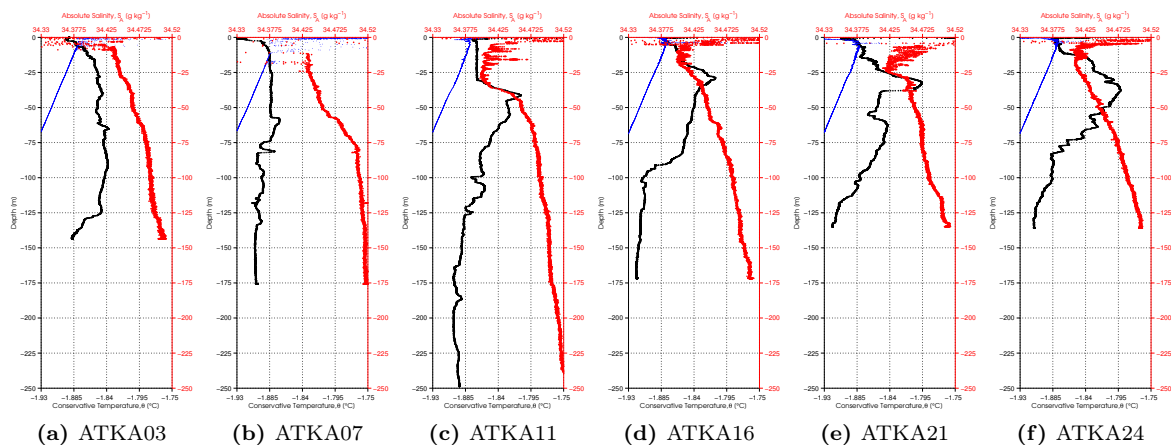


Figure 87: CTD profiles on 19 December 2022

13.3. 24 h CTD profiles at ATKA21 on 03/04 January 2013

As sea-ice thickness determination by electromagnetic induction sounding (described in sections 6.1 and 6.2) critically depends on the water conductivity just below the sea ice, a 24 h long time-series of oceanic properties was obtained at ATKA21 on 03 and 04 January 2013. By doing so, we were able to study the influence of the tidal cycle on the waters of Atka Bay. Starting at 19:00 UTC, the CTD was installed into a borehole at around 2 m depth, just below the sea-ice surface. In addition, a full-depth CTD cast (136 m) was performed every

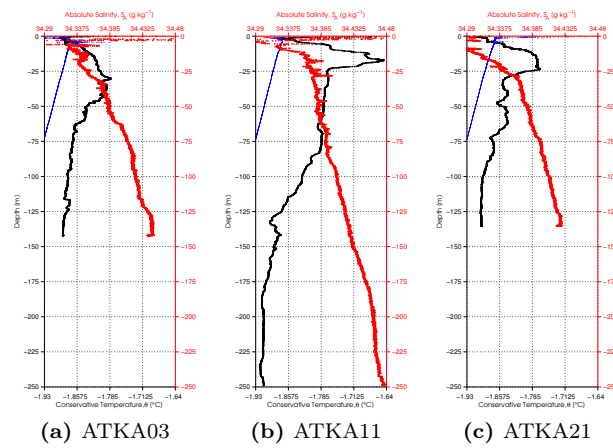


Figure 88: CTD profiles 27 - 29 December 2012

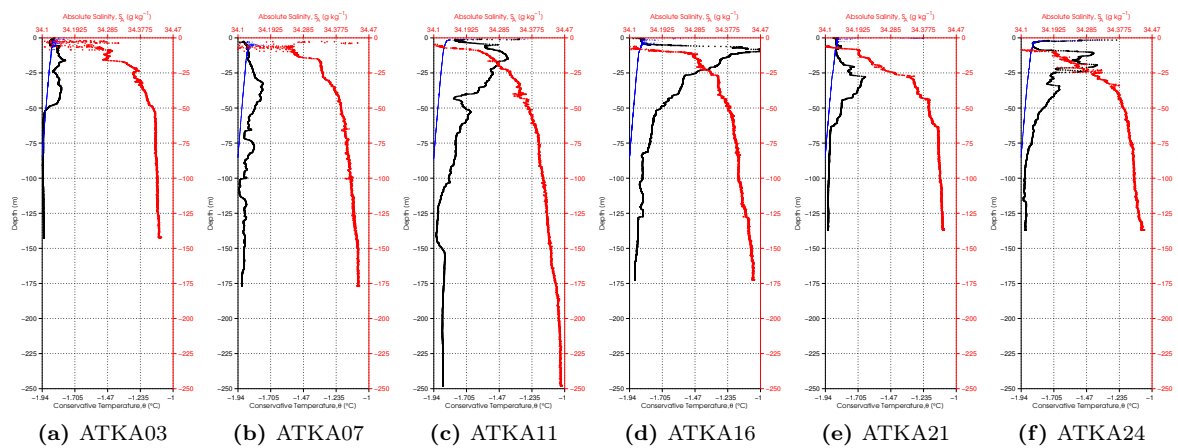


Figure 89: CTD profiles on 07 January 2013

full hour.

The results of the CTD casts are summarized as interpolated color plots in Figure 90.

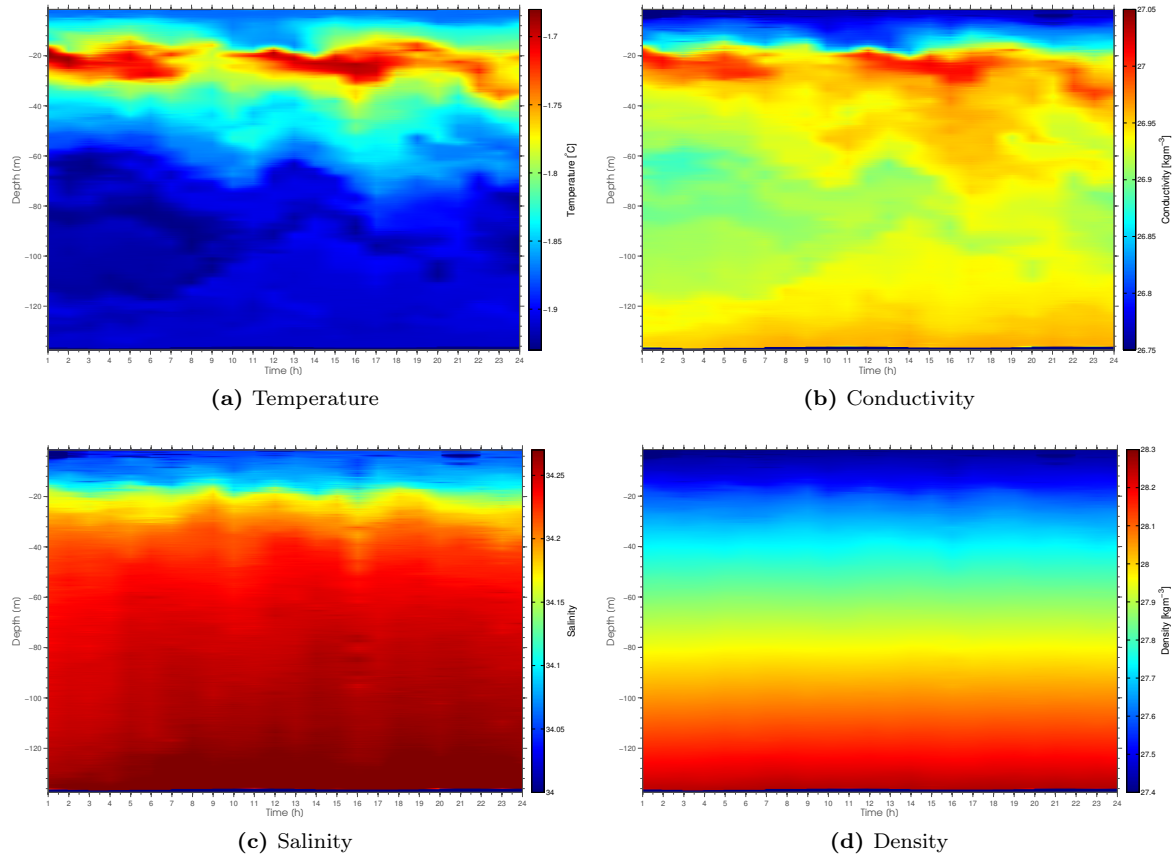


Figure 90: Color plots of interpolated CTD measurements at ATKA21 on 03 January 2013

14. Sea-Ice Cores

A large amount of 10 cm diameter core-holes (>50) were drilled during the campaign, using a Kovacs Mark II Coring System operated on a generator-powered drilling machine. Most of these holes were needed to obtain under-ice CTD profiles and to operate the L-Arm and platelet camera. Therefore, most cores were thrown away and not processed further. Table 15 gives an overview of the 23 sea-ice cores which were used for further analysis.

Table 15: Overview of sea-ice cores processed during campaign. *All samples of the core taken at site SNOW01 on 03 December 2012 were contaminated with small black particles, which originated in one of our transport boxes. Therefore, we decided not to filtrate these samples for Chlorophyll a.

Date	Site	Temp	Sal	Den	Chl-a	Texture	L-Arm
30.11.2012	ATKA11	x	x	x	x		x
01.12.2012	ATKA21	x	x	x	x		x
03.12.2012	SNOW01	x	x	x	*		
19.12.2012	ATKA03	x				x	
19.12.2012	ATKA07	x				x	
19.12.2012	ATKA11	x	x	x	x	x	
19.12.2012	ATKA16	x				x	
19.12.2012	ATKA21	x	x	x	x	x	
19.12.2012	ATKA24	x	x	x	x	x	
27.12.2012	ATKA03		x	x	x		
27.12.2012	ATKA11		x	x	x		x
		9	8			6	

14.1. Temperature

9 sea-ice temperature profiles were obtained with a thermometer probe, inserted into small holes drilled with an electric drill. The whole sea-ice core was shadowed throughout the measurement to avoid radiative warming.

14.2. Salinity and Density

The 8 sea-ice cores for salinity, density and Chlorophyll a measurements were immediately segmented into 10cm pieces after drilling, using a manual saw. Care was taken not to lose too much brine, but under the prevailing conditions this generally was not a big problem. Each segment was quickly placed in a pre-weighted plastic can. In addition, each segment was carefully measured using a vernier caliper, but due to imprecise sawing and broken pieces the error is considered to be large. The cores at ATKA11 on 30 November and 27 December, and at ATKA21 on 01 December were drilled immediately after under-ice optical measurements directly above the sensor position.

The samples were melted in the 5°C food storage room (with an exception) to ensure that the cells contained in the samples were not destroyed by a sudden temperature increase



Figure 91: Preparation of sea-ice core for segmentation. Photo: Mario Hoppmann



(a) Brown water emerges from corehole



(b) Distinct brown layer in core



(c) Melted sample (mostly diatoms and some filaments of green algae)

Figure 92: Photos of sea-ice core at ATKA11. Photos: Mario Hoppmann

(Figure 92). After 5 days the melted samples were weighted using a common laboratory balance (Sartorius). Density was then calculated by

$$\rho \text{ [kg/cm}^3\text{]} = \frac{m_{\text{sample}} - m_{\text{can}}}{\pi \cdot 4,5^2 \cdot \text{length}_{\text{seg}}} \quad (1)$$

The salinity of each sample was determined using a *WTW Cond3110* Conductivity-Meter (Figure 93), which was calibrated against a standard solution beforehand.



Figure 93: *WTW Cond3110* Conductivity-Meter. Photo: Mario Hoppmann

14.3. Chlorophyll a and Phaeophytin

The Chlorophyll a content of a water sample has historically provided a useful estimate of algal biomass. Furthermore, the amount of Phaeophytin may be used to assess the physiological state of the phytoplankton contained in that sample. In order to quantify the amount of biomass and its state in the fast ice of Atka Bay during spring and summer 2012/13, we determined the Chlorophyll a and Phaeophytin content of 7 sea ice cores obtained in November and December 2012 with a vertical resolution of 10 cm as described in section 14.2. The following paragraph describes the methodology of our Chlorophyll a measurements in Atka Bay sea-ice cores. An overview of the procedure is given in Figure 95.

Sample acquisition was already described earlier in section 14.2. We used the same samples for the determination of Chlorophyll a and Phaeophytin. We filtrated a defined volume of each melted core segment through a 25 mm *Whatman* GF/F glass-fiber filter with a pore-width of 0.7 μm using a custom-built filtration system. Afterwards, the filters were folded twice, put into a labeled *Eppendorf* tube and stored in the freezer at $-20\text{ }^{\circ}\text{C}$. The frozen samples were processed in a laboratory at AWI Bremerhaven between 15 and 18 April

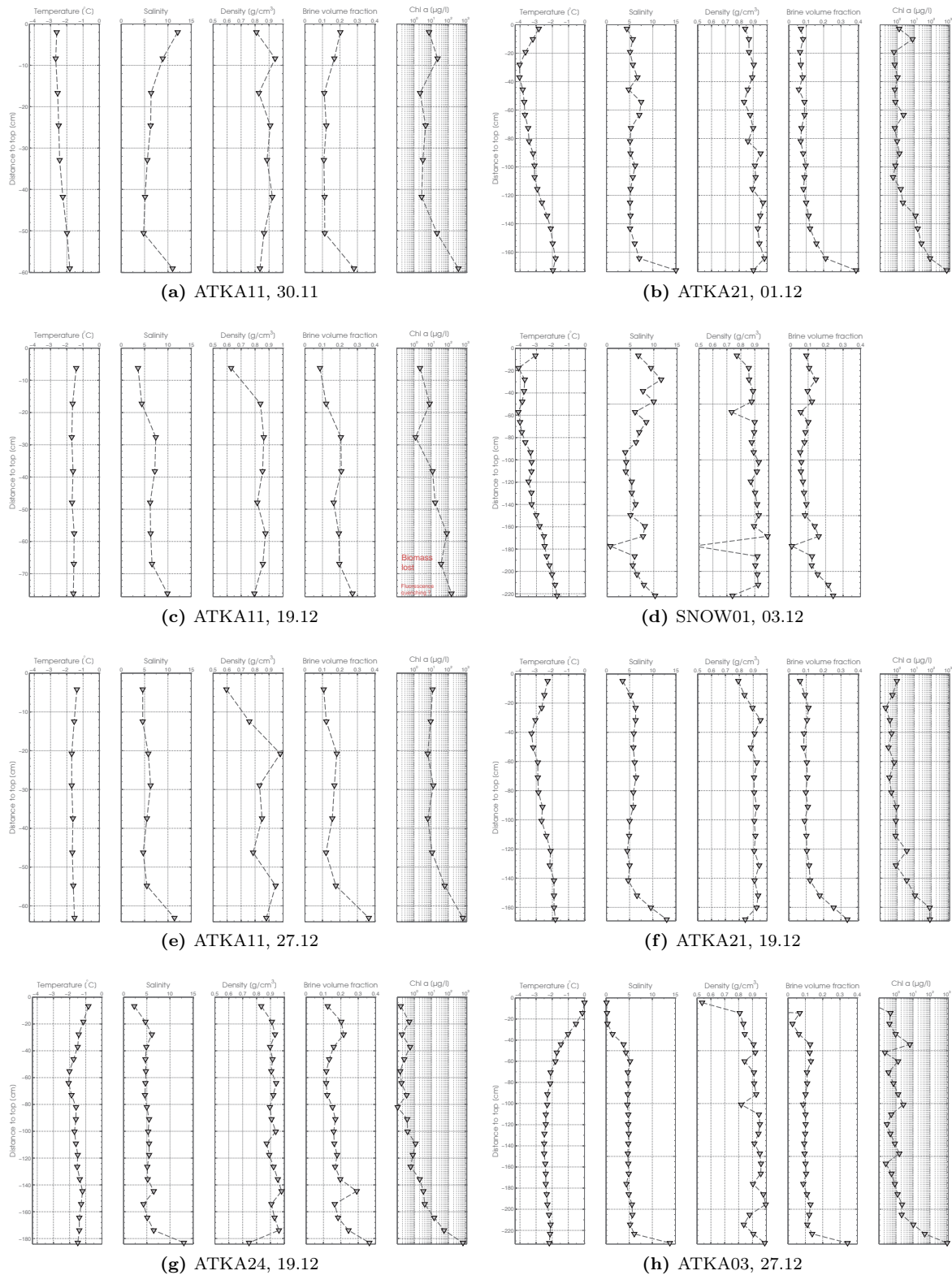


Figure 94: Physical and biological properties of sea-ice cores obtained at different stations in November/December 2012

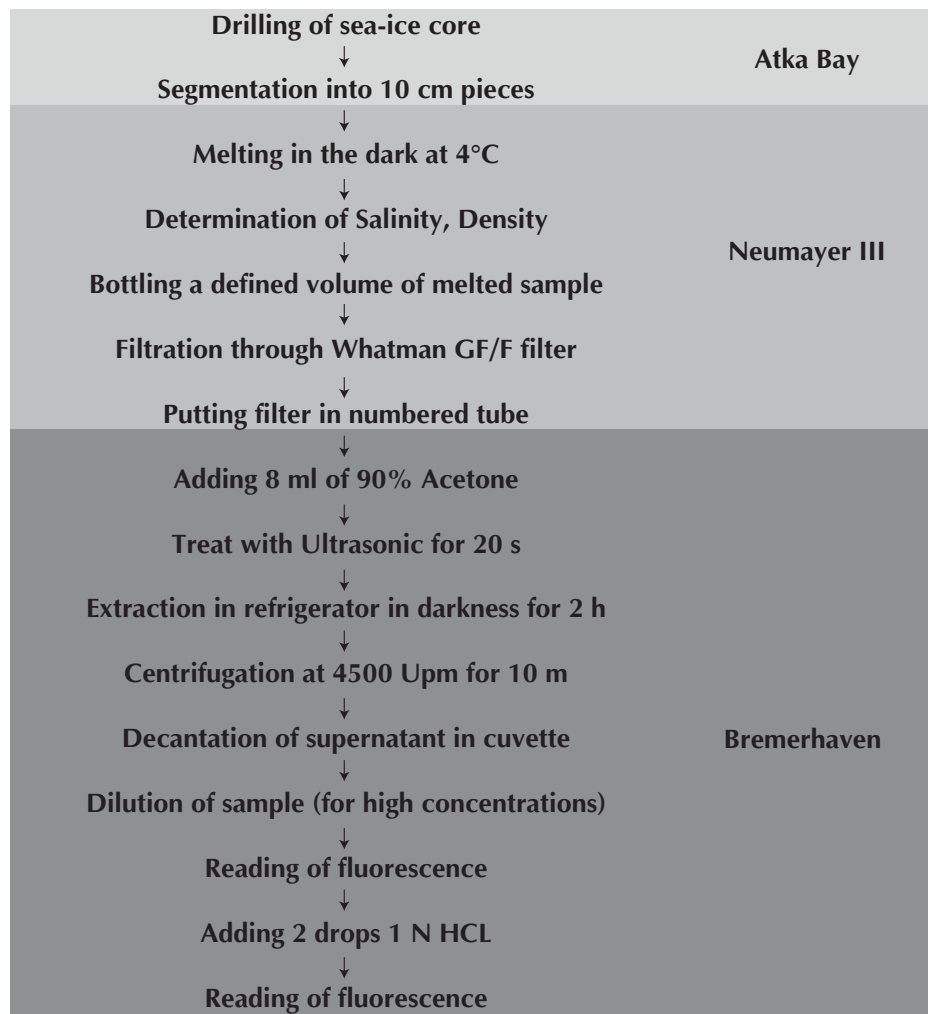


Figure 95: Scheme of Chlorophyll a determination



Figure 96: TD-700 Laboratory Fluorometer by Turner Designs. Photo: Mario Hoppmann

2013, using the fluorometric method.

A TD-700 Laboratory Fluorometer by Turner Designs (Figure 96) was used for the measurement of Chlorophyll a and Phaeophytin. It was calibrated against a standard Chlorophyll a solution on 18 March 2013 by the laboratory personnel. The calibration procedure shall be shortly outlined in the following.

14.3.1. Calibration of fluorometer

The Chlorophyll a standard (*Anacystis nidulans*, Product Number C6144, Sigma-Aldrich) was first dissolved in 90% acetone for several hours for pigment extraction. Due to degradation effects or errors during preparation, the actual chl-a concentration of the standard solution (in mg l^{-1}) was measured spectrophotometrically using the following formula:

$$\text{Chlorophyll a } \left[\frac{\mu\text{g}}{\text{l}} \right] = \frac{A_{\text{max}} - A_{750\text{nm}}}{E \cdot l} \cdot 1000 \quad (2)$$

where:

A_{max} = absorption maximum (664 nm)

$A_{750\text{nm}}$ = absorbance at 750 nm to correct for light scattering

E = extinction coefficient for Chlorophyll a in 90% acetone at 664 nm ($87.67 \text{ L g}^{-1} \text{ cm}^{-1}$)

l = cuvette path length (1 cm)

Please note that all readings are corrected for the reading of pure 90% acetone.

After determination of the actual Chlorophyll a concentration of the standard, seven dilu-

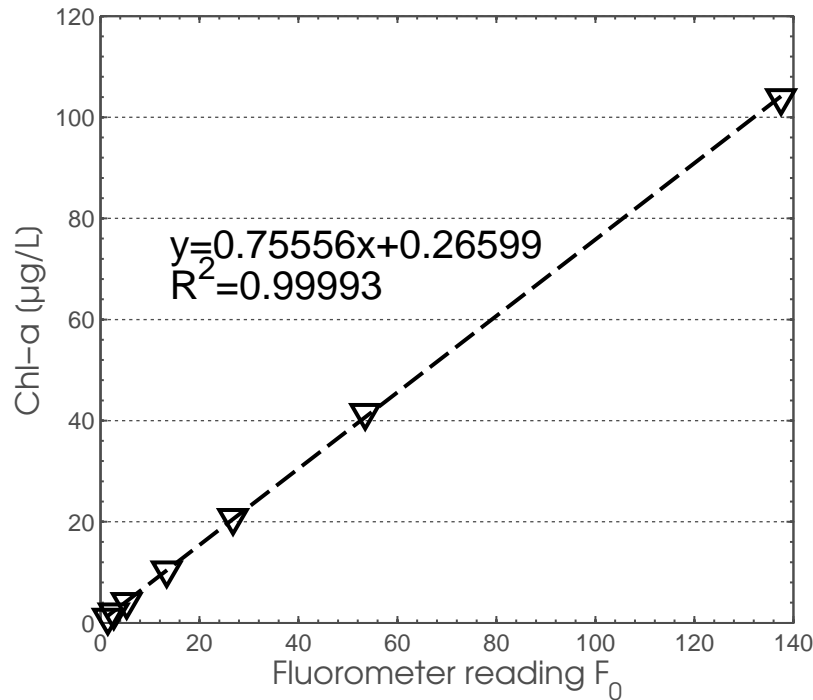


Figure 97: Linear regression of TD700 fluorometer calibration factor

tions were prepared based on the standard with now known concentration (1:10, 1:25, 1:50, 1:100, 1:250, 1:500, 1:1000). Fluorometer readings of all seven dilutions were taken before and after the addition of 2 drops of 1.2 M HCl. Linear regression between non-acidified fluorometric reading vs Chlorophyll a concentration determined spectrophotometrically yielded the linear calibration factor K_x of the fluorometer, in our case $K_x = 0.7556$ (Figure 97). Finally, the acidification coefficient (F_m) was calculated as the average of non-acidified and acidified readings ($\frac{F_0}{F_a}$) of the dilution series (Table 16). In our case, $F_m = 2.14013996$.

Table 16: Calibration of TD700 fluorometer

Vol _{Standard} [μl]	Vol _{total} [ml]	Dilution	Chl a [$\mu\text{g/l}$]	F_0	F_a	F_m
10000	100	0,100000	103,798335	137,5	63,3	2,17591125
2000	50	0,040000	41,5193339	53,5	24,9	2,15789474
1000	50	0,020000	20,7596669	26,8	12,3	2,19834711
1000	100	0,010000	10,3798335	13,4	6,1	2,23728814
1000	250	0,004000	4,15193339	5,3	2,8	1,96153846
100	50	0,002000	2,07596669	2,7	1,4	2,08333333
100	100	0,001000	1,03798335	1,5	0,8	2,16666667
blank				0,2	0,2	
Average						2,14013996

14.3.2. Preparation of samples

The folded filters, sometimes covered with a dense greenish or brownish layer of up to 2 mm in thickness, were put each into a larger PE tube and 8 ml of 90% acetone was added. The workflow allowed for 20-30 filters to be processed at a time. The room was kept in subdued light to prevent cell degradation.

The samples were stored on a rack in the refrigerator at -7°C while treated with ultrasonic for 20 s (Figure 98b) one at a time. Sonication of samples was recommended to support the pigment dissolution from the densely-packed filters. The samples were then covered in aluminium foil and allowed to extract in the refrigerator. After 2 h of extraction, the samples were centrifuged for 10 m at 4500 Upm (Figure 98c) to remove cellular debris and filter particles. The centrifuge was cooled beforehand, but due to a malfunction the instrument could not entirely cool down to the recommended 0°C . Most of the time, the temperature in the centrifuge was between 10°C and 14°C . The supernatant was decanted in a glass cuvette (8ml), and were diluted depending on the concentration of the sample (see next section).

14.3.3. Fluorometry

Principle

Chlorophyll a is a special molecule in higher plants and algae, which is in vivo able to initiate an electron transport chain in the cell by the absorption of photons (photosynthesis). This molecule also has protection mechanisms by which excess light energy is relieved in the form of heat, or by the emission of photons. The latter phenomenon is termed fluorescence. Chlorophyll a in solution only exhibits the two latter forms of energy transport, giving rise to the method of Chlorophyll a measurement by fluorometric analysis. Algal pigments, in particular Chlorophyll a, are extracted in acetone and excited by blue wavelengths of light. As the excited state is highly unstable, the molecule immediately dissipates part of the energy as heat and emits a photon of lower energy (red wavelengths) to return to the ground state. This signal may be detected for example by photo-multipliers and its strength is (in a limited range) proportional to the amount of Chlorophyll a in solution. But if the concentration is too high, re-absorption of emitted photons and different quenching mechanisms trigger, which lead to a nonlinear relationship between Chlorophyll a content and fluorescence.

Measurement of samples

The TD-700 Laboratory Fluorometer was switched on 30 min prior to the measurements to warm up. The cuvette was cleaned with a lab wipe and inserted into the sample chamber (Figure 98e), where the sample was excited by blue light (340-500 nm). Fluorescence was detected by a red-sensitive photomultiplier tube behind a $>665\text{nm}$ red filter. The reading stabilized after a few seconds most of the time, and the value was written down (F_0 , non-acidified). Sometimes the reading would not stabilize, and the cuvette was removed, cleaned, and inserted into the chamber again. Samples with fluorometric readings above 150 were



(a) Lab work



(b) Sonication



(c) Centrifugation



(d) Samples after centrifugation



(e) Measuring a sample



(f) Acidification

Figure 98: Photos of Chl a sample processing. Photos: Mario Hoppmann

diluted with 90% acetone to stay in the linear range of the instrument (Figure 97). Some samples had to be diluted twice in order to reach the linear range. The error in the measurement introduced by dilution is on first order proportional to the concentration of chl-a in the sample. Finally, each sample was acidified with 2 drops of 1.2 M HCl (Figure 98f), stirred and immediately measured again to yield F_a , the acidified fluorescence (or Phaeophytin fluorescence) of the sample.

The “real” chl-a and phaeopigment concentrations were then calculated by

$$\text{Chl-a } \left[\frac{\mu\text{g}}{\text{l}} \right] = \frac{F_m}{F_m - 1} \cdot (F_0 - F_a) \cdot K_x \cdot \frac{V_{ex}}{V_{filt}} \quad (3)$$

$$\text{Phaeo } \left[\frac{\mu\text{g}}{\text{l}} \right] = \frac{F_m}{F_m - 1} \cdot \left(\left(\frac{F_m}{F_m - 1} \cdot F_a \right) - F_0 \right) \cdot K_x \cdot \frac{V_{ex}}{V_{filt}} \quad (4)$$

where:

$$F_m = \text{acidification coefficient } \frac{F_0}{F_a}$$

$$F_0 = \text{reading before acidification}$$

$$F_a = \text{reading after acidification}$$

$$K_x = \text{calibration factor to convert fluorescence into chl-a concentration}$$

$$V_{ex} = \text{extraction volume}$$

$$V_{filt} = \text{sample volume}$$

14.4. Texture

Finally, a set of 6 texture cores was obtained on 19 December 2012 from the sites ATKA03 - ATKA24, which were also visited regularly during winter. Originally it was planned to take these cores later during the campaign, but the state of the sea ice visibly deteriorated during the last two weeks. These cores arrived in Bremerhaven at the end of April 2013. Vertical thin sections of two cores (ATKA11 and ATKA24) were prepared along the entire core length using a Leica Microtome (Figure 99 a and b). In addition, horizontal thin sections were produced at a regular spacing of about 10 cm.

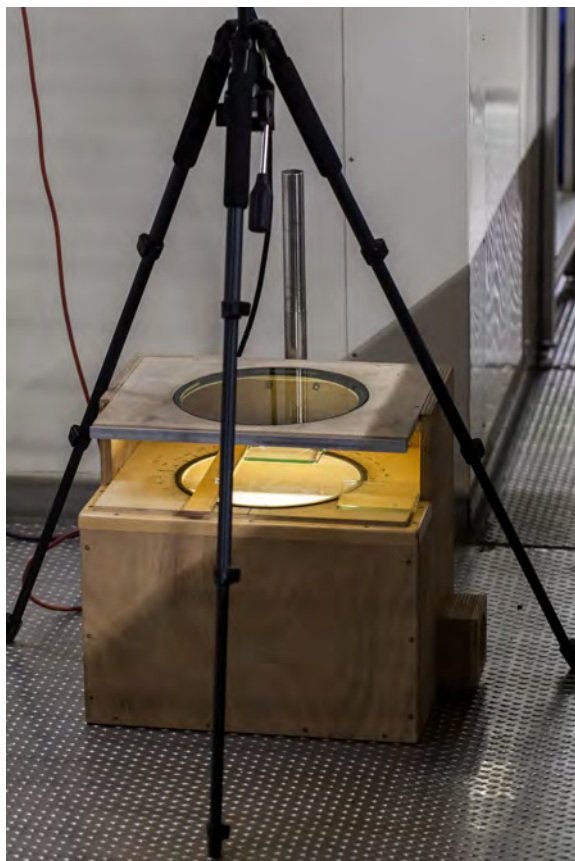
All thin sections were photographed between crossed polarizers (Figure 99 c) to highlight the crystal structure. The results are compiled in Figures 100 and 101 for ATKA11 and ATKA24, respectively.



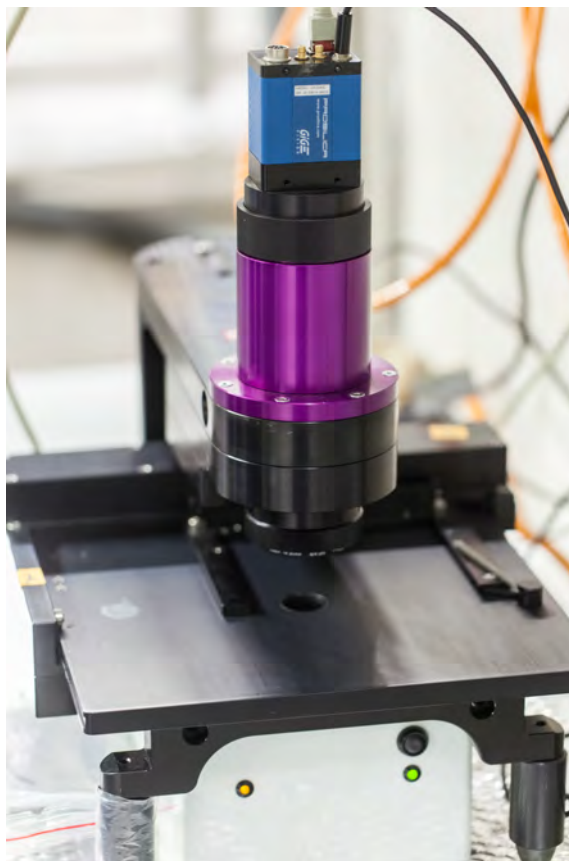
(a) Microtome



(b) Sample during preparation



(c) Camera setup



(d) G50 Fabric Analyzer

Figure 99: Photos of thin section processing. Photos: Mario Hoppmann

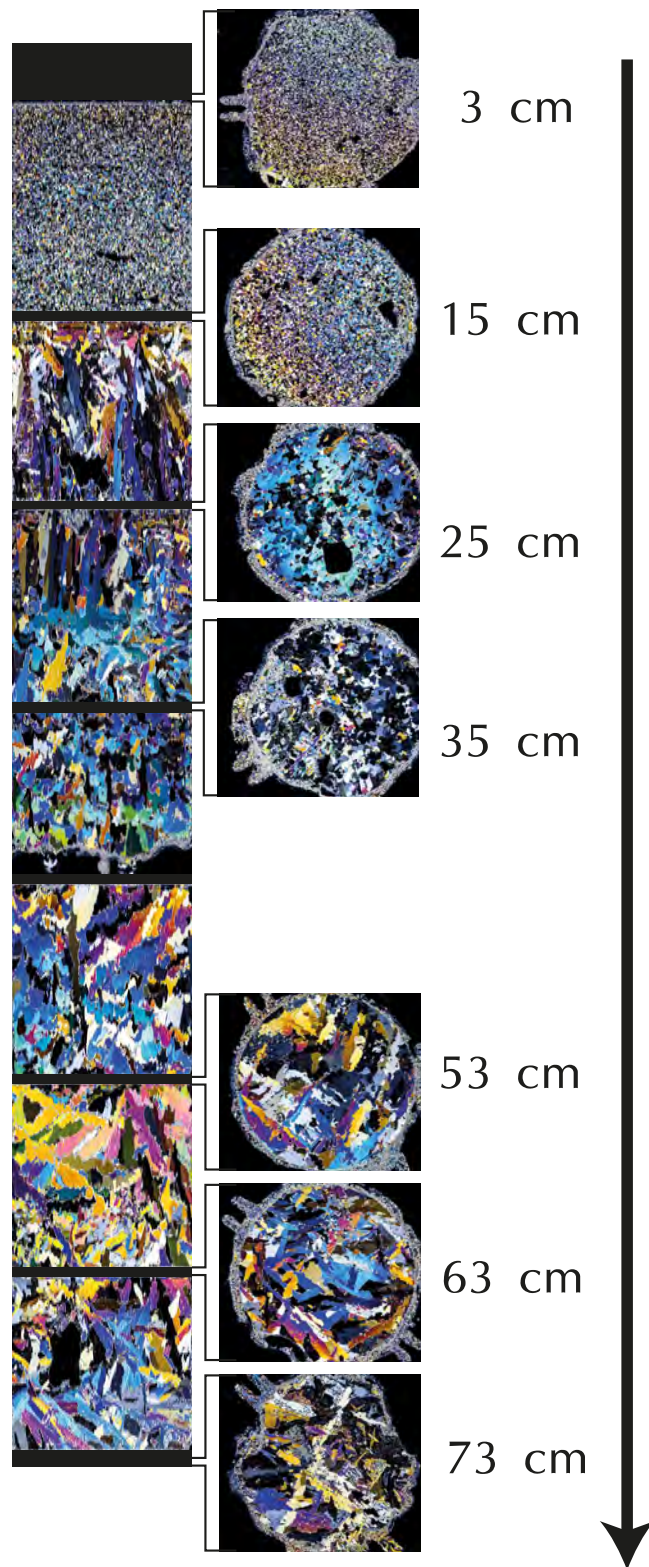


Figure 100: Texture of sea ice at ATKA11. Photos: Mario Hoppmann

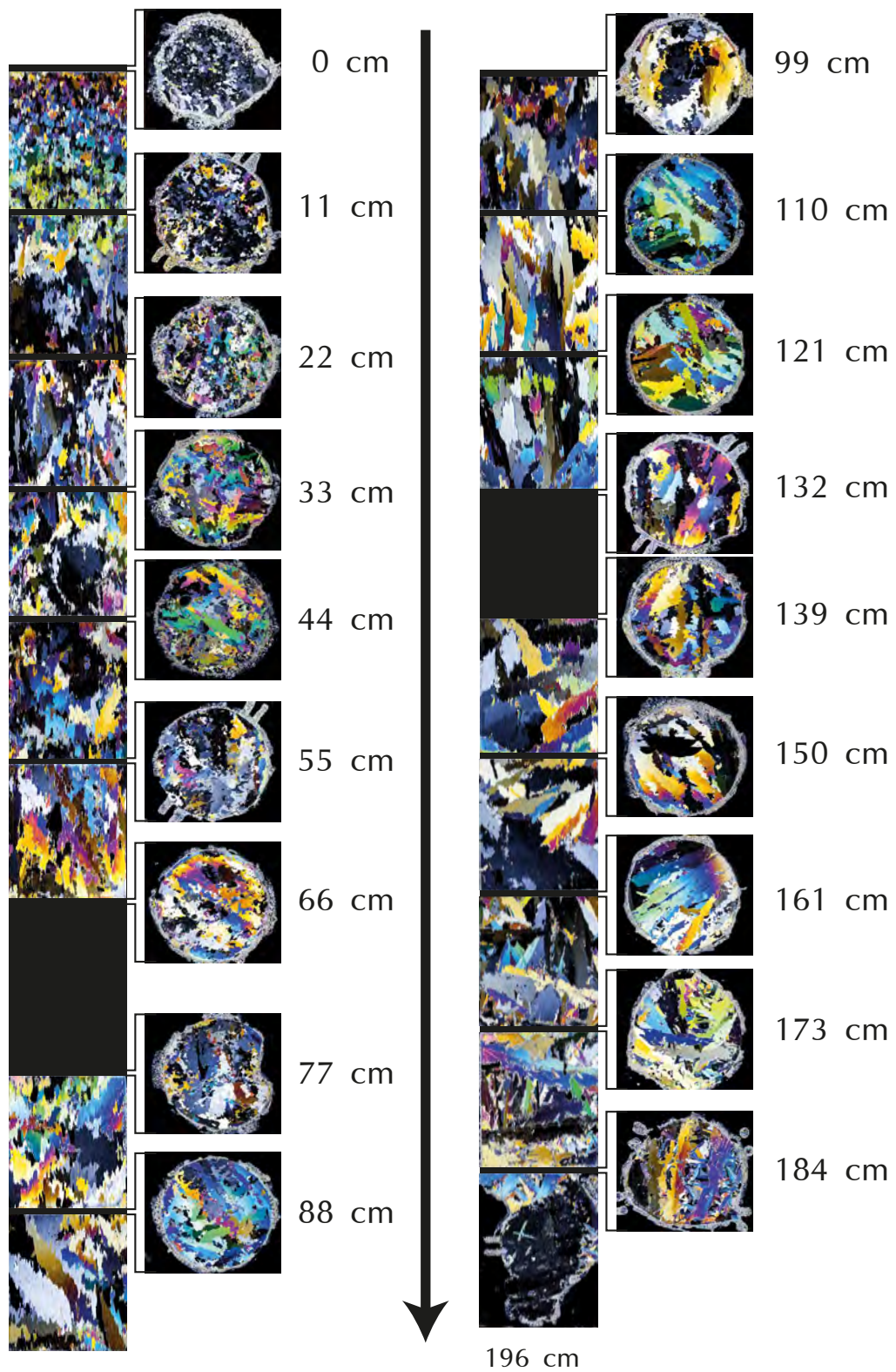


Figure 101: Texture of sea ice at ATKA24. Photos: Mario Hoppmann

15. Aerial Imagery

On 22 December 2012, a large amount of nadir-looking aerial photos of the sea-ice surface at Atka Bay were acquired during a Helicopter-based sea-ice reconnaissance flight. The images were taken by a Canon 5D Mark II with a 24-105mm F4 IS USM lens at 24mm, which was mounted below the cockpit (Figure 102). The camera was operated in automatic aperture control mode, with a predefined, fixed exposure time of 1/1600 s. The shutter was controlled by an external remote switch, set to an interval of 1 seconds.



Figure 102: Canon 5D Mark II camera mounted on the Helicopter. Photos: Mario Hoppmann

The camera time was synchronized to a hand-held GPS in advance, which recorded position data during the flight in 1 s intervals. The altitude was 150 ± 30 m. The GPS track of the reconnaissance flight is shown in Figure 103.

Position data were afterwards added to the meta-data of each image with the GPS tagging utility COPIKS PhotoMapper. The images were saved to a geodatabase, from where they can directly be accessed from the map by clicking on the corresponding tag, for example by using ARCMAP (as shown in Figure 103).

Apart from geotagging, image processing is in a very early stage. First steps have been made to retrieve small-scale surface roughness by precise textured mesh models reconstruction using the 3D reconstruction software Photo Scan by Agisoft.

A sample 3D mesh model of an iceberg near ATKA03 is presented as an example in Figure 103 to illustrate this method. A potential use of these models could be the comparison of the model outcome to TerraSAR-X backscatter coefficients.

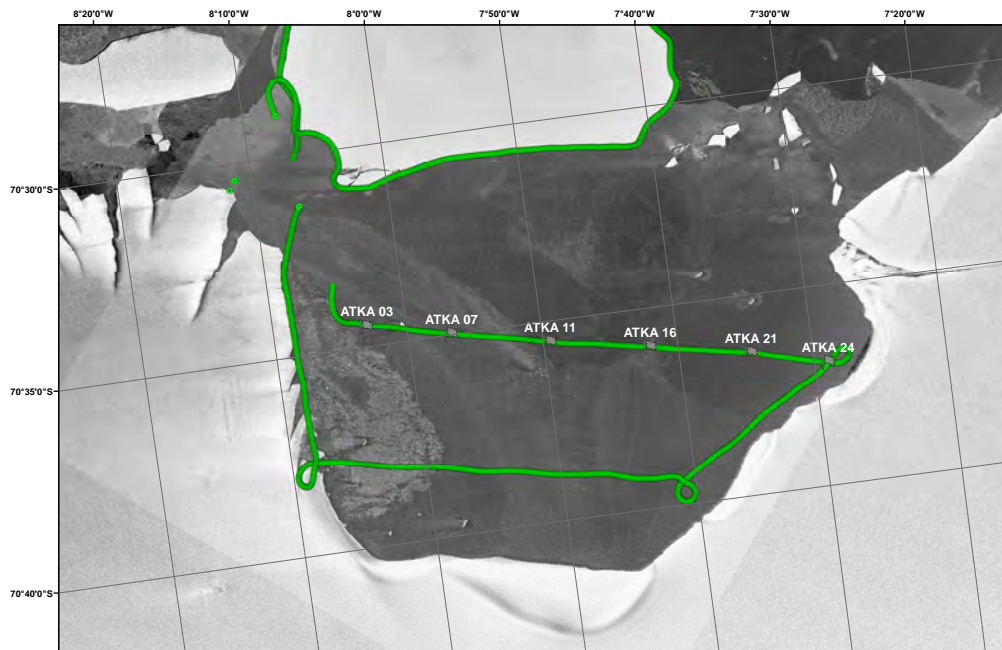


Figure 103: GPS track of aerial images taken on 22 December 2012 during a Helicopter-based sea-ice reconnaissance flight. Each green dot represents the position where an aerial image was taken.

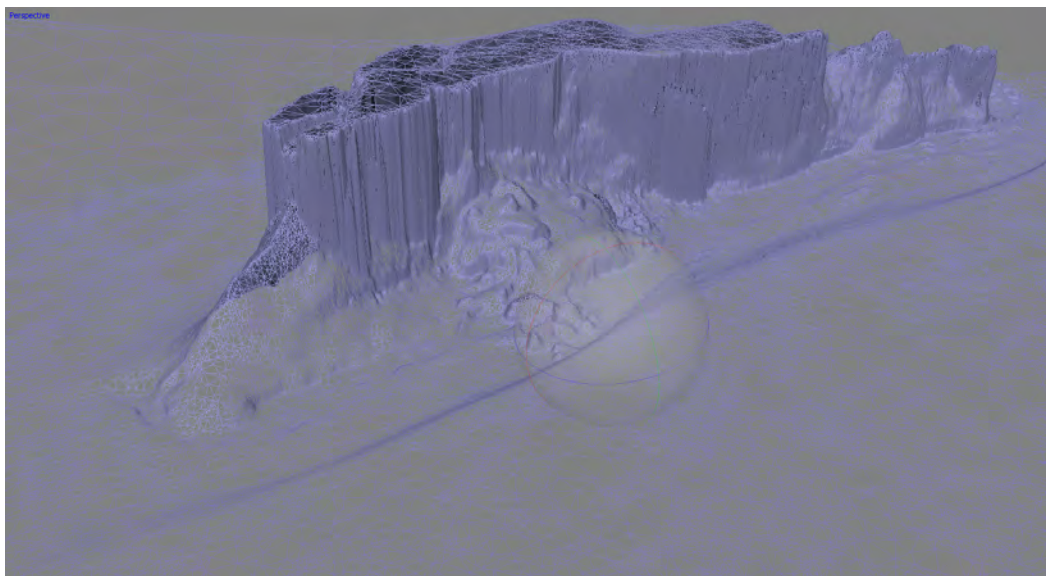


Figure 104: 3D Mesh model of sea-ice surface consisting of 7 images with an overlap of about 30%. The image shows an iceberg several hundred meters east of ATKA03.

16. TerraSAR-X

One aim of our field campaign was to gather ground-truth data for later comparison to remotely sensed satellite imagery. Complementing in particular our snow-pit, radiation and sea-ice data, we intend to combine images from different satellites in order to enhance the interpretation of snow and ice conditions. By doing that, we aim at the development of multi-sensor and large-scale retrieval algorithms on surface conditions and their relation to the snow/ice albedo.

TerraSAR-X is a satellite equipped with an active phased array X-band SAR antenna (wavelength 31 mm, frequency 9.6 GHz), circling in the Earth's orbit at 514 km altitude. X-band radar is independent of illumination and weather conditions, so that acquisitions can be made at any time of the day or night and independent of cloud coverage (cite DLR?).

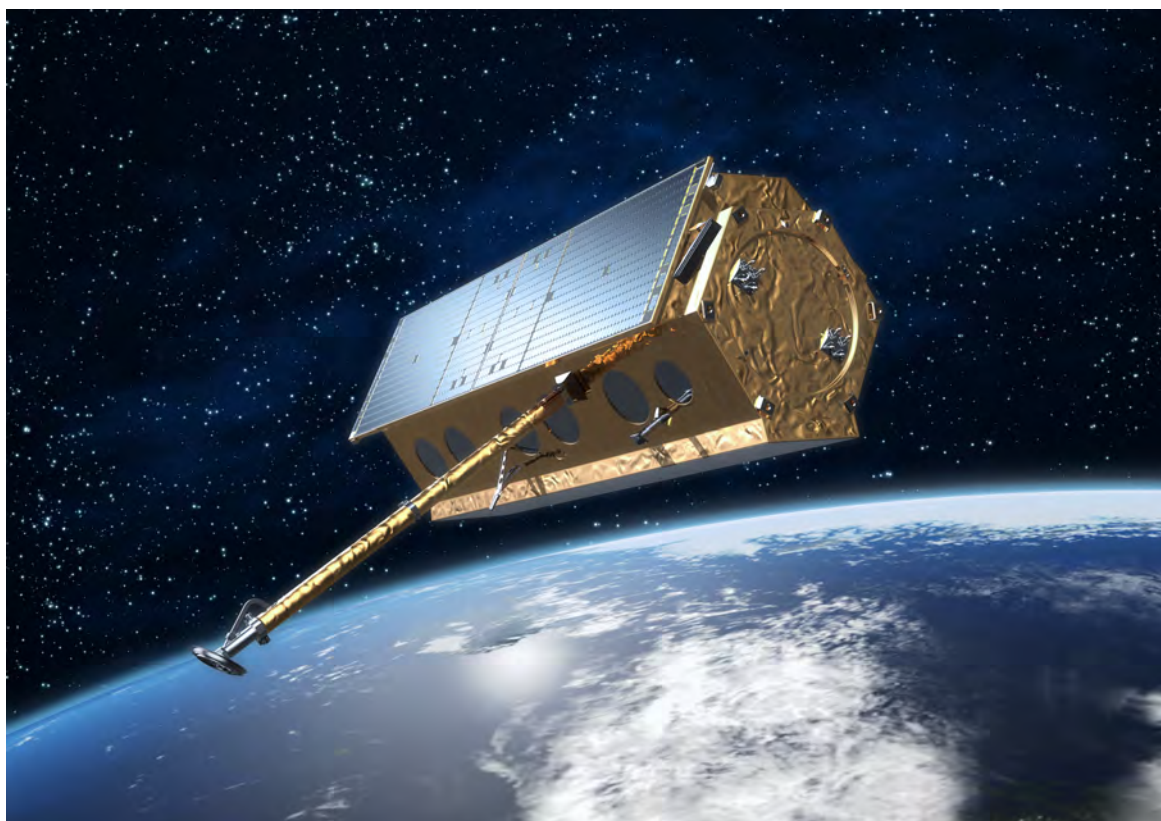


Figure 105: TerraSAR-X satellite (source: EADS Astrium)

During the SIMBIS campaign, we obtained 19 high-resolution TerraSAR-X images in different modi and polarisations parallel to our ongoing field measurements of snow and sea ice properties (Table 18)). In the future analysis of this data, we will assess the influence of sea ice and snow physical properties on X-band radar. The focus of this study will be to contribute to the question whether X-band radar is sensitive to the seasonal evolution of snow, and if it is possible to identify the timing of snow melt onset on fast ice in Atka

Table 17: TerraSAR-X main imaging modes. Single, dual and full polarimetric data takes are possible.

Mode	Resolution [m]	Scene size [km x km]
SpotLight	up to 1 m	10 x 5
StripMap	up to 3 m	30 x 50
ScanSAR	up to 18 m	100 x 150

Bay by TerraSAR-X imagery. Since the formation of melt water significantly amplifies the attenuation of microwaves, we expect that melt onset can be defined by a strong decrease in backscatter values. In addition, the possibility for the detection of thin ice formation and snow cover evolution using TerraSAR-X data in dual-pol strip map mode will be assessed in comparison to thermal infrared imagery, as acquired by the Moderate Resolution Imaging Spectroradiometer (MODIS, aboard satellites Terra and Aqua) ice surface temperature data (MOD29). We will also investigate the possibility to empirically retrieve ice and snow albedo from TSX-images, using the results of the spectral radiometer measurements described earlier.

Table 18: TerraSAR-X data availability

Date	Mode	Polarisation
25.06.2012	ScanSAR	HH
05.09.2012	ScanSAR	HH
23.10.2012	ScanSAR	HH
15.11.2012	ScanSAR	HH
24.11.2012	StripMap	HH,VV
27.11.2012	StripMap	HH
01.12.2012	StripMap	HH,HV
07.12.2012	StripMap	HH,VV
12.12.2012	StripMap	HH,HV
18.12.2012	StripMap	HH
23.12.2012	StripMap	HH,VV
24.12.2012	StripMap	HH,VV
09.01.2013	ScanSAR	HH

III

Reference List

- Dijk, A. v., Moene, A. and Debruin, H. (2004). The principles of surface flux physics: theory, practice and description of the ecpack library. (Cited on page 51.)
- Drüe, C. (2012). *EC-Frame Users Manual*. (Cited on page 50.)
- Fretwell, P., Pritchard, H. D., Vaughan, D. G., Bamber, J. L., Barrand, N. E., Bell, R., Bianchi, C., Bingham, R. G., Blankenship, D. D., Casassa, G., Catania, G., Callens, D., Conway, H., Cook, A. J., Corr, H. F. J., Damaske, D., Damm, V., Ferraccioli, F., Forsberg, R., Fujita, S., Gogineni, P., Griggs, J. A., Hindmarsh, R. C. A., Holmlund, P., Holt, J. W., Jacobel, R. W., Jenkins, A., Jokat, W., Jordan, T., King, E. C., Kohler, J., Krabill, W., Riger-Kusk, M., Langley, K. A., Leitchenkov, G., Leuschen, C., Luyendyk, B. P., Matsuoka, K., Nogi, Y., Nost, O. A., Popov, S. V., Rignot, E., Rippin, D. M., Riviera, A., Roberts, J., Ross, N., Siegert, M. J., Smith, A. M., Steinhage, D., Studinger, M., Sun, B., Tinto, B. K., Welch, B. C., Young, D. A., Xiangbin, C. and Zirizzotti, A. (2012). Bedmap2: improved ice bed, surface and thickness datasets for antarctica, *The Cryosphere Discuss.* **6**(5): 4305–4361. (Cited on pages 9 and 11.)
- Günther, S. and Dieckmann, G. S. (1999). Seasonal development of algal biomass in snow-covered fast ice and the underlying platelet layer in the Weddell Sea, Antarctica, *Antarctic Science* **11**(3): 305–315. (Cited on pages 10 and 92.)
- Heil, P., Allison, I. and Lytle, V. I. (1996). Seasonal and interannual variations of the oceanic heat flux under a landfast Antarctic sea ice cover, *Journal of Geophysical Research-Oceans* **101**(C11): 25741–25752. (Cited on page 8.)
- Heil, P., Gerland, S. and Granskog, M. A. (2011). An Antarctic monitoring initiative for fast ice and comparison with the Arctic, *The Cryosphere Discussions* **5**(5): 2437–2463.
URL: <http://www.the-cryosphere-discuss.net/5/2437/2011/> (Cited on page 8.)
- Hoppmann, M., Nicolaus, M. and Asseng, J. (2012). Summary of AFIN measurements on Atka Bay landfast ice in 2011.
URL: <http://epic.awi.de/24642/> (Cited on page 10.)
- Hoppmann, M., Nicolaus, M. and Schmithüsen, H. (2011). Summary of AFIN measurements on Atka Bay landfast ice in 2010.
URL: <http://epic.awi.de/24642/> (Cited on page 10.)
- Kawamura, T., Ohshima, K. I., Takizawa, T. and Ushio, S. (1997). Physical, structural and isotopic characteristics and growth processes of fast sea ice in Lützow-Holm Bay, Antarctica, *Journal of Geophysical Research* **102**(C2): 3345–3355. (Cited on page 8.)
- Kipfstuhl, J. (1991). On the formation of underwater ice and the growth and energy budget of the sea ice in Atka Bay, Antarctica (mostly in German), *Reports on Polar and Marine Research* **85**: 88p. (Cited on page 10.)
- Lei, R., Li, Z., Cheng, B., Zhang, Z. and Heil, P. (2010). Annual cycle of landfast sea ice in Prydz Bay, east Antarctica, *J. Geophys. Res.* **115**(C2): C02006. (Cited on page 8.)

- Leonard, G. H., Langhorne, P. J., Williams, M. J. M., Vennell, R., Purdie, C. R., Dempsey, D. E., Haskell, T. G. and Frew, R. D. (2011). Evolution of supercooling under coastal Antarctic sea ice during winter, *Antarctic Science* **23**(4): 399–409. (Cited on page 8.)
- Lewis, E. L. and Perkin, R. G. (1986). Ice pumps and their rates, *J. Geophys. Res.* **91**(C10): 11756–11762. (Cited on page 92.)
- McGuinness, M. J., Williams, M. J. M., Langhorne, P. J., Purdie, C. and Crook, J. (2009). Frazil deposition under growing sea ice, *Journal of Geophysical Research-Oceans* **114**. (Cited on page 8.)
- Tang, S. L., Qin, D. H., Ren, J. W., Kang, J. C. and Li, Z. J. (2007). Structure, salinity and isotopic composition of multi-year landfast sea ice in Nella Fjord, Antarctica, *Cold Regions Science and Technology* **49**(2): 170–177. (Cited on page 8.)
- Trodahl, H. J., McGuinness, M. J., Langhorne, P. J., Collins, K., Pantoja, A. E., Smith, I. J. and Haskell, T. G. (2000). Heat transport in McMurdo Sound first-year fast ice, *Journal of Geophysical Research-Oceans* **105**(C5): 11347–11358. (Cited on page 8.)

Acknowledgements

We are most grateful to the other overwinterers and helpers at Neumayer III in 2012/13 for their support.

We thank Angelika Humbert (University of Hamburg) and the German Aerospace Center (DLR) for providing high resolution TerraSAR-X satellite images during our campaign.

We highly acknowledge Gert König-Langlo, Bernd Loose, Gerhard Dieckmann, Lars Kindermann and other scientists and technicians at AWI for their support and professional advice in every respect.

This work was supported by the Deutsche Forschungsgemeinschaft (DFG) in the framework of the priority programme "Antarctic Research with comparative investigations in Arctic ice areas" by grants NI 1092/2, HE 2740/12.